

## Near-field characterization of plasmonic waveguides

Zenin, Volodymyr

*Publication date:*  
2014

*Document version:*  
Accepted manuscript

*Citation for polished version (APA):*  
Zenin, V. (2014). *Near-field characterization of plasmonic waveguides.*

Go to publication entry in University of Southern Denmark's Research Portal

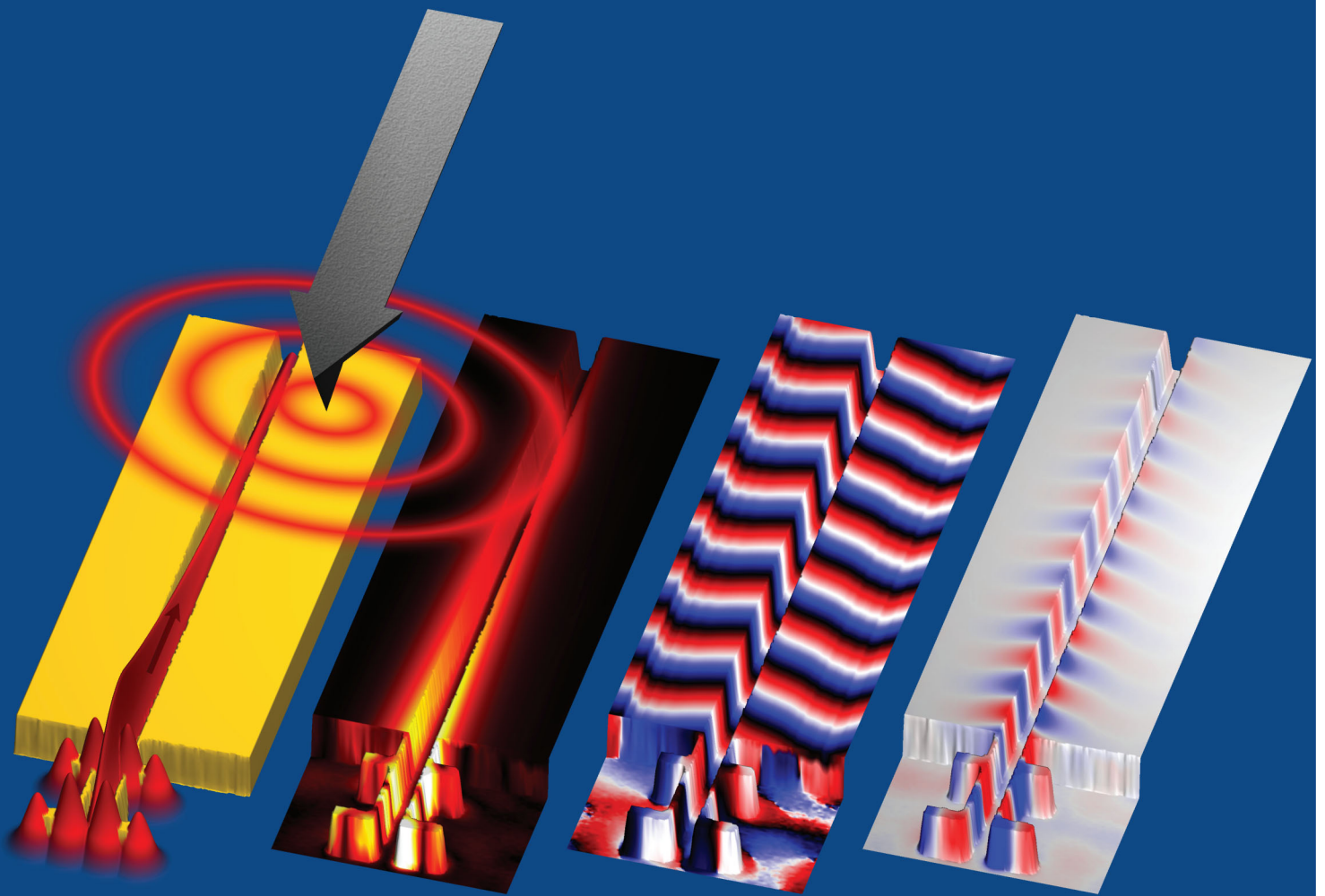
### Terms of use

This work is brought to you by the University of Southern Denmark.  
Unless otherwise specified it has been shared according to the terms for self-archiving.  
If no other license is stated, these terms apply:

- You may download this work for personal use only.
- You may not further distribute the material or use it for any profit-making activity or commercial gain
- You may freely distribute the URL identifying this open access version

If you believe that this document breaches copyright please contact us providing details and we will investigate your claim.  
Please direct all enquiries to [puresupport@bib.sdu.dk](mailto:puresupport@bib.sdu.dk)

# Near-field characterization of plasmonic waveguides



Volodymyr Zenin

Volodymyr Zenin

---

*Near-field characterization of plasmonic waveguides*



Department of Technology and Innovation  
University of Southern Denmark

NEAR-FIELD CHARACTERIZATION OF PLASMONIC WAVEGUIDES

Copyright © 2014 by Volodymyr Zenin.

Typeset in L<sup>A</sup>T<sub>E</sub>X2<sub>ε</sub> by the author.

Printed by Print&Sign, University of Southern Denmark, Odense.

All rights reserved. No part of this publication may be reproduced, transmitted or translated in any form or by any means, electronic or mechanical, including photocopy, recording, or any information storage and retrieval system, without prior permission in writing from the author.

---

## Summary

This PhD thesis presents investigation of plasmonic waveguides and waveguiding components by means of scanning near-field optical microscopy characterizations, far-field optical observations, and numerical simulations. The plasmonic waveguiding attracts huge interest due to several reasons: 1) it is believed to bridge naturally optical and electronic circuits; 2) it looks natural and most efficient for active applications due to the presence of the metal inside the core of the plasmonic mode; 3) the mode size and correspondent field confinement of plasmonic waveguides can be tuned in a vast range simply by changing geometric parameters of the waveguide, keeping in mind the trade-off between confinement and propagation losses. A broad variety of plasmonic waveguides and waveguide components, including antennas for coupling the light in/out of the waveguide, requires correspondent characterization capabilities, especially on experimental side. The most straight-forward and powerful technique for such purpose is scanning near-field optical microscopy, which allows to probe and map near-field distribution and therefore becomes the main tool in this project. The detailed description of the used setups and their imaging techniques is included additionally to the main research of plasmonic waveguides (channel plasmon polariton, long-range dielectric-loaded surface plasmon polariton, and plasmonic slot waveguides) and waveguide components (antennas, S-bends, and directional couplers) included as a reprint of papers.

## Resumé

Denne Ph.d. afhandling præsenterer undersøgelser af plasmoniske bølgeledere og bølgelederkomponenter ved brug af optisk skanning-nærfeltmikroskopi, optiske fjernfelts observationer, og numeriske simuleringer. Plasmoniske bølgeledere tiltrækker stor interesse på grund af følgende årsager: 1) det menes at kunne naturligt forbinde optiske og elektroniske kredsløb; 2) det fremstår naturligt og mest effektivt for aktive applikationer på grund af metallet i centrum af den plasmoniske tilstand; 3) Størrelsen af plasmoniske bølgelederes tilstande kan kontrolleres i et stort område ved at ændre de geometriske parametre af bølgelederen, mens der tages hensyn til afvejningen mellem afgrænsning af feltet og udbredelsestab. En bred vifte af plasmoniske bølgeledere og bølgelederkomponenter, herunder antenner for ind- og udkobling af lys i bølgeledere, har behov for at blive karakteriseret eksperimentelt. Den mest ligetil og kraftfulde teknik til dette formål, og derfor hovedværktøjet i dette projekt, er optisk skanning-nærfeltmikroskopi, hvilket kan bruges til at undersøge og kortlægge nærfeltsfordelingen. Denne afhandling indeholder udover hovedforskningen i plasmoniske bølgeledere (channel plasmon polariton, long-range dielectric-loaded surface plasmon polariton, og plasmonic-slot bølgeledere) og bølgelederkomponenter (antenner, S-bøjninger, og retningsbestemte koblere), der er inkluderet som et genoptryk af artikler, også en detaljeret beskrivelse af de anvendte eksperimentelle opsætninger og afbildningsteknikker.

## Preface

---

This Ph.D. thesis presents most of the work done during my time as a Ph.D. student at the Department of Technology and Innovation, University of Southern Denmark, Denmark, from September 2011 to August 2014 under skilled supervision of Professor Dr. Scient. Sergey I. Bozhevolnyi and unofficial co-supervision of Associate Professor Valentyn S. Volkov. The thesis focuses on experimental investigation of plasmonic nanostructures using scanning near-field optical microscope. It is based on 5 peer-reviewed journal papers that are enclosed in Appxs. [A.1–A.5](#).

## Outline

The thesis is organized into two parts and represents the research done during my PhD project. The first part contains three chapters and includes more detailed description and the work, which was not included into published papers. The first chapter shortly introduces to the plasmonics and plasmonic waveguides. The second chapter describes the most straight-forward experimental technique of visualization and investigation of plasmonic modes – scanning near-field optical microscopy (SNOM). The real setups used for the research in this project are described in details. The last chapter focuses on amplitude- and phase-resolved detection technics with a particular interest on application in scattering-type SNOM (s-SNOM).

The second part of the thesis contains reprints of 5 papers, where 4 of them done during this PhD project and the first paper done just before its beginning (but it is included for consistency, since it is historically and logically connected to other papers). The first two papers are focused on investigation of channel plasmon polariton (CPP) waveguides formed by V-grooves milled in otherwise smooth metal films. The main CPP characteristics (mode index, width, and propagation length), as well as directional coupling are studied experimentally (by use of fiber-

based SNOM) and compared to theoretical results and numerical simulations. The third paper is based on research of long-range dielectric-loaded plasmonic waveguides (LR-DLSPPWs) – both experimentally and numerically. The fourth paper describes study of nanofocusing in circular sector-like nanoantennas using far-field observation (transmission spectra), near-field measurements, and numerical simulations. The obtained results are supported by a simple interpretation of SPP focusing. Finally, the last paper focuses on investigation of plasmonic slot waveguides and nanocouplers using s-SNOM. The obtained amplitude- and phase-resolved near-field mapping allows direct measurement of effective mode index, propagation length and relative coupling efficiency, which is shown to be in good correspondence with numerical simulations. Overall, the papers themselves should be considered as the main scientific value of this PhD thesis.

## Acknowledgments

First and foremost I am grateful to my supervisor Prof. Dr. Scient. Sergey I. Bozhevolnyi for introducing me to the field of plasmonics, nano-optics and near-field microscopy. Owing to his guidance, support and sober judgment, I never got stuck and always continued to move forward in my research. Also I would like to deeply thank my unofficial co-supervisor, colleague and friend, Ass. Prof. Valentyn S. Volkov for introducing me to the world of experiment and particularly – to the scanning near-field optical microscopy. I appreciate a lot those knowledge, approach and attitude I learned from him. Also I am grateful to Eloïse Devaux and Thomas W. Ebbesen (Université de Strasbourg, France) for fabrication of channel plasmon polariton waveguides. I would like to acknowledge a fruitful on-going collaboration with Andrei Andryieuski, Radu Malureanu, and Andrei V. Lavrinenko (DTU Fotonik, Denmark), which has already yield in paper concerning plasmonic slot waveguides and nanocouplers. Also I am thankful to Kristján Leósson (University of Iceland) for fabrication of the substrate for long-range dielectric-loaded surface plasmon polariton waveguides. I also thank my former colleague Zhanghua Han (China Jiliang University) for the numerical simulations and fabrication of samples in almost every project I had.

I greatly appreciate my colleagues in Department of Technology and Innovation who helped me a lot in my work and my life. Especially I would like to thank Ilya Radko, who was always open for help and informal discussions. During my stay in Denmark I learned Danish culture and language (and even passed the final exam PD3) thanks to my Danish teachers Betina Rohr and Lola Garcelan (Lærdansk).

Last but not least I want to thank my fiancée Oksana, my brother Peter and my parents for their infinite love and valuable support.

*Odense, Denmark, September 2014*

**Vladimir Zenin**



## List of used acronyms

---

<b>1D/2D:</b>	One-dimensional/two-dimensional
<b>AFM:</b>	Atomic-force microscopy/microscope
<b>CPP(W):</b>	Channel plasmon polariton (waveguides)
<b>DC:</b>	Directional coupler
<b>DFT:</b>	Discrete Fourier transform
<b>EI(M):</b>	Effective index (method)
<b>FE:</b>	Electric field enhancement
<b>FEM:</b>	Finite element method
<b>FIB:</b>	Focused ion-beam
<b>FWHM:</b>	Full width at half-maximum
<b>GSP:</b>	Gap surface plasmon
<b>IMI:</b>	Insulator-metal-insulator
<b>(LR-)DLSP(W):</b>	(Long-range) dielectric-loaded surface plasmon-polariton (waveguide)
<b>MIM:</b>	Metal-insulator-metal

<b>NA:</b>	Numerical aperture
<b>(N)IR:</b>	(Near) infrared
<b>PEC:</b>	Perfect electric conductor
<b>PMMA:</b>	Polymethyl methacrylate
<b>Q-factor:</b>	Quality-factor
<b>SEM:</b>	Scanning electron microscopy/microscope
<b>SOH:</b>	Synthetic optical holography
<b>SPP:</b>	Surface plasmon polariton
<b>(s-)SNOM:</b>	(Scattering-type) scanning near-field optical microscopy/microscope
<b>TE/TM:</b>	Transverse electric/transverse magnetic
<b>UV:</b>	Ultraviolet
<b>WPP:</b>	Wedge plasmon polariton
<b>WR:</b>	Waveguide-ring

# Contents

---

Summary . . . . .	iii
Resumé . . . . .	iv
Preface . . . . .	v
Acronyms . . . . .	vii
Contents . . . . .	x
<b>I Introduction</b>	<b>1</b>
1 Introduction to plasmonics . . . . .	3
1.1 Surface plasmon polaritons . . . . .	4
1.2 Long- and short-range SPPs . . . . .	6
1.3 Gap surface plasmons . . . . .	8
1.4 SPP waveguides . . . . .	9
2 Scanning near-field optical microscopy . . . . .	13
2.1 General principles of near-field microscopy . . . . .	13
2.2 Apertureless fiber-based SNOM . . . . .	14
2.3 Scattering-type SNOM . . . . .	17
3 Amplitude- and phase-resolved detection . . . . .	19
3.1 Homodyne detection . . . . .	20
3.2 Heterodyne detection . . . . .	21
3.3 Pseudoheterodyne detection . . . . .	22
3.4 Synthetic optical holography . . . . .	24
<b>II Collection of papers</b>	<b>29</b>
A.1 CPP dispersion . . . . .	31
A.2 CPP directional coupling . . . . .	39
A.3 LR-DLSPP directional coupling . . . . .	51
A.4 Nanofocusing in circular sector-like nanoantennas . . . . .	61

A.5 Plasmonic slot waveguides and nanocouplers . . . . .	73
Authorship agreements . . . . .	89
<b>Bibliography</b>	<b>95</b>
References . . . . .	97
List of publications . . . . .	101

# Part I

---

## Introduction



# Chapter 1

## Introduction to plasmonics

---

Modern communication systems dealing with huge amounts of data at ever increasing speed try to utilize the best sides of electronic and optical circuits. Electronic circuits are tiny but their operation speed is limited, whereas optical circuits are much better in transmitting data at high speed, but their sizes are limited by diffraction. Therefore modern computers use electronic circuits both for calculations (active components) and for interconnects and communication between different internal parts (passive components), while optical circuits (with a use of optical fibers) are used for transmission of data over long distances. Thus several goals arise: 1) making efficient and compact transition between electronic and optical circuits; 2) creating optical waveguides small enough to be used for interconnects; 3) developing tiny and efficient active optical components, which can completely replace electronics used for calculations. Surface plasmon polaritons (SPPs), which are coupled electromagnetic (EM) excitations and surface collective oscillations of free electrons in a metal, are bound to and propagate along metal-dielectric interfaces [1, 2], therefore they look natural for realization of the transition between electronic and optical circuits [3]. Having by nature subwavelength spatial periods and transverse dimensions perpendicular to the metal surface, SPPs offer the possibility to realize subwavelength waveguiding and ultra-compact photonic components [4]. Finally, due to the confinement of the electromagnetic field to the metal surface, plasmonic waveguides are in principle more efficient for active applications than the photonic ones. However, the important issue in this context is to strongly confine the SPP field in the cross section perpendicular to the SPP propagation direction (smaller cross sections ensure smaller bend losses, smaller cross-talk, and higher densities of components), while keeping relatively low propagation loss. The investigation and research of such plasmonic waveguides and waveguide components in this context is the main focus of this PhD thesis.

## 1.1 Surface plasmon polaritons

SPPs are studied for about a hundred years, therefore today it is a well-known subject. To my knowledge, a theory of SPP is already well described in several books [1, 5], so let's just outline the main properties of SPPs here. SPPs are quasi two-dimensional (2D) electromagnetic waves bound to the metal-dielectric interface. Field components of monochromatic SPPs, travelling in the positive  $x$ -axis are:

$$\begin{pmatrix} H_y^{\text{m,d}}(x, z) \\ E_x^{\text{m,d}}(x, z) \\ E_z^{\text{m,d}}(x, z) \end{pmatrix} = \begin{pmatrix} \text{metal} & \text{dielectric} \\ -\omega\epsilon_0 & -\omega\epsilon_0 \\ -ik_z^{\text{m}}/\epsilon_{\text{m}} & ik_z^{\text{d}}/\epsilon_{\text{d}} \\ k_{\text{SPP}}/\epsilon_{\text{m}} & k_{\text{SPP}}/\epsilon_{\text{d}} \end{pmatrix} C e^{ik_{\text{SPP}}x} e^{-k_z^{\text{m,d}}|z|}, \quad (1.1)$$

where  $\epsilon_{\text{m,d}}$  is a dielectric constant (relative permittivity),  $k_{\text{SPP}}$  is a propagation constant (SPP wave vector), and indices m, d indicate either metal or dielectric half-space (Fig. 1.1).

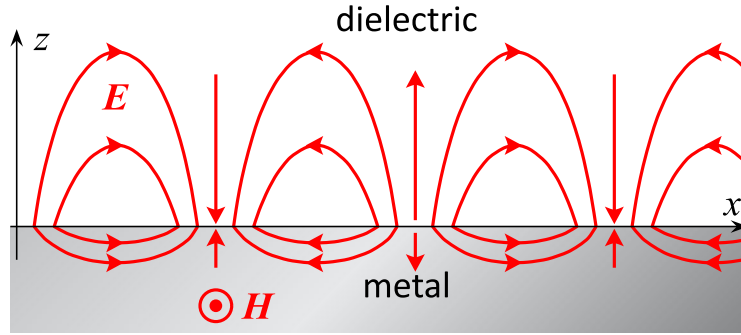


Figure 1.1: Geometry and field distribution of SPP.

As one can see, the field decreases exponentially away from the interface with the following rate

$$k_z^{\text{m,d}} = \sqrt{k_{\text{SPP}}^2 - \epsilon_{\text{m,d}}k_0^2}, \quad k_0 = \frac{\omega}{c}. \quad (1.2)$$

The boundary conditions for electric field yields the following relation:

$$\frac{k_z^{\text{m}}}{-\epsilon_{\text{m}}} = \frac{k_z^{\text{d}}}{\epsilon_{\text{d}}}, \quad (1.3)$$

thus leading to the expression for the propagation constant (called also a dispersion relation):

$$k_{\text{SPP}} = k_0 \sqrt{\frac{\epsilon_{\text{m}}\epsilon_{\text{d}}}{\epsilon_{\text{m}} + \epsilon_{\text{d}}}} = \frac{\omega}{c} \sqrt{\frac{\epsilon_{\text{m}}\epsilon_{\text{d}}}{\epsilon_{\text{m}} + \epsilon_{\text{d}}}} \quad (1.4)$$

For the analytical consideration of SPPs and other plasmonic modes it is usually helpful to use a simplified Drude approximation for the relative permittivity of



metal [6]:

$$\varepsilon_m(\omega) = 1 - \frac{\omega_p^2}{\omega^2}, \quad (1.5)$$

where  $\omega_p$  is the plasma frequency of the considered metal. With such approximation the dispersion relation will look like shown in Fig. 1.2. For comparison the dispersion relation of light in dielectric is also shown (noted as a light line). One of the consequences of the dispersion relation of SPPs is that their frequency

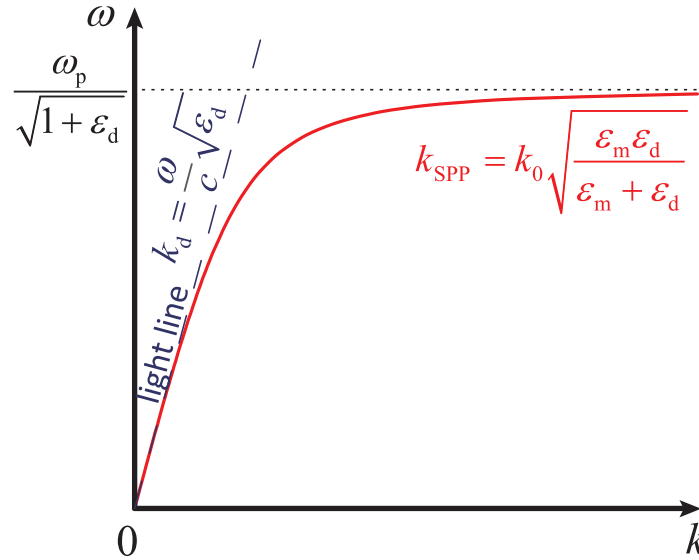


Figure 1.2: Dispersion relation for SPP (red line) and light in dielectric (blue line).

range is limited, and when their wave vector goes to the infinity, the frequency approaches finite value. At such limit the group velocity approaches zero, therefore the mode acquires electrostatic character and called surface plasmons. Another consequence is that the dispersion relation doesn't cross a light line (except origin) and  $k_{\text{SPP}}$  is always larger than the wave-vector in the dielectric. That means the impossibility of exciting SPP with a simple illumination of the metal-dielectric interface.

Since the real metals have both real and imaginary part of the permittivity constant (meaning the presence of damping or Ohmic losses), the propagation constant is also in general a complex value. Its real part shows the phase gain along the propagation and it is usually represented in terms of the effective mode index  $N_{\text{eff}}$  and SPP wavelength  $\lambda_{\text{SPP}}$ :

$$N_{\text{eff}} = \frac{\text{Re}[k_{\text{SPP}}]}{k_0}, \quad \lambda_{\text{SPP}} = \frac{2\pi}{\text{Re}[k_{\text{SPP}}]} = \frac{\lambda_0}{N_{\text{eff}}}, \quad (1.6)$$

where  $\lambda_0 = 2\pi/k_0$  is a free-space wavelength. The imaginary part of the propagation constant creates an exponential decrease (decay) of the SPP field along the propagation direction. It is caused by the Ohmic losses in metal, therefore usually noble metals, such as gold and silver, are used for plasmonic applications.

The distance along the propagation direction, where the intensity of SPP mode drops by a factor of  $1/e$ , is called a propagation length, and is equal to:

$$L_{\text{prop}} = \frac{1}{2 \text{Im}[k_{\text{SPP}}]} \quad (1.7)$$

The Fig. 1.3 below shows the parameters of metal/air SPPs of real metals (relative permittivity of metals are taken from [7]). The above definitions of the

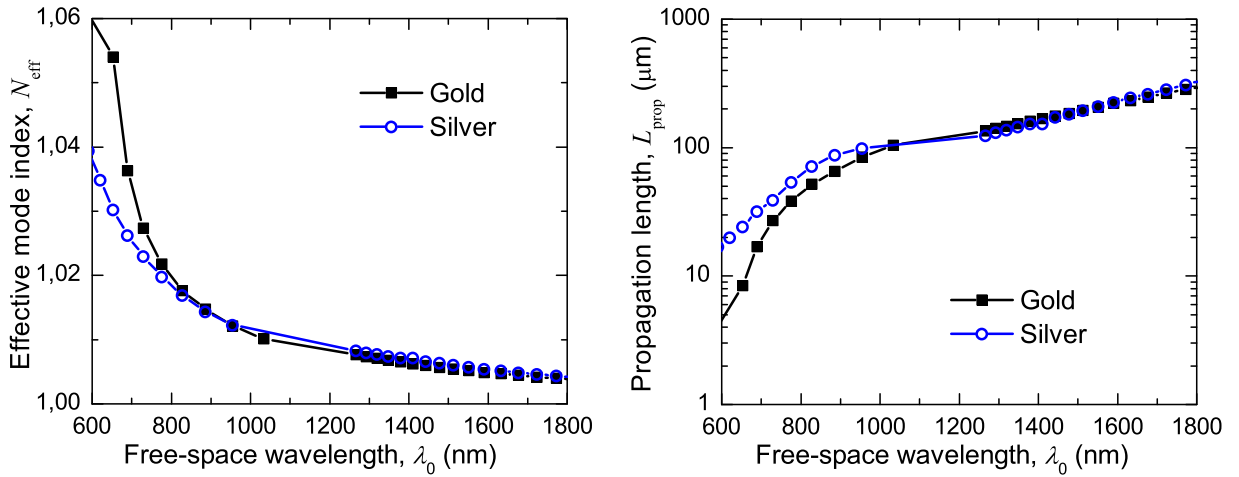


Figure 1.3: The effective mode index and propagation length for gold/air and silver/air SPP.

effective mode index and the propagation length are universal for any propagating mode. It is seen from Fig. 3 that the effective mode index of SPP is close to the refractive index of dielectric. However, by modifying the geometry of the waveguide, one can substantially increase it, thought with a price of decreased propagation length [8]. Overall, there is a known trade-off between the field confinement/effective mode index and the propagation length [9].

## 1.2 Long- and short-range SPPs

Let's now consider more complicated case, where two metal-dielectric interfaces are present. Such systems can be considered as two interacting SPP modes, and the distance between two interfaces will influence the strength of such interaction. There are two possibilities of such structures: insulator-metal-insulator (IMI) and metal-insulator-metal (MIM) systems. Let's start with the first one: a metal film of thickness  $t$  sandwiched between two dielectrics. For simplicity let's assume the same dielectric on both sides of the metal film. Then, similar to SPP, the  $H$ -field distribution in each media can be written as:

$$H_y(x, z) = e^{ik_{\text{SPP}}x} \begin{cases} C_1 e^{-k_z^d |z - \frac{1}{2}t|}, & z > \frac{1}{2}t \\ C_2 e^{-k_z^m |z - \frac{1}{2}t|} + C_3 e^{-k_z^m |z + \frac{1}{2}t|}, & -\frac{1}{2}t < z < \frac{1}{2}t \\ C_4 e^{-k_z^d |z + \frac{1}{2}t|}, & z < -\frac{1}{2}t \end{cases} \quad (1.8)$$

The boundary conditions, together with a symmetry of the system, leads to two solutions: symmetric ( $C_1 = C_2 = C_3 = C_4$ ), also known as a long-range (LR) SPPs; and asymmetric ( $C_1 = C_2 = -C_3 = -C_4$ ), known as a short-range (SR) SPPs. Again, similarly to the simple SPPs, the boundary conditions lead to the following dispersion relations:

$$\text{LR - SPP : } \tanh\left(\frac{1}{2}k_z^m t\right) = -\frac{k_z^d \varepsilon_m}{k_z^m \varepsilon_d}, \quad (1.9)$$

$$\text{SR - SPP : } \tanh\left(\frac{1}{2}k_z^m t\right) = -\frac{k_z^m \varepsilon_d}{k_z^d \varepsilon_m}. \quad (1.10)$$

These two equations cannot analytically derive a direct expression for the propagation constant, but they can easily be solved numerically, for example, by using iterative methods [10]. Results of such calculation for air-gold-air configuration are shown in Fig. 1.4 (relative permittivity of metal is taken from [7]). One can see that the larger the thickness  $t$  of metal film, the closer the parameters of both modes to one-interface SPP mode. However, when the film thickness is sufficiently small, SPP splits in LR- and SR-modes. LR-SPP is characterized by a long propagation length (that reflects its name) and weak field confinement (effective mode index close to the refractive index of dielectric). On the contrary, SR-SPP has strong field confinement (large effective mode index), but its propagation length becomes smaller. This can be considered as an example of the abovementioned trade-off between the field confinement and the propagation length [9]. It can be used as an advantage: for a particular application one can choose the important property (either high field confinement of the propagation length) and then fabricate a proper waveguide.

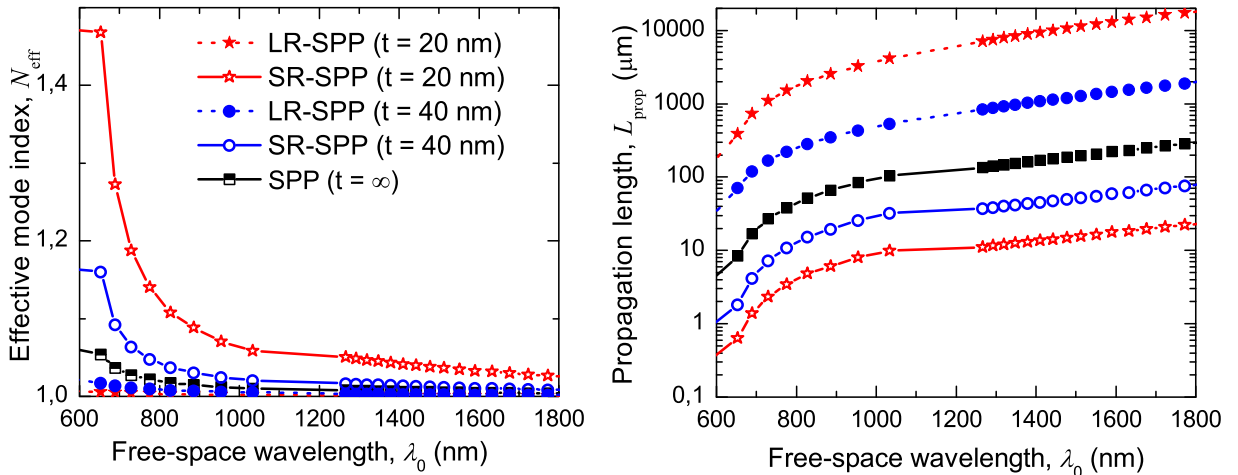


Figure 1.4: The effective mode index and propagation length of LR- and SR-SPP for air/gold/air configuration.

Thus the fundamental plasmonic modes in the symmetric IMI structures were considered. A case with asymmetric environment (i.e., when there are different dielectrics around metal film) is more complicated since a non-confined mode

(with a radiation propagating away from the film) becomes available as one of the solution. In other words, SPP start to leak to the dielectric with higher refractive index, the so-called leakage radiation, acting as additional losses. However, such radiation is a key concept in leakage radiation microscopy [11], used to study plasmonic modes.

### 1.3 Gap surface plasmons

As noted above, another two-interface configuration is a metal-insulator-metal system (or, simply, a dielectric gap in metal). Again, let's assume the same metal. Then the field distribution is similar to the previously considered IMI systems, with an interchange of  $\varepsilon_m$  and  $\varepsilon_d$ . However, the study of the dispersion relations of two modes reveals that only one mode does not have a cut-off. In other words, for a relatively thin dielectric gap only one of the modes gives a meaningful solution. Such mode is called gap surface plasmons (GSP), and its dispersion relation is described by the following:

$$\text{GSP : } \tanh\left(\frac{1}{2}k_z^d t\right) = -\frac{k_z^m \varepsilon_d}{k_z^d \varepsilon_m}, \quad (1.11)$$

where  $t$  is a thickness of the dielectric gap. Again, the analytical solution for the propagation constant is impossible, but it can be solved approximately [12] or numerically. Results of such calculation for air gap in gold are shown in Fig. 1.5 (relative permittivity of metal is taken from [7]).

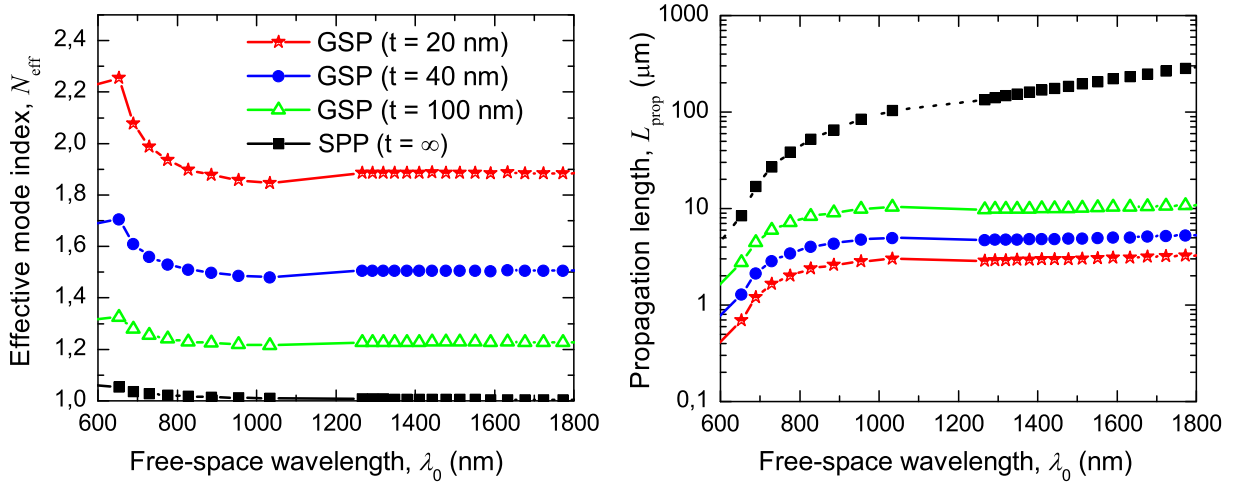


Figure 1.5: The effective mode index and propagation length of GSP for gold-air-gold configuration.

One can see that the thicker the gap, the closer the propagation constant of GSP to SPP (similar to IMI structures). However, for relatively small gaps the field becomes strongly confined, thus increasing effective mode index and reducing the propagation length. Overall it behaves similar to SR-SPP, but they have a fundamental difference - in case of GSP SPPs of each metal-dielectric interface

are coupled through the dielectric gap, while in SR-SPP case they are coupled through the metal film. Also one can notice slightly larger propagation length of GSP compared to SR-SPP with the same effective mode index, making them highly attractive for many applications.

## 1.4 SPP waveguides

The previous two sections described basic planar metal-dielectric configuration, allowing the guiding of plasmonic modes. Real plasmonic waveguides, where the plasmonic mode is confined in two dimensions and propagates along the third dimension, are usually based on one of the above basic configurations, therefore the properties of plasmonic waveguides can be predicted by comparing to SPP, LR-, SR-SPP or GSP modes. Then let's overview the plasmonic waveguides studied in this project: channel plasmon-polariton (CPP), long-range dielectric-loaded SPP (LR-DLSPP) and slot waveguides.

CPP are electromagnetic waves that are bound to and propagate along the bottom of V-shaped grooves milled in a metal film. They have been first predicted [13, 14] and then experimentally shown [15] to exhibit useful subwavelength guiding properties. Their unique features of strong SPP mode confinement make it possible to bend (and split) CPP waveguides (CPPWs) formed in the materials with extremely small curvature [16]. CPPs have already been found suitable for realization of many passive photonic devices [17], and may find important applications as basic building blocks in ultrahigh-speed all-optical signal processing circuits [4].

For a relatively small angle of V-groove CPPW can be considered as a GSP waveguide with a variable gap width. Such consideration allows for approximate analytical solution of dispersion properties of CPP for infinitely deep V-grooves [18, 19]. Another quasi-analytical approach is the effective index method (EIM), which can be used for finite depth V-grooves [20]. Finally, the field distribution, propagation constant and other properties of CPP can be found directly by using special software (in these project COMSOL was used). On the other hand, CPP properties can be found experimentally, for example, using scanning near-field optical microscopy (SNOM). The result of experimental investigation of CPP, supported by V-shaped grooves in gold with the angle of  $\sim 17^\circ$  and depth of  $\sim 1.7 \mu\text{m}$  at telecommunication wavelength range (1425-1625 nm) is presented in Fig. 6. It shows that the propagation length increases with the increase of the free-space wavelength or with the increase of the groove angle. The inset depicts the field magnitude distribution calculated analytically for the infinitely deep groove and numerically, using a finite element method (FEM) implemented in COMSOL, for a finite-depth groove at different excitation wavelengths. The result shows that with the increase of the wavelength the field is pushed away from the groove, thus decreasing confinement. One would expect that there should be

a certain cutoff threshold ( $\lambda_{\text{cut}} > 1630$  nm) after which the CPP mode can no longer be confined within the groove, and is radiated in the form of SPPs along the contiguous horizontal metal surfaces. It is also observed that as the wavelength increases (i.e., approaching to cutoff), the CPP modes became hybridized with the modes running on the edges at both sides of the groove (e.g., calculations show rather strong hybridization of the CPP mode at  $\lambda = 1630$  nm even though it is still mainly confined within the groove walls).

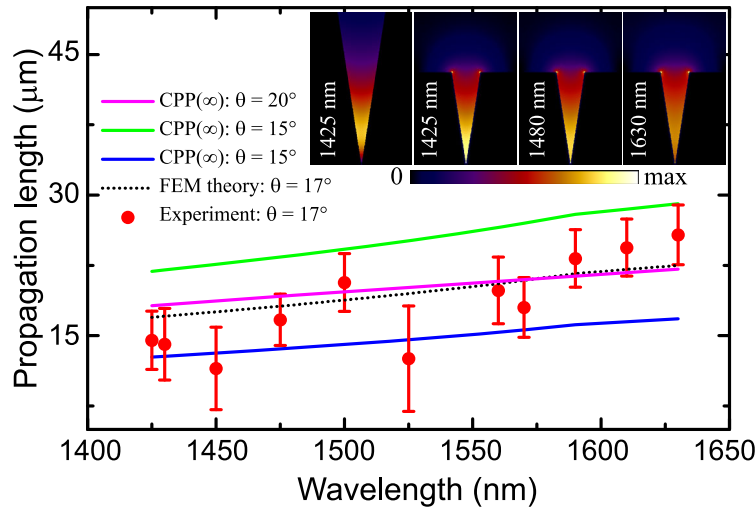


Figure 1.6: CPP propagation length as a function of free-space wavelength. Insets (time-averaged electric field magnitude distributions) represent the modal structure of the fundamental CPP modes at indicated wavelengths. Inset size is  $2 \mu\text{m} \times 3 \mu\text{m}$ .

Overall CPPs comprise all useful GSPs properties, i.e., strong field confinement with relatively small propagation losses, and they overcome GSPs in broader tunability (two parameters of CPP - groove angle and groove width/depth - can be varied, compared to one parameter of GSP - gap thickness). A weak point in CPP-based utilization is fabrication complexity - for long time the only option for fabrication was focused ion beam (FIB) technic, which is rather expensive and slow. However, recently a new process, involving UV-lithography and crystallographic silicon etching, was developed and proved [21], allowing relatively fast and cheap CPP fabrication.

As described in previous sections, LR-SPPs are characterized by long propagation length and weak field confinement. In order to better confine plasmonic mode without losing propagation length, one can use a proper dielectric environment, similar to photonic waveguides. Such concept is implemented in long-range dielectric-loaded SPP (LR-DLSPP) waveguides, where a thin metal stripe is sandwiched between a high-refractive-index dielectric ridge and dielectric layer, deposited directly on a low-refractive-index substrate (Fig. 1.7). It has been shown that LR-DLSPP waveguides able to guide a plasmonic mode over millimeter-long distances [22], while retaining relatively strong mode confinement (similar to diffraction-limited photonic waveguides, i.e.,  $\sim \lambda$ ). The usage of LR-DLSPPW-based components seems very promising for many practical applications, such as

active modulation and bridging electric and optical circuits.

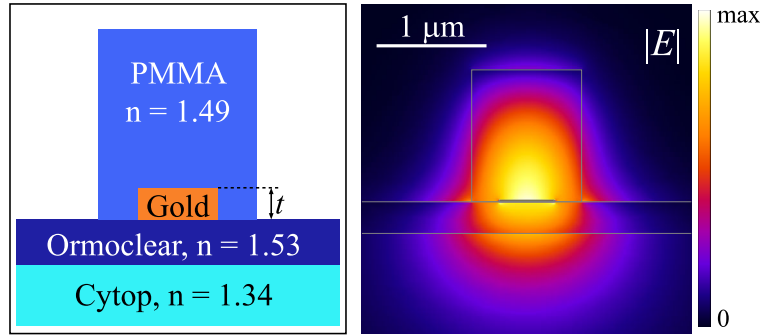


Figure 1.7: Schematic layout and mode distribution of LR-DLSPP at  $\lambda = 1500$  nm. Thickness of the gold stripe  $t = 15$  nm.

Another configuration mimicking GSP waveguide is a slot waveguide [23], where the plasmonic mode is supported by a slot (gap) in a metal film deposited on dielectric substrate (Fig. 1.8). In such configuration the geometric parameters of the slot plays a key role in supported mode properties: for a relatively small width  $w$  of the slot compared to the film thickness  $t$  the field profile is similar to GSP and highly concentrated in the slot (see middle image in Fig. 8, calculated for  $w = 50$  nm,  $t = 100$  nm, metal - gold and dielectric - silica,  $n = 1.44$ ). Similar to GSP, such mode has high effective mode index and small propagation length (for the calculated parameters  $N_{\text{eff}} = 1.53$  and  $L_{\text{prop}} \approx 6 \mu\text{m}$ ). When the gap width increases (or when the metal thickness decreases), the mode loses its confinement, with a correspondent decrease in the mode effective index and increase in the propagation length (see rightmost image in Fig. 8 as an example, calculated for  $w = 100$  nm and  $t = 50$  nm, resulted in  $N_{\text{eff}} = 1.47$  and  $L_{\text{prop}} \approx 8 \mu\text{m}$ ). With a further decrease of confinement, the effective mode index continue to decrease and at certain point it becomes less than the one of SR-SPP, and slot mode starts to leak to SR-SPPs. This introduces additional losses and reduces the propagation length. Thus the optimal parameters for either strong field confinement or long propagation length can be found. Another advantage of slot plasmonic waveguides is relatively easy fabrication.

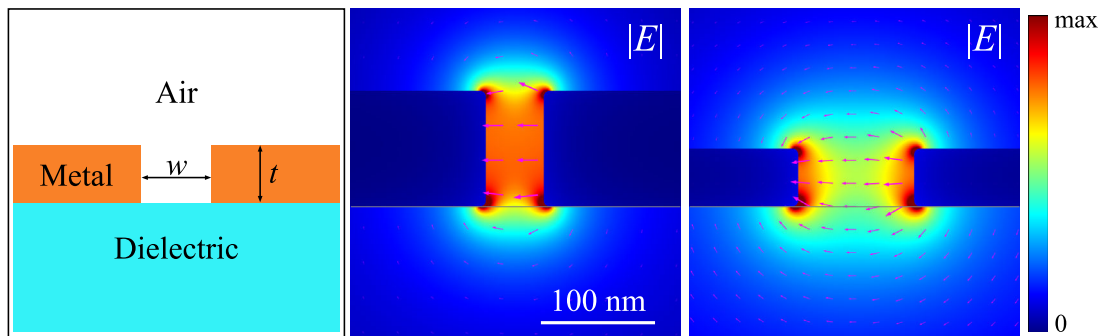


Figure 1.8: Schematic layout and mode distribution of slot plasmonic mode at  $\lambda = 1500$  nm. Arrows represent in-plane electric field components.





# Chapter 2

## Scanning near-field optical microscopy

---

Since SPPs, as all other propagating plasmonic modes, are electromagnetic waves bound to the metal-dielectric interface, an obvious problem of the investigation and characterization of such modes arise. Usual devices, such as optical microscopes, are based on detection of free-space propagating waves (light), so they become useless for the detection of evanescent waves, characterized by rapid amplitude decay in one or more direction of space. Therefore several new technics have been developed for visualization and detection of the propagating plasmonic waves: electron energy-loss spectroscopy [24, 25], fluorescence mapping [26], photoemission electron microscopy [27], and leakage radiation microscopy [11, 28]. They allow the investigation of plasmonic modes, but all of them are indirect methods. However, the most natural technique that allows probing near fields of plasmonic modes (both propagating and localized) with sub-wavelength resolution beyond the diffraction limit is a scanning near-field optical microscopy (SNOM) [29]. The next sections describe basic principles of near-field microscopy and two types of SNOM used in this project.

### 2.1 General principles of near-field microscopy

The basic principle of SNOM is to put a tiny probe in a close proximity to the sample, which will scatter the oscillating evanescent field in usual free-space propagating waves, which can be detected by usual means (Fig. 2.1). In such way local information of the evanescent field is retrieved from one point. By applying a point-by-point scanning, the whole map of the near-field can be obtained.

The ability to detect evanescent waves also increases the resolution of SNOM beyond the diffraction limit intrinsic to usual optical microscopy. This can be explained by the Heisenberg's uncertainty principle:

$$\Delta x \Delta k_x \approx 2\pi, \tag{2.1}$$

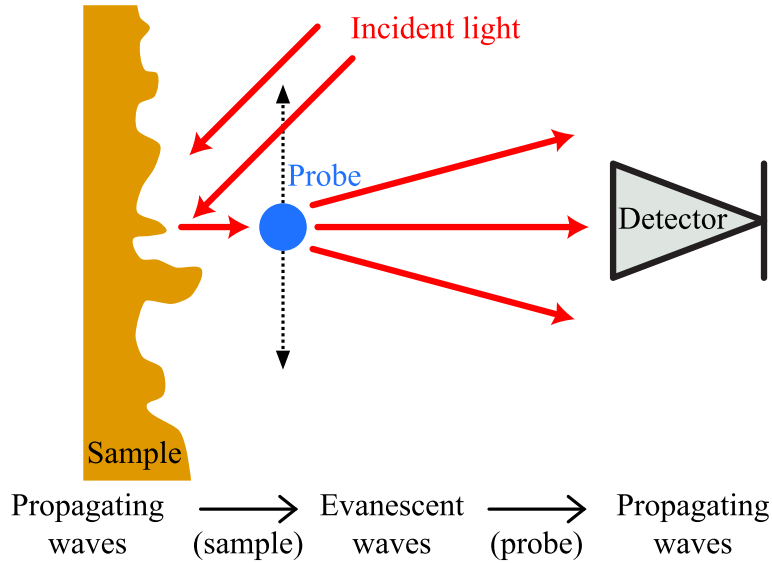


Figure 2.1: Basic principle of SNOM.

where  $\Delta x$  is a lateral resolution and  $\Delta k_x$  is a lateral component of  $k$ -vector detected by device. In usual optical microscopy  $\max[\Delta k_x] = k_0 = 2\pi/\lambda$ , therefore the lateral resolution is limited by the wavelength. Evanescent waves, however, have at least one imaginary  $k$ -vector component (resulting in exponential decay of the field away from the interface), therefore the lateral component of  $k$ -vector can be larger than a magnitude of the correspondent free-space  $k$ -vector  $k_0$ . Thus SNOM (or any other device capable of detecting evanescent wave) can have a subwavelength resolution.

There are many different types of SNOM probes and detection schemes, which results in a number of particular SNOM setups available today. Here only two of them are considered since they were used for the research done during this PhD project: apertureless fiber-based SNOM (also known as a photon scanning tunneling microscopy or collection SNOM) and scattering-type SNOM (s-SNOM). However, before going into details, one should keep in mind the problem of transfer function, which allows one to relate an image and an object, presuming the process of image formation is linear. In other words, one should know how to relate a measured data point to the electromagnetic field ( $\mathbf{E}$ ,  $\mathbf{H}$ ) at the correspondent point on the sample. The transfer function strongly depends on the type of SNOM, therefore it will be discussed in details in corresponding sections.

## 2.2 Apertureless fiber-based SNOM

The fiber-based SNOM uses a sharp tapered optical fiber as a probe. Such fiber can be coated by a thin (10-100 nm) metal layer with a small aperture at the tip in order to increase the resolution and/or to enhance the selectivity on the

detection of particular field components. An uncoated fiber tip, usually referred as an apertureless, provides a much higher optical signal compared to the coated fiber tip. The detected signal in the fiber-based SNOM is usually the light, scattered by the tip inside the fiber (therefore such setup is sometimes referred as a collection SNOM), so the detector is simply connected to the other end of the fiber. The excitation of plasmonic modes can be done in different ways: prism coupling in the Kretschmann [30] and Otto [31] configuration; by the use of grating; coupling from the edge (end-fire coupling); excitation on defects; and by illuminating from the same fiber tip used as a SNOM probe.

The schematic layout of the experimental setup used in this PhD project is shown in Fig. 2.2. The end-fire excitation of plasmonic waveguides is done with a use of a tapered-lensed polarization-maintaining single-mode fiber, focusing tunable telecom (1425–1625 nm) TE/TM-polarized radiation to a spot of diameter of approx.  $3 \mu\text{m}$  at the entrance of the waveguide. The setup also allowed an easy replacement of the SNOM head with a far-field microscopic arrangement, including a  $20\times$  objective and a telecom camera. It was used both for the alignment of the in-coupling fiber and for the observation of the propagating mode, since the evanescent field of the mode was scattered on the defects due to the imperfections.

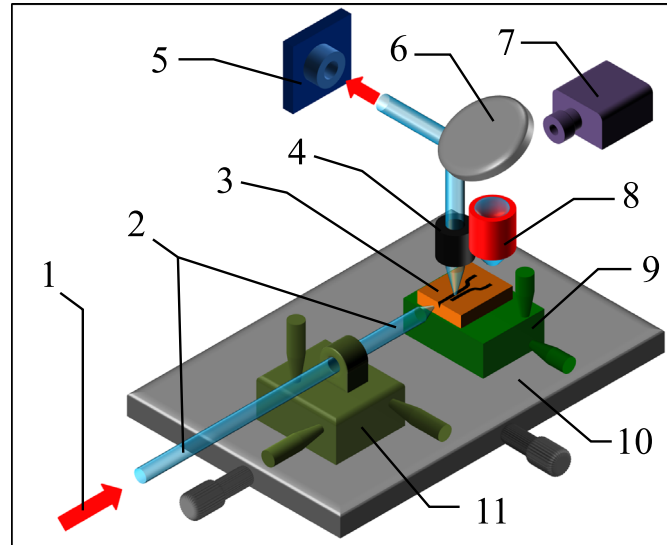


Figure 2.2: Apertureless fiber-based SNOM setup: (1) incoming TE/TM-polarized radiation from tunable laser; (2) polarization-maintained fiber with a tapered-lensed end used to couple light to waveguiding mode; (3) sample; (4) SNOM probe with its positioning system; (5) femto-watt InGaAs photoreceiver; (6) mirror; (7) telecom camera; (8)  $20\times$  objective; (9,10,11) 2- and 3-dimensional stages.

Tapered fiber tip, used as a SNOM probe, was made from a single-mode silica fiber by  $\sim 2$  hours tube etching (i.e. in plastic jacket) of a cleaved fiber in 40% hydrofluoric acid with a protective layer of olive oil [32]. After the etching the plastic jacket was removed by softening it in a dichloromethane and mechanical removal. The resulting fiber tip had a cone angle of  $\sim 30^\circ$  and curvature radius

of  $\sim 100$  nm (Fig. 2.3). It should be noted that such process of tip fabrication is somewhat uncontrollable, so the resulting angle and curvature radius may vary from tip to tip. Moreover, sometimes multiple tips were produced (as can be seen in the middle image of Fig. 2.3), resulting in a multiple/self-duplicating SNOM images.

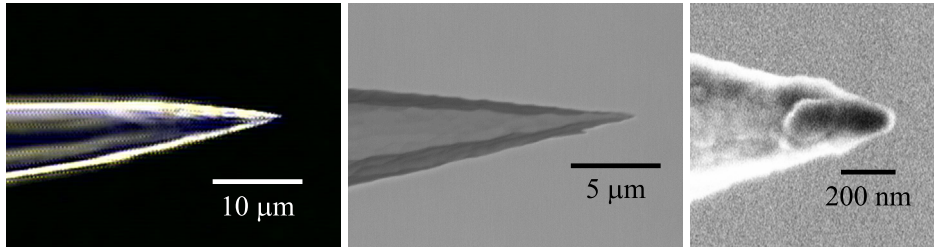


Figure 2.3: Tapered fiber tip, produced by tube etching, at different magnifications (left - optical dark-field microscope image, middle and right - scanning electron microscope (SEM) images).

The fiber tip was glued to the SNOM probe holder containing 2 piezoelectric elements – one was exciting the transverse oscillation of the tip, and another was reading the amplitude of oscillation. The oscillation frequency was  $\sim 150$  kHz with a Q-factor of  $\sim 100$ . Approaching the sample the amplitude of oscillations drops due to the shear-force damping, therefore, by using such shear-force feedback, the tip-sample distance was kept constant of about few nanometers. The near-field radiation has been scattered and partially collected by the fiber tip itself, and afterwards guided (in the form of fiber modes) towards the other end of the fiber, where it has been detected by the femtowatt InGaAs photoreceiver and processed by SNOM controller (providing both topographical and near-field optical images, simultaneously).

As for the transfer function, first of all one should bear in mind that apertureless fiber-based SNOM measures dominantly in-plane electric field component, since the field scattered by the probe should be collected by the fiber, which guides only transverse modes, parallel to the sample surface due to the normal position of the probe. The scattered out-of-plane (normal) components of the near-field are thus not scattered normally (with in-plane field components) due to the symmetry of the tip. However, the normal component of the near-field can be measured with SNOM, if the tip is not symmetrical (for example, see middle image in Fig. 11). Another aspect of transfer function of apertureless fiber-based SNOM is a finite size of the probe and correspondent response, which is dependent on the decay rate of evanescent field. In other words, the more confined the near-field, the less it is detected by SNOM. A systematic experimental study of the SNOM transfer function, supported by a simple analytical model, results in a simple empirical rule: the detected signal is proportional to the near-field in-plane component at certain effective point inside the tip, which is  $\sim 150$  nm away from the tip apex [33, 34].

## 2.3 Scattering-type SNOM

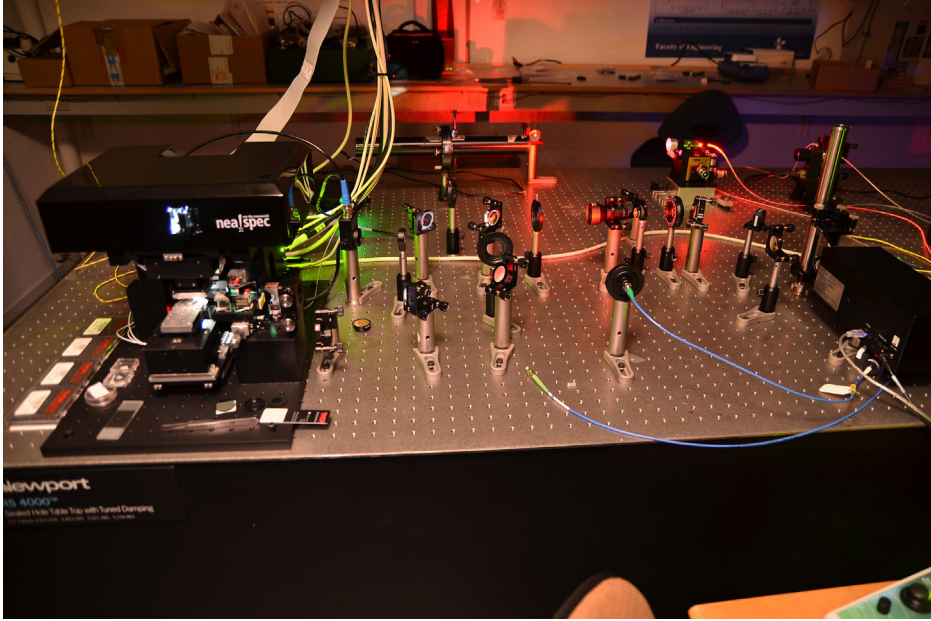


Figure 2.4: Photo of NeaSpec s-SNOM setup.

The scattering-type SNOM used in this project is based on an atomic force microscope (AFM) and uses cantilevered tips as near-field probes (NeaSNOM from Neaspec GmbH, see Fig. 2.4). In the experiments standard commercial Si tips covered with platinum (Arrow NCPT, NanoWorld) were used. The sample is scanned in a tapping mode, with the tip oscillating at the mechanical resonance frequency  $\Omega \approx 250$  kHz with an amplitude  $\sim 50$  nm (Fig. 2.5). The sample is illuminated from the bottom with a use of a lower parabolic mirror for focusing the light to the spot of diameter around  $3 \mu\text{m}$  (so-called transmission-mode, [35]). The light, scattered by the tip, is collected by a top parabolic mirror and directed towards the detector, where it is overlapped with an interfering reference beam, yielding both the amplitude and the phase of the scattered light using pseudoheterodyne detection [36] (see next section about phase detection). It should be noted that the setup is, in principle, wavelength-free due to the use of parabolic mirrors instead of refractive lenses. Only few minor components, such as beam splitters and polarizers, require the replacement with a substantial change of the illumination wavelength. Background contributions from far-field and scattering of the incident light on the tip and cantilever were suppressed by demodulating the detector signal at a high harmonic frequency  $n\Omega$  (usually  $n = 2$  or  $3$  is used), providing background-free near-field amplitude and phase images [37].

In most s-SNOM setups the illumination is done in reflection-mode, where the light is focused on the tip with the same top parabolic mirror that collects

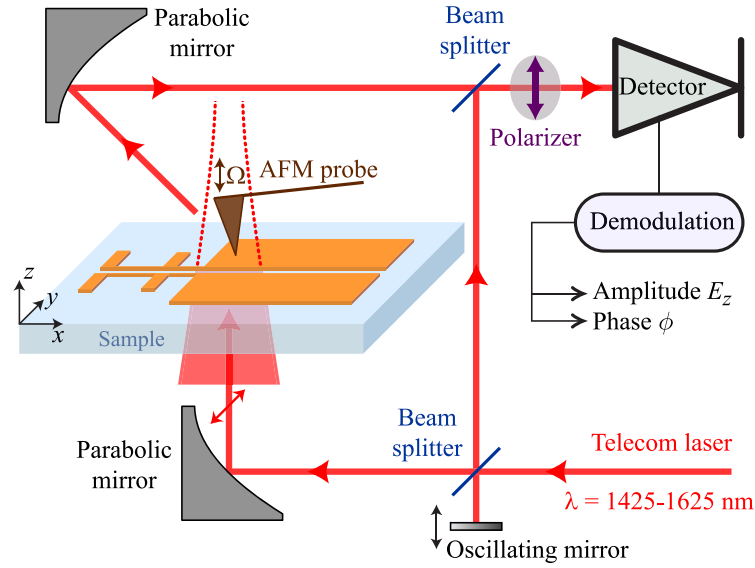


Figure 2.5: Apertureless fiber-based SNOM setup with pseudoheterodyne amplitude- and phase-detection.

scattered light. Such configuration is useful for the subwavelength sampling of material properties [37–39], but it creates many problems observing clear antenna modes and treatment of data due to a strong tip-sample coupling [40] and phase-retardation effects [41]. However, in the transmission-mode configuration the sample is illuminated from below, with an in-plane direction of polarization. Therefore such configuration produces homogeneous illumination and efficient excitation of the antenna, avoiding direct excitation of the tip [35, 42]. Due to a dominating dipole moment of a tip along its axis (i.e., along  $z$ -axis), the recorded s-SNOM images represents mostly a distribution of the amplitude and phase of the  $z$ -component of the electric field,  $E_z$  [43, 44]. In order to enhance this selectivity, a polarizer at the detector is set correspondently to  $z$ -polarization of the light, scattered by the tip. Finally, the recorded data is imaged with free scanning probe microscopy software Gwyddion.

# Chapter 3

## Amplitude- and phase-resolved detection

---

The basic idea behind the detection of the phase is to use the interference of signal beam with a reference beam, since the absolute value of the phase is practically useless (the measured signal is always proportional to the mean electric field intensity over the period of oscillations), so only the relative phase difference, creating interference pattern in space or time, can be measured. Therefore in all phase detection methods described later the in-coming laser beam is split in two arms: reference and signal (sample) arm, overlapping later at the detector. The detected signal – intensity – is proportional to the square of the amplitude of the total electric field  $E_{\text{total}}$ , so one can write is as:

$$\begin{aligned} I &\propto |E_{\text{total}}|^2 = |E_{\text{signal}} + E_{\text{ref}}|^2 \\ &= |E_{\text{signal}}|^2 + |E_{\text{ref}}|^2 + E_{\text{signal}}E_{\text{ref}}^* + E_{\text{signal}}^*E_{\text{ref}} \\ &= |E_{\text{signal}}|^2 + |E_{\text{ref}}|^2 + 2|E_{\text{signal}}||E_{\text{ref}}|\cos(\phi_{\text{signal}} - \phi_{\text{ref}}), \end{aligned} \quad (3.1)$$

$$E_{\text{signal}} = |E_{\text{signal}}|\exp(i\phi_{\text{signal}}), \quad E_{\text{ref}} = |E_{\text{ref}}|\exp(i\phi_{\text{ref}}), \quad (3.2)$$

where  $E_{\text{signal}}$  and  $E_{\text{ref}}$  are the electric field in the signal and reference arm, correspondingly, and star means complex conjugate. Only the interference term contains valuable information about the phase, therefore, in order to measure it, one needs to apply the modulation to the signal beam,  $\text{mod}_{\text{signal}}$ , and reference beam,  $\text{mod}_{\text{ref}}$ , and then demodulate the detected signal at ‘crossed modulation’ -  $\text{mod}_{\text{signal}}\text{mod}_{\text{ref}}$ . The phase detection methods differ by the modulation/demodulation procedure, and sometimes it is enough to modulate beam in only one arm (usually reference arm). Before proceeding to the particular phase detection methods, one should keep in mind that the intensity in the signal arm of AFM-based s-SNOM is already modulated by tip’s oscillation frequency  $\Omega$ . Therefore in general case one can write the electric field in the signal arm ex-

panded in Fourier series:

$$E_{\text{signal}} = \sum_{m=-\infty}^{\infty} S_m \exp(im\Omega t), \quad (3.3)$$

where  $S_m$  is a complex-valued Fourier coefficients. Such general consideration is rather complicated, but it can be simplified due to the fact that only the scattered near-field ENF strongly depends on the tip-sample distance, while the far-field EFF (background) does not. Therefore the electric field in the signal arm can be simplified as:

$$\begin{aligned} E_{\text{signal}} &= E_{\text{NF}} + E_{\text{FF}}, \\ E_{\text{NF}} &= |E_{\text{NF}}| \cos(\Omega t) \exp(i\phi_{\text{NF}}), \\ E_{\text{FF}} &= |E_{\text{FF}}| \exp(i\phi_{\text{FF}}). \end{aligned} \quad (3.4)$$

In practical case, the far-field might still have reasonable amplitude of the first harmonic, but the following rule holds: the higher the harmonics, the larger the near-field to far-field amplitude ratio, so high-order harmonics are used in experiments (in the case of this thesis 2<sup>nd</sup> and 3<sup>rd</sup> harmonics were used). The amplitude of the signal drops down with the increase of harmonic order, therefore the optimum is found in a trade-off between near-field to far-field ratio and signal-to-noise ratio. It should be noted that in the equation above the cosine function is used instead of the complex exponent for harmonic dependence, because mostly the amplitude of the scattered near-field depends on tip-sample distance, and the phase is nearly constant [38]. Therefore the detected signal for s-SNOM is:

$$\begin{aligned} I &= I_{\text{NF/NF}} + I_{\text{FF/FF}} + I_{\text{ref/ref}} + 2I_{\text{NF/FF}} + 2I_{\text{NF/ref}} + 2I_{\text{FF/ref}}, \\ I_{\text{A/A}} &\propto \frac{1}{2} (E_{\text{A}} E_{\text{B}}^* + E_{\text{A}}^* E_{\text{B}}); \end{aligned} \quad (3.5)$$

$$\begin{aligned} I &\propto |E_{\text{FF}}|^2 + |E_{\text{ref}}|^2 + 2|E_{\text{FF}}| |E_{\text{ref}}| \cos(\phi_{\text{FF}} - \phi_{\text{ref}}) + |E_{\text{NF}}|^2 \cos^2(\Omega t) \\ &\quad + 2|E_{\text{NF}}| \cos(\Omega t) \{ |E_{\text{ref}}| \cos(\phi_{\text{NF}} - \phi_{\text{ref}}) + |E_{\text{FF}}| \cos(\phi_{\text{NF}} - \phi_{\text{FF}}) \} \end{aligned} \quad (3.6)$$

Thus the ultimate goal of phase detection in s-SNOM is to measure the amplitude  $|E_{\text{NF}}|$  and phase  $\phi_{\text{NF}}$  of the background-free near-field.

### 3.1 Homodyne detection

The main idea in homodyne detection method (also known as phase shifting interferometry) is to make several consecutive measurements with different but well-controlled phases of the reference beam and then mathematically derive the amplitude and the phase. The phase shift is usually done by a controlled change of the optical path in the reference arm as shown in Fig. 3.1.



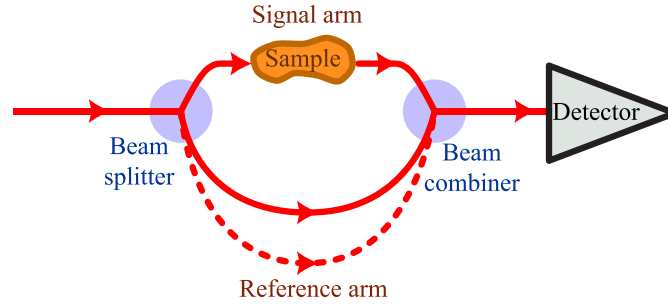


Figure 3.1: Homodyne detection scheme.

In case of AFM-based s-SNOM only 2 measurements are required, and the phase difference of  $90^\circ$  ( $\pi/2$ ) is usually taken. The measured intensity, demodulated at the frequency of  $\Omega$ , is equal to:

$$I_\Omega^{1,2} \propto 2 |E_{\text{NF}}| \left\{ |E_{\text{ref}}| \cos(\phi_{\text{NF}} - \phi_{\text{ref}}^{1,2}) + |E_{\text{FF}}| \cos(\phi_{\text{NF}} - \phi_{\text{FF}}) \right\} \quad (3.7)$$

Without limiting the generality we can assume the phase of the reference beam  $\phi_{\text{ref}}^1 = 0$  in the first measurements and  $\phi_{\text{ref}}^2 = \pi/2$  in the second. First, let's consider a case without background ( $E_{\text{FF}} = 0$ ). Then

$$\begin{cases} I_\Omega^1 \propto 2 |E_{\text{NF}}| |E_{\text{ref}}| \cos(\phi_{\text{NF}}), \\ I_\Omega^2 \propto 2 |E_{\text{NF}}| |E_{\text{ref}}| \sin(\phi_{\text{NF}}). \end{cases} \Rightarrow |E_{\text{NF}}| \exp(i\phi_{\text{NF}}) \propto I_\Omega^1 + iI_\Omega^2. \quad (3.8)$$

In such way the near-field amplitude and phase can be determined from two consecutive measurements. However, if the background is non-zero, it acts as an additive disturbance, making such measurements non-background-free. In order to discriminate this background, one can use either one or more additional measurements [45] or make the amplitude of the reference beam much higher than the one of the background. Another drawback of homodyne detection is a requirement for controlled phase shift – in a case of the change of the optical path in the reference arm it requires precise and repeatable positioners with close-loop accuracy much less than the wavelength. Then it becomes a trade-off between the detection speed and accuracy.

## 3.2 Heterodyne detection

The main idea in heterodyne detection method is to shift the optical frequency of the reference beam (Fig. 3.2). This can be done by either using acousto-optic modulator or simply by linear change of the optical path (= phase) of the reference arm. Then the electric field in the reference arm is:

$$E_{\text{ref}} = |E_{\text{ref}}| \exp [i(-Mt + \phi_{\text{ref}}^0)], \quad (3.9)$$

where  $M$  is the shift in the frequency and  $\phi_{\text{ref}}^0$  is the initial phase of the reference beam. Without limiting the generality  $\phi_{\text{ref}}^0$  can be set to zero. Then in general case the detected signal is:

$$I \propto |E_{\text{signal}}|^2 + |E_{\text{ref}}|^2 + 2 |E_{\text{signal}}| |E_{\text{ref}}| \cos(\phi_{\text{signal}} + Mt) \quad (3.10)$$

Therefore the amplitude and the phase of the signal beam can be found simply by demodulating the measured intensity with a frequency  $M$ .

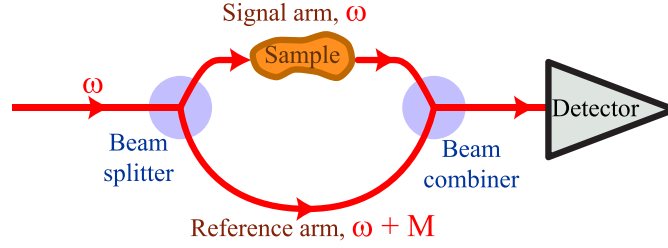


Figure 3.2: Heterodyne detection scheme.

In the case of s-SNOM the term of the detected signal corresponding to the interference of scattered near-field and the reference beam can be expressed as following:

$$\begin{aligned} I_{\text{NF/ref}} &\propto \frac{1}{2} (E_{\text{NF}} E_{\text{ref}}^* + E_{\text{NF}}^* E_{\text{ref}}) \\ &= 2 |E_{\text{NF}} \cos(\Omega t)| |E_{\text{ref}}| \cos(\phi_{\text{NF}} + Mt) \\ &= |E_{\text{NF}}| |E_{\text{ref}}| \{ \cos([M + \Omega] t + \phi_{\text{NF}}) + \cos([\Omega - M] t - \phi_{\text{NF}}) \} \end{aligned} \quad (3.11)$$

Therefore the amplitude  $|E_{\text{NF}}|$  and the phase  $\phi_{\text{NF}}$  of scattered near-field can be found by demodulating the detected signal with a frequency of  $|\Omega \pm M|$ . Since the detected signal will have harmonics at frequencies  $\Omega$ ,  $M$  and  $|\Omega \pm M|$ , then the minimum time required for one measurement is  $\sim 1/\min[\Omega, M]$ . Such detection method is background-free, however it has practical disadvantages: when acousto-optic modulator is used, the setup should be readjusted each time when the illumination wavelength is changed. When the linear positioner is used for the linear change of the optical path of the reference beam, then it should have high constant speed stability and very long travel range.

### 3.3 Pseudoheterodyne detection

Comparing the two detection methods described above one can see that the continuous modulation of the phase in the reference arm is better than a discrete phase shifting. However, the linear increase of the phase in the reference arm is hard to realize practically. The most straight-forward continuous modulation of the phase is a phase oscillation, which can be realized by mirror oscillation in the

reference arm, thus periodically changing the optical path of the reference beam (Fig. 3.3). Such approach is called pseudoheterodyne detection [36].

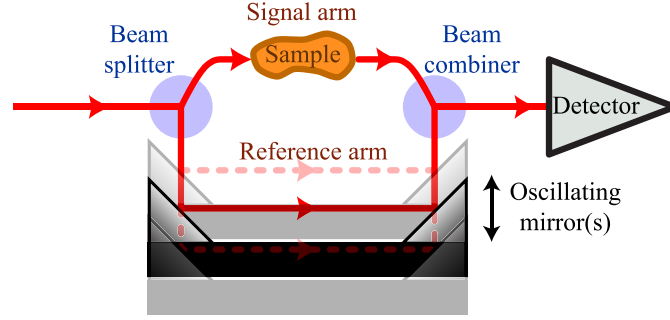


Figure 3.3: Pseudoheterodyne detection scheme.

The electric field in the reference arm can be written as

$$E_{\text{ref}} = |E_{\text{ref}}| \exp [i (\phi_{\text{ref}}^{\text{avg}} + \gamma \sin \{Mt\})], \quad (3.12)$$

where  $M$  is a phase-modulation frequency,  $\gamma$  is a modulation depth, and  $\phi_{\text{ref}}^{\text{avg}}$  is an average phase (corresponding to the equilibrium point). As in the previous case,  $\phi_{\text{ref}}^{\text{avg}}$  can be set to zero. The above equation can be expanded in Fourier series with Jacobi–Anger expansion:

$$\begin{aligned} E_{\text{ref}} &= |E_{\text{ref}}| \sum_{m=-\infty}^{\infty} J_m(\gamma) e^{imMt} \\ &= |E_{\text{ref}}| \left\{ J_0(\gamma) + 2 \sum_{m=1}^{\infty} J_m(\gamma) \cos [mMt] \exp (im\frac{\pi}{2}) \right\}, \end{aligned} \quad (3.13)$$

where  $J_m$  is the Bessel function of the first kind,  $m^{\text{th}}$  order. Thus the periodic oscillation of the phase can be interpreted as a multiple-heterodyning. Then the term of the detected signal corresponding to the interference of scattered near-field and the reference beam can be expressed as following:

$$\begin{aligned} I_{\text{NF/ref}} &\propto |E_{\text{ref}}| |E_{\text{NF}}| \cos(\Omega t) \left\{ J_0 \cos(\phi_{\text{NF}}) \right. \\ &\quad \left. + 2 \sum_{m=1}^{\infty} J_m(\gamma) \cos(mMt) \cos(\phi_{\text{NF}} - m\frac{\pi}{2}) \right\} \\ &= |E_{\text{ref}}| |E_{\text{NF}}| \left\{ J_0 \cos(\Omega t) \cos(\phi_{\text{NF}}) \right. \\ &\quad \left. + \sum_{m=1}^{\infty} J_m(\gamma) \cos(\phi_{\text{NF}} - m\frac{\pi}{2}) [\cos(\{mM + \Omega\}t) + \cos(\{mM - \Omega\}t)] \right\} \\ &= |E_{\text{ref}}| |E_{\text{NF}}| \sum_{m=-\infty}^{\infty} J_m(\gamma) \cos(\phi_{\text{NF}} - m\frac{\pi}{2}) \cos(\{mM + \Omega\}t) \end{aligned} \quad (3.14)$$

If  $\Omega \gg M$ , then the detected signal will split into sidebands with a frequency of  $\Omega \pm mM$ . From the above equation it follows that the successive lines in a sideband are in alternation proportional to the real (cos) and imaginary part (sin) of the complex near-field  $E_{\text{NF}}$ , for even and odd  $m$ , respectively. Consequently, it can be recovered from two signal amplitudes

$$|E_{\text{NF}}| \exp(i\phi_{\text{NF}}) \propto \frac{I_{\text{NF/ref}}^{\Omega+kM}}{J_k(\gamma)} + i \frac{I_{\text{NF/ref}}^{\Omega+lM}}{J_l(\gamma)} (-1)^{\frac{l-k-1}{2}}, \quad (3.15)$$

where  $k$  is an even and  $l$  is an odd integer. This equation can be simplified even further if  $J_k(\gamma)$  is made equal to  $J_l(\gamma)$  by a suitable choice of the modulation depth  $\gamma$ . For  $l = 1$  and  $k = 2$ , the required  $\gamma = 2.63$ . Then

$$|E_{\text{NF}}| \exp(i\phi_{\text{NF}}) \propto I_{\text{NF/ref}}^{\Omega+kM} - i I_{\text{NF/ref}}^{\Omega+lM} \quad (3.16)$$

As can be seen from the distribution of the Bessel functions (Fig. 3.4), at this point the energy is mostly concentrated at these sidebands, which corresponds to high efficiency of this detection method at this modulation depth.

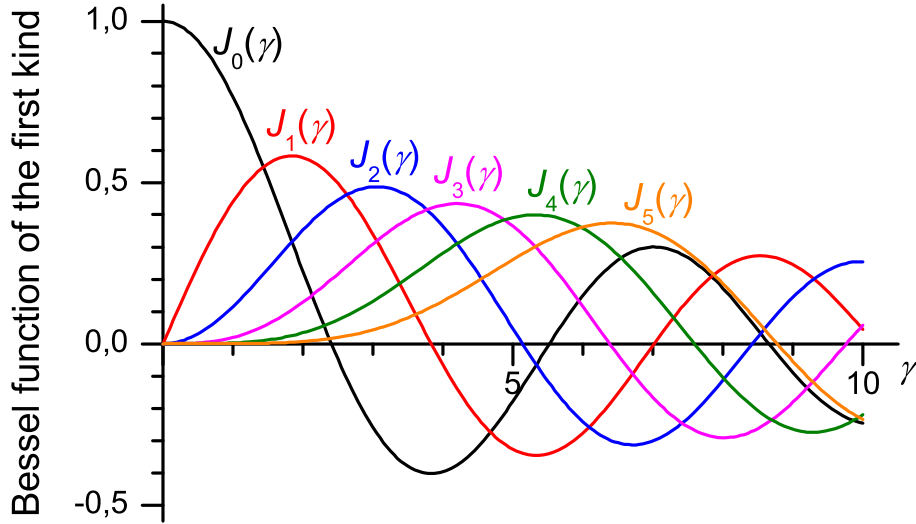


Figure 3.4: Bessel functions of the first kind and  $m = 0.5^{\text{th}}$  order.

In practical side of view it means that the detected signal in the Fourier space will have such sidebands around each harmonic  $n\Omega$ . It should be noted that only sidebands around non-zero harmonic represents background-free interference of the scattered near-field with the reference beam (Fig. 3.5). The minimum time required for one measurement is  $\sim 1/\min[\Omega, M]$ , as in previous case.

### 3.4 Synthetic optical holography

The final phase detection method developed specifically for scanning microscopes is relatively new [46] and combines phase shifting interferometry, heterodyne and

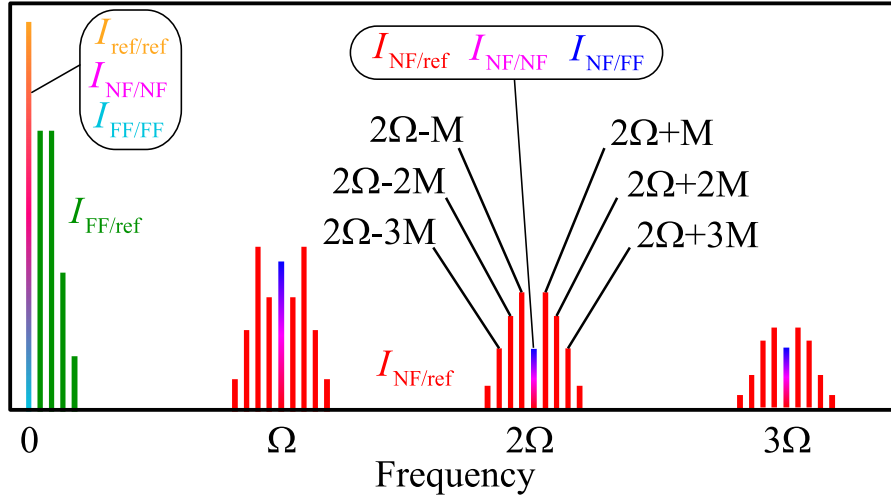


Figure 3.5: Schematic representation of the detector output spectrum.

holography technics. It applies phase modulation during the scan, therefore the scan map of the detected signal appears to be space-modulated, similar to the usual holography.

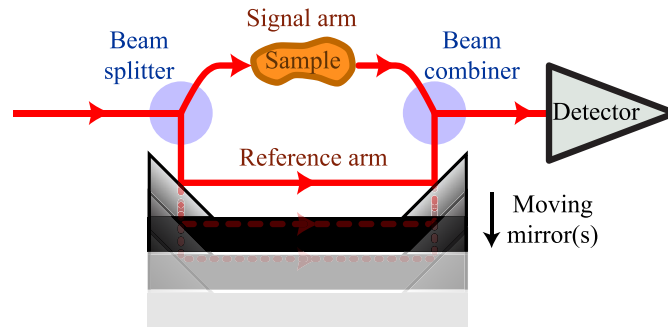


Figure 3.6: Synthetic optical holography detection scheme.

The basic practical realization of synthetic optical holography (SOH) is to linearly change the optical path of the reference beam (for example, by moving mirrors), similar to heterodyne method (Fig. 3.6). However, in this case it is not needed to demodulate the detected signal with a frequency of  $|\Omega \pm M|$  - only the demodulation at  $\Omega$  is required. Thus the time limit for one point detection is  $\sim 1/\Omega$  instead of  $\sim 1/\min[\Omega, M]$ , as in the case of heterodyne and pseudo-heterodyne. Since usually  $\Omega \gg M$  (for example, in NeaSpec s-SNOM used in this project  $\Omega \sim 250$  kHz and  $M \sim 150$  Hz), SOH enables substantial increase in data acquisition speed compared to other background-free techniques (heterodyne and pseudoheterodyne methods). As in the heterodyne method, the electric field in the reference arm can be written as

$$E_{\text{ref}} = |E_{\text{ref}}| \exp(iMt), \quad (3.17)$$

where  $M$  is the speed of the phase increase. If the phase change of the reference beam is negligible during one point detection (i.e.,  $\Omega \gg M$ ), then the detected signal, demodulated at frequency  $\Omega$ , is (similar to homodyne):

$$I_{\Omega} \propto 2 |E_{\text{NF}}| \{ |E_{\text{ref}}| \cos(\phi_{\text{NF}} - Mt) + |E_{\text{FF}}| \cos(\phi_{\text{NF}} - \phi_{\text{FF}}) \} \quad (3.18)$$

If we further neglect the phase change of the reference beam during the scan along the fast-axis  $x$  and assume the starting point of scan to be  $(0, 0)$ , then the time can be related to the slow-axis coordinate of the scan  $y$ :

$$t = \frac{y}{\Delta y} \Delta t_{\text{line}}, \quad (3.19)$$

where  $\Delta t_{\text{line}}$  is the scanning time of one line and  $\Delta y$  is the distance between lines. Then the scan map of the detected signal is:

$$\begin{aligned} I_{\Omega}(x, y) &\propto 2 |E_{\text{NF}}| \left\{ |E_{\text{ref}}| \cos\left(\phi_{\text{NF}} - M \frac{y}{\Delta y} \Delta t_{\text{line}}\right) + |E_{\text{FF}}| \cos(\phi_{\text{NF}} - \phi_{\text{FF}}) \right\} \\ &= 2 |E_{\text{NF}}| \left\{ |E_{\text{ref}}| \left( e^{-i\phi_{\text{NF}} + k_{\text{SOH}}y} + e^{i\phi_{\text{NF}} - k_{\text{SOH}}y} \right) \right. \\ &\quad \left. + |E_{\text{FF}}| \cos(\phi_{\text{NF}} - \phi_{\text{FF}}) \right\} \quad (3.20) \end{aligned}$$

where  $k_{\text{SOH}}$  is a wave vector of the synthetic wave:

$$k_{\text{SOH}} = \frac{M \Delta t_{\text{line}}}{\Delta y} \quad (3.21)$$

Usually the spatial resolution of detected near-field in SNOM is below the diffraction limit (i.e., less than a half of the wavelength), but it is still limited – for example, by a probe size of  $\sim 20$  nm. A wave vector of the synthetic wave  $k_{\text{SOH}}$ , on the other hand, is not limited and can be adjusted easily by increasing the number of lines or by changing the speed of scanning/phase change in the reference arm. Thus the amplitude and phase of the scattered near-field can be reconstructed by a standard Fourier transform (FT) filtering. With a relatively large  $k_{\text{SOH}}$  the Fourier spectrum of the scan map will represent three clusters, separated by  $k_{\text{SOH}}$  along the slow-axis. The filtering procedure is simply shifting and window filtering (or in the reverse order). In order to reconstruct the scattered near-field, the Fourier spectrum should be shifted by  $k_{\text{SOH}}$  in either positive or negative direction in Fourier domain, meaning the following change in real domain:

$$\begin{aligned} I_{\Omega}(x, y) e^{\pm k_{\text{SOH}}y} &\propto 2 |E_{\text{NF}}| |E_{\text{ref}}| e^{\pm i\phi_{\text{NF}}} \\ &+ 2 |E_{\text{NF}}| |E_{\text{ref}}| e^{\mp i\phi_{\text{NF}}} e^{\pm 2k_{\text{SOH}}y} + 2 |E_{\text{NF}}| |E_{\text{FF}}| \cos(\phi_{\text{NF}} - \phi_{\text{FF}}) e^{\pm k_{\text{SOH}}y} \quad (3.22) \end{aligned}$$

Then a window filtering should be applied in the Fourier domain in order to reconstruct the first term:

$$I_{\Omega}(x, y) e^{\pm k_{\text{SOH}}y} \xrightarrow[\text{transform}]{\text{Fourier}} \xrightarrow[\text{filtering}]{\text{Window}} \xrightarrow[\text{transform}]{\text{Inverse Fourier}} \propto 2 |E_{\text{NF}}| |E_{\text{ref}}| e^{\pm i\phi_{\text{NF}}} \quad (3.23)$$

In order to use SOH most efficiently, one should take into account that the bandwidth of the scan map is limited due to the discretization and is equal to  $2\pi/\Delta y$ . According to the above, it should fit three clusters separated by  $k_{\text{SOH}}$ . Then

$$\frac{2\pi}{\Delta y} \leq 3k_{\text{SOH}} = \frac{3M\Delta t_{\text{line}}}{\Delta y}; \quad (3.24)$$

$$M\Delta t_{\text{line}} \leq \frac{2\pi}{3} \quad (3.25)$$

It means that the most efficient SOH detection will be when the total change of the optical path in reference arm during the scanning time of one line is equal to one-third of the wavelength.

As for the spatial resolution of the reconstructed scan map of the scattered near-field, it is obvious that it will be lowered due to the window filtering in Fourier domain. The new resolution will be:

$$\Delta y^* = \frac{2\pi}{k_{\text{SOH}}} \leq 3\Delta y \quad (3.26)$$

It means that in most efficient SOH detection the spatial resolution will decrease by a factor of 3. It can also be interpreted as three points in original scan map are used to produce one point of background-free near-field reconstructed scan map – the same as for the phase shifting interferometry. Overall, SOH offers fast data acquisition of background-free near-field map. It also allows multicolor imaging, i.e. using several wavelengths and a single reference arm at the same time. As for the drawbacks, a practical application of SOH using linear positioner requires high accuracy on keeping constant speed and long travel range. However, the requirement on the accuracy is not so strict as in the case of homodyne and heterodyne, since slow drifts in position of the linear positioner will only affect the phase of the recovered near-field.





# Part II

---

Collection of papers



# Appendix A.1

CPP dispersion

---

## Dispersion of strongly confined channel plasmon polariton modes

Vladimir A. Zenin,<sup>1,\*</sup> Valentyn S. Volkov,<sup>2</sup> Zhanghua Han,<sup>2</sup> Sergey I. Bozhevolnyi,<sup>2</sup> Eloisa Devaux,<sup>3</sup> and Thomas W. Ebbesen<sup>3</sup>

<sup>1</sup>Laboratory of Nanooptics and Femtosecond Electronics, Department of General Physics, Moscow Institute of Physics and Technology (State University), 9, Institutsky Lane, Dolgoprudny, 141700, Russia

<sup>2</sup>Institute of Technology and Innovation, University of Southern Denmark, Niels Bohrs Allé 1, DK-5230 Odense M, Denmark

<sup>3</sup>Laboratoire des Nanostructures, ISIS, Université de Strasbourg, CNRS (UMR7006), 8 allée Gaspard Monge, 67000 Strasbourg, France

\*Corresponding author: vz@iti.sdu.dk

Received March 16, 2011; accepted April 19, 2011;  
posted May 4, 2011 (Doc. ID 144219); published June 3, 2011

We report on experimental (by use of scanning near-field optical microscopy) and theoretical investigations of strongly confined ( $\sim\lambda/5$ ) channel plasmon polariton (CPP) modes propagating at telecom wavelengths (1425–1630 nm) along V-grooves cut in a gold film. The main CPP characteristics (mode index, width, and propagation length) are determined directly from the experimental near-field images and compared to theoretical results obtained using an analytic description of CPP modes supported by (infinitely deep) V-grooves and finite-element simulations implemented in COMSOL. © 2011 Optical Society of America

OCIS codes: 230.7380, 000.2700.

### 1. INTRODUCTION

Surface plasmon polaritons (SPPs) represent electromagnetic excitations that are bound to metal-dielectric interfaces [1]. Their fundamental properties have been the subject of extensive studies both theoretical and experimental. In recent years, the focus of investigation shifted noticeably toward exploring the possibilities for SPP control and manipulation with artificially created surface structures. The developments in plasmonic circuitry [2] suggest abundant possibilities for further advancement toward practical realization of exciting optical phenomena associated with metal nanostructures. Thus, the phenomenon of nanoscale field confinement by SPP manipulation has great potential to revolutionize many applications in nanophotonics, ranging from quantum optics [3] to imaging [4], near-field optics [5,6], and nanosensing [7].

Note that the physics of SPP guiding is fundamentally different from that of light guiding in dielectric waveguides (which obey the diffraction limit) and is intimately connected with the hybrid nature of SPP modes, in which electromagnetic fields in dielectrics are coupled to free electron oscillations in metals [1]. A variety of SPP guiding geometries have already been suggested to achieve high SPP concentration on length scales smaller than the diffraction limit of light (in the surrounding dielectric) [2]. The appropriate SPP modes are supported, for example, by linear chains of metal nanoparticles [8], narrow dielectric ridges deposited on metal films known as dielectric-loaded SPP waveguides (DLSPWs) [9], narrow gaps between metal surfaces (gap SPPs) [10], and by corresponding cylindrical, i.e., rod and coaxial, structures [11,12]. Since, for all of these SPP systems (except DLSPWs), the downscaling of cross section is not limited by the light wavelength, they represent a promising alternative to dielec-

tric optical waveguides. However, the simultaneous realization of strong confinement and a propagation loss sufficiently low for practical applications has long been out of reach.

Channel SPP modes—channel plasmon polaritons (CPPs)—are electromagnetic waves that are bound to and propagate along the bottom of V-shaped grooves milled in a metal film [13]. They are expected to exhibit useful subwavelength confinement, relatively low propagation loss [14], single-mode operation [15], and efficient transmission around sharp bends [16]. Recent experiments showed that CPPs at telecom wavelengths propagate over tens of micrometers along grooves in gold [17] and exhibit strong subwavelength confinement along with low bend losses in large-angle S-bends and Y-splitters [18], thereby enabling the realization of ultracompact plasmonic components such as Mach-Zehnder interferometers, waveguide-ring (WR) resonators [19], add-drop multiplexers, and compact Bragg grating filters [20] as well as nanofocusing components [21]. Thus, there is substantial interest in the fundamental properties of CPP propagation in metal V-grooves, which are determined by the dispersion properties of the CPP mode. Knowledge of CPP modal shape and dispersion properties is essential to set up an efficient end-fire excitation of the waveguide, and also to estimate efficient coupling between adjacent waveguides. In contrast to the dispersion relation for a SPP at a planar metal/dielectric interface, which is well investigated theoretically and experimentally (as well as for different planar waveguide configurations) [1,22,23], the dispersion of CPP modes and their field profiles in V-grooves has to date only been investigated theoretically [13,17,24–28].

In this paper, we report on experimental (by use of scanning near-field optical microscopy) and theoretical

investigations of the dispersion and the mode structure of strongly confined CPP modes propagating at telecommunication wavelengths along V-grooves cut in a gold film.

## 2. EXPERIMENTAL ARRANGEMENT

The sample, containing several straight  $150\ \mu\text{m}$  long V-shaped grooves with the angle  $\theta$  close to  $\sim 17^\circ$  and depth  $d$  of  $\sim 1.7\ \mu\text{m}$ , was fabricated using a focused ion-beam (FIB) milling technique in a  $2\text{-}\mu\text{m}$ -thick gold layer deposited on a substrate of fused silica covered with an  $80\text{-nm}$ -thick indium-tin-oxide layer [Fig. 1(a)]. For these groove parameters, the CPP guiding is expected to be single-mode [17]. Special care was taken to fabricate V-grooves with smooth walls and prevent contamination of the completed structures by dust particles.

The experimental setup is rather similar to that used in our previous experiments [17–21] and consists of a collection scanning near-field optical microscope (SNOM) with an uncoated sharp fiber tip used as a probe and an arrangement for launching tunable ( $1430\text{--}1620\ \text{nm}$ ) TE/TM-polarized radiation into a metal groove by positioning a tapered-lensed polarization-maintaining single-mode fiber [Fig. 1(b)]. Note that, since the main component of the SPP electric field is oriented perpendicularly to the metal surface [1], the CPP electric field tends to be oriented perpendicularly to the groove walls and thereby, for small groove angles, parallel to the sample surface plane. The adjustment of the in-coupling fiber with respect to the illuminated V-groove channel was accomplished during monitoring of the SPP propagation along the sample surface with the help of a far-field microscopic arrangement. The track of the propagating radiation (distinguishable for all structures and wavelengths) featured, apart from a gradual decay in visibility with the propagation distance, a rather bright spot at its termination [Fig. 1(c)]. These far-field obser-

vations also confirmed the expected polarization properties of the guided radiation [17] and demonstrated its (relatively) low dissipation. Following these experiments (that also include adjusting the in-coupling fiber position to maximize the coupling efficiency), we moved the entire fiber-sample arrangement under the SNOM head and mapped the intensity distribution near the surface of the groove with an uncoated sharp fiber tip of the SNOM. The near-field optical probe used in the experiment was produced from a single-mode silica fiber by  $\sim 120$  min etching of a cleaved fiber in 40% hydrofluoric acid with a protective layer of olive oil. The resulting fiber tip has a cone angle of  $\sim 30^\circ$  and curvature radius of less than  $100\ \text{nm}$  [Fig. 1(d)].

The tip was scanned along the sample surface at a constant distance of a few nanometers maintained by shear-force feedback. It should be noted that this distance could not be maintained in the middle of the groove (given the groove dimensions and the tip size), a circumstance that might influence the characterization of CPP mode cross section. Near-field radiation scattered by the tip was partially collected by the fiber itself and propagated in the form of the fiber modes toward the other end of the fiber, where it was detected by a femtowatt InGaAs photoreceiver.

## 3. EXPERIMENTAL RESULTS

The fabricated plasmonic structures were excited at different wavelengths ranging from  $1425$  to  $1630\ \text{nm}$  with TE-polarized light and imaged with SNOM. Topographical and near-field optical images of efficient CPP guiding by fabricated V-grooves were recorded at the distance of  $\sim 100\ \mu\text{m}$  from the in-coupling groove edge (to decrease the influence of the stray light, i.e., the light that was not coupled into the CPP mode) and in the entire range of laser tunability.

The experimental results (typical topographical and near-field optical images of CPP propagation at different wavelengths) can be seen in Fig. 2, where the SNOM images are oriented in such a way that the CPPs propagate from left to right (in the horizontal direction). SNOM measurements were carried out by scanning areas of roughly  $36.8\ \mu\text{m} \times 3.5\ \mu\text{m}$  [Figs. 2(a)–2(c)] and  $55\ \mu\text{m} \times 3.5\ \mu\text{m}$  [Figs. 2(d)–2(h)] along the waveguide. The fast scan direction was orthogonal to the V-groove. Appearance of the optical images is similar to those obtained with photonic crystal waveguides [29], featuring efficient mode confinement (in the lateral cross section) at the groove and clearly pronounced decay (along the propagation direction) of the CPP intensity. The aforementioned decay is found to be wavelength dependent, directly demonstrating (Fig. 2) the observed increase in CPP propagation length along with the corresponding increase in wavelength. The averaged cross sections taken along the propagation direction for optical ( $\lambda = 1630\ \text{nm}$ ) and corresponding topographical images are shown in Fig. 2(i). One can see that the cross section taken along the optical image demonstrates clearly pronounced (and rather unperiodic) intensity variations along the propagation direction. The latter is usually accounted for by the interference between the CPP mode's incident and scattered (by the groove imperfections and/or stray light [17]) field components. However, the preliminary analysis of these cross sections together with spatial spectra taken for different wavelengths has shown that the situation is quite complicated, because the cross sections/spectra exhibit

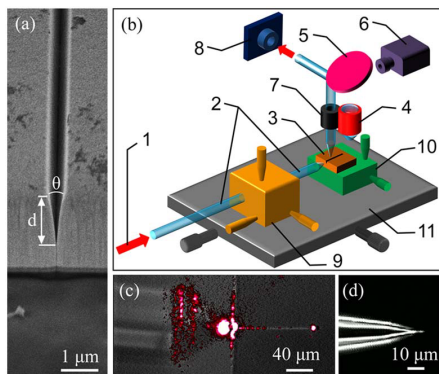


Fig. 1. (Color online) Experimental arrangement. (a) SEM image of V-groove entrance showing typical groove profile ( $d$  and  $\theta$  are groove depth and angle, respectively). (b) Schematic layout of the experimental setup. (1) TE-polarized radiation (electric field is parallel to sample surface plane) from tunable laser ( $1425\text{--}1630\ \text{nm}$ ); (2) in-coupling tapered-lensed polarization-maintaining single-mode fiber; (3) sample: gold film containing several straight V-grooves; (4) microscope objective of  $20\times$  magnification; (5) mirror; (6) IR camera; (7) SNOM operated in collection mode; (8) InGaAs photoreceiver; (9) three-dimensional  $X, Y, Z$  stage; (10),(11) two-dimensional  $X, Y$  stages. (c) Microscope image of a coupling arrangement superimposed with far-field image taken at excitation wavelength  $\lambda \approx 1600\ \text{nm}$  with IR camera, showing the track of CPP propagation and a bright spot at the V-groove termination. (d) Microscope image of near-field optical probe used in the experiment.

several features that are independent of the light wavelength and therefore should be related (in our opinion) to the roughness of groove walls and/or the scanning mechanism of the SNOM (including scanning speed, stability of the SNOM feedback, shape of the SNOM tip, etc.). To test this idea, the optical cross sections (taken at different wavelengths) were directly compared to cross sections taken (along the same direction) for the corresponding topographical images. The results obtained [Fig. 2(i)] revealed a good agreement between topographical and optical profiles (where the minima in the optical signal clearly correspond to the maxima in topography). Note that due to its evanescent nature, the CPP signal measured in the middle of a groove is directly related to the ability of the SNOM fiber tip to penetrate the channel (with the depth of penetration being kept as constant as possible). The cross sections of the topographical images (taken along and across the propagation direction) showed that the penetration depth varied significantly (both in time and space), with the SNOM tip actually being below the sample surface by  $\sim 200$ – $600$  nm, depending on the tip shape, stability of the scanning process, and/or the quality of the fabricated V-groove. Thus the disappearance of the CPP signal in certain areas of the groove along the propagation direction [clearly seen in some images, e.g., Figs. 2(e)–2(h)] has to be directly attributed to varying penetration depth of the SNOM fiber tip inside the V-groove. Note also that the recorded images are characterized by a high contrast ratio (the ratio of useful CPP signal in the groove to the background signal), i.e.,

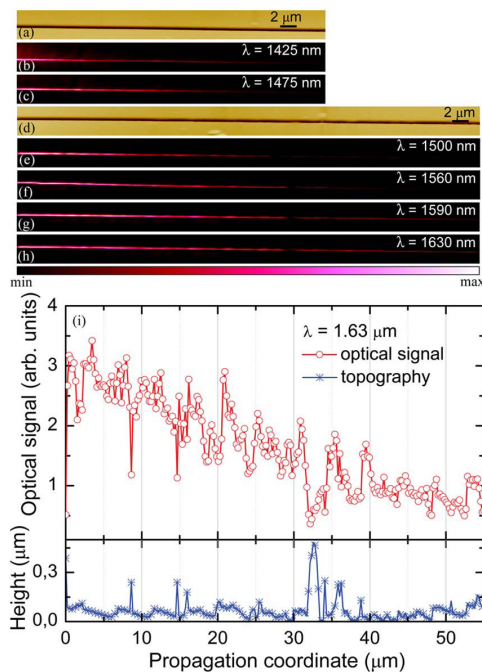


Fig. 2. (Color online) Experimental results. Pseudocolor (a), (d) topographical, and (b)–(c), (e)–(h) near-field optical images of different sizes; (a–c)  $36.8 \mu\text{m} \times 3.5 \mu\text{m}$ , (d–h)  $55 \mu\text{m} \times 3.5 \mu\text{m}$ . SNOM images recorded at different wavelengths with shear-force feedback, (b) 1425 nm, (c) 1475 nm, (e) 1500 nm, (f) 1560 nm, (g) 1590 nm, (h) 1630 nm. (i) Cross sections of the topographical (asterisks) and near-field optical (open circles) images of (d), (h) taken (along 1 line) along propagation direction.

CPP signal drops rapidly outside the groove, indicating the presence of a negligibly weak homogeneous background at the level of  $\sim 3\%$  compared to the maximum signal (inside the groove). Despite the aforementioned signal variations, we could use the recorded SNOM images to characterize the structure of the CPP mode and its propagation length. It turned out that in the wavelength range of 1425–1630 nm, the CPP propagation length (determined from the corresponding SNOM images) varied significantly, depending on both the coupling arrangement and wavelength used. To treat SNOM images properly, the following method has been used [Fig. 3(a)]: averaged optical signal profiles (taken along the propagation direction) have been directly extrapolated by the corresponding exponential dependences fitted by the least-squares method (where the CPP propagation length has been obtained from corresponding exponent coefficients). The result (that shows the CPP propagation length as a function of light wavelength) is presented in Fig. 3(b), where the

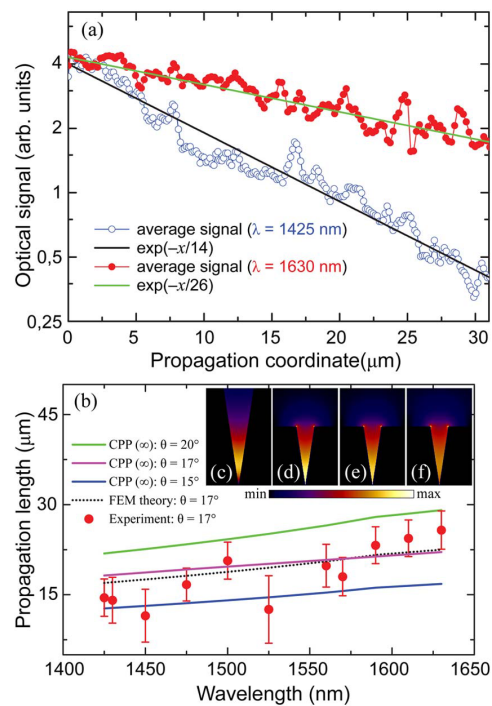


Fig. 3. (Color online) CPP propagation length estimation. (a) Cross sections of the near-field optical images in Figs. 2(b) and 2(h) (filled and open circles, respectively) averaged along 5 lines along the propagation direction; the exponential dependences fitted by the least-squares method to the signal dependence along the propagation direction are included. (b) CPP dispersion: the CPP propagation length as a function of light wavelength; filled circles represent the experimental data, with calculated theoretical curves in different colors. Error bars are estimated from the CPP propagation length maximum variations with the averaging windows at different positions along the propagation direction. Insets (time-averaged electric field distributions) represent the modal structure of the fundamental CPP modes at different wavelengths: (c) CPP ( $\infty$ ) mode for an infinitely deep groove at 1425 nm (computed with EI method); the CPP mode for increasing wavelength of (d) 1425, (e) 1480, and (f) 1630 nm (computed with FEM method for a truncated groove of depth  $1.7 \mu\text{m}$ ). Inset size is  $2 \mu\text{m} \times 3 \mu\text{m}$ .

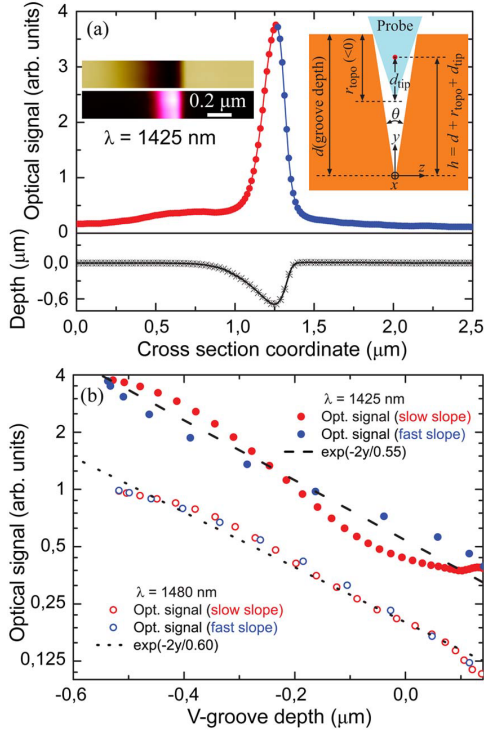


Fig. 4. (Color online) (a) Cross sections of the topographical (asterisks) and corresponding high-resolution near-field optical (filled circles) images (in left-hand insets) averaged along 10 lines perpendicular to the propagation direction. Schematic of the V-groove/SNOM probe configuration under consideration is shown in right-hand inset. (b) Optical signal recorded inside the groove, presented as a function of groove depth, along with the exponential fitting curve.

experimental values (determined through the aforementioned procedure) are shown by the filled circles.

Figure 3(b) also contains results that were calculated theoretically with two different electromagnetic techniques: the first, effective index (EI) approximation [17] in combination with analytic description [28] of CPP modes supported by infinitely deep V-grooves of different angles [shown by solid curves; for simplicity, these modes are labeled as CPP ( $\infty$ )]; and second, the finite-element method (FEM) as implemented in the commercial software COMSOL (dotted curve), using tabular gold dielectric constants [30]. Overall, it is seen that the experimental results are in rather good agreement (within experimental error) with our calculations, demonstrating a clearly pronounced general trend: the increase in CPP propagation length with the increase in wavelength. Note that the two theoretical approaches provided similar results, as expected for strongly confined (and thereby, far from the cutoff) CPP modes [28]. The same methods have also been used to investigate the structure of the fundamental CPP mode [see insets and legend of Figs. 3(c)–3(f)]. These results show

that as the wavelength increased (up to 1630 nm), the field is pushed out of the groove. The latter would facilitate its observation both with a far-field microscope (such a mode is easier to scatter by surface features) and the SNOM (the detection efficiency of a fiber probe increases for lower spatial frequencies [31]). One would expect that (keeping the same trend for even longer wavelengths) there should be a certain cutoff threshold ( $\lambda_{\text{cut}} > 1630$  nm) after which the CPP mode can no longer be confined within the groove, and is radiated in the form of SPPs along the contiguous horizontal metal surfaces. It is also observed that as the wavelength increases (i.e., approaching to cutoff), the CPP modes became hybridized with the modes running on the edges at both sides of the groove (e.g., calculations show rather strong hybridization of the CPP mode at  $\lambda = 1630$  nm even though it is still mainly confined within the groove walls).

Note that, in our opinion, the roughness and imperfections of V-groove walls (as well as other groove defects) contributed significantly to the detected CPP propagation loss (at least for shorter wavelengths in the range 1425–1525 nm). The discrepancy between theory and experiment can also be ascribed to small differences in the groove geometry, both in the groove shape (e.g., angle, depth, wall flatness) and/or different dielectric permittivities of gold (in our calculations, the Palik and Ghosh [30] data sets were used). For example, it was recently verified [24,27] that even slightly less negative dielectric permittivity of gold or/and smaller groove angle noticeably influences the properties of a CPP mode (including propagation length and cutoff wavelength). One can further suggest that the accuracy of the experimental results can be further improved by increasing the scanning area along the propagation direction of the groove (which should also be combined with a corresponding increase in the number of independent experiments). The latter task is not trivial, considering that the near-field optical microscopy (used in this experiment) is a point-by-point scanning technique (i.e., it is a time-consuming procedure to produce even one SNOM image with a high optical resolution). Despite these difficulties, the high-resolution SNOM images were recorded at different wavelengths (1425 and 1480 nm) and used to investigate the CPP mode characteristics. Figure 4(a) shows typical cross sections (averaged along 10 lines perpendicular to the propagation direction) of high-resolution topographical and corresponding near-field optical images (recorded at  $\lambda = 1425$  nm). From the cross sections of the SNOM images, one can see a clearly pronounced asymmetry of topographical and optical profiles (e.g., it is clearly pronounced as a difference in the slope of the groove walls). The latter is not a real topographical/optical artifact (e.g., the actual groove symmetry is revealed by the SEM images in Fig. 1) and should be attributed to a convolution (asymmetry) of the SNOM tip. Generally speaking, every data point in a SNOM image represents a spatial convolution (in the general sense, not in the sense of Fourier analysis) of the shape of the SNOM tip and the shape of the feature imaged (e.g., the V-groove, in

Table 1. Experimental and Numerically Calculated CPP Mode Characteristics

$\lambda$	$d_{\text{pen}}(\text{exp})$	$N_{\text{eff}}(\text{exp})$	$w_{\text{FWHM}}(\text{exp})$	$d_{\text{cut}}(\infty)/d_{\text{cut}}(\text{FEM})$	$N_{\text{eff}}(\infty)/N_{\text{eff}}(\text{FEM})$	$w_m(\infty)/w_m(\text{FEM})$
1425 nm	550 nm	1.08	170 nm	650 nm/750 nm	1.064/1.045	288 nm/250 nm
1480 nm	600 nm	1.07	190 nm	679 nm/825 nm	1.059/1.040	310 nm/273 nm

our case). As long as the tip is significantly sharper than the groove the true edge profile of the groove is represented. However, when the feature is sharper than the SNOM tip, the image will be dominated by the tip's shape.

To show experimentally that the power for the CPP mode is indeed efficiently concentrated within the V-groove, one needs to estimate the effective index of the CPP mode. We begin our considerations with the V-groove geometry [see the right-hand inset in Fig. 4(a)] assuming that the groove angle is sufficiently small ( $\theta \sim 17^\circ$  as in our experiment). Note that in this case, the SNOM probe can only partially penetrate the groove by a certain depth  $r_{\text{topo}}$  (which can be evaluated from topographical cross sections of the groove). It is reasonable to assume that the optical signal (collected by the SNOM tip), being proportional to the field intensity (at an effective detection point inside a fiber probe [31]), decreases exponentially with the probe-surface distance [21] (i.e., we are measuring the exponential tail of the CPP field concentrated deep into the groove where it cannot be reached with SNOM probe directly). The latter indicates that the effective index of the CPP mode can be obtained from the decay rate of the CPP field far from the groove bottom, assuming that the decay is exponential with respect to the distance  $h = d + r_{\text{topo}} + d_{\text{tip}}$  from the groove bottom ( $h > 1 \mu\text{m}$ , i.e., we are very close to the V-groove opening). Note that this procedure is essentially approximate because it does not take into account the dependence of the field intensity on the transverse coordinate. For the fiber probe used in our experiments, the effective detection point is found to be located at distance  $d_{\text{tip}} \sim 150 \text{ nm}$  away from the fiber tip [31]. The intensity of the field (picked up at the effective detection point of the SNOM tip) as a function of the distance from the groove bottom [Fig. 4(a)] can be presented as follows

$$I(y) \sim \exp(-\alpha h)^2 \approx I_0 \exp(-2r_{\text{topo}}/d_{\text{pen}}), \quad (1)$$

where  $\alpha = 1/d_{\text{pen}} = k_0(N_{\text{eff}}^2 - 1)^{0.5}$  represents the decay rate of the field,  $k_0 = 2\pi/\lambda$  is the wave number,  $\lambda$  is the radiation wavelength in vacuum,  $N_{\text{eff}} = \beta\lambda/(2\pi)$  is the CPP mode effective index, and  $\beta$  denotes the CPP mode propagation constant. Note that the CPP mode index  $N_{\text{eff}}$  determines the mode confinement, since the mode penetration depth in dielectric (air) above the sample surface is given by  $d_{\text{pen}} = (\lambda/2\pi) \cdot (N_{\text{eff}}^2 - 1)^{-0.5}$ , so that a larger effective index corresponds to a smaller penetration depth and thereby better confinement in depth (in width, the CPP mode is confined within the groove walls). To obtain the experimental value of the effective index by measuring the decay rate  $\alpha$ , the optical signal has been presented as a function of the groove depth  $r_{\text{topo}}$  penetrated by the SNOM tip. Thus, the assumption of exponential decay of the CPP field is verified experimentally: Figure 4(b) demonstrates that the intensity of the CPP signal recorded at  $\lambda = 1425$  (shown by the filled circles) and  $1480 \text{ nm}$  (shown by the open circles) indeed decays exponentially with the distance from the groove bottom as  $\sim \exp(-2y/0.55)$  for  $1425 \text{ nm}$  and  $\sim \exp(-2y/0.60)$  for  $1480 \text{ nm}$ . These exponential decays give the CPP mode penetration depth  $d_{\text{pen}}$  [Eq. (1)] of  $550 \text{ nm}$  (at  $\lambda = 1425 \text{ nm}$ ) and  $600 \text{ nm}$  (at  $\lambda = 1480 \text{ nm}$ ), and the corresponding experimental  $N_{\text{eff}}(\text{exp})$  values are close to 1.08 and 1.07.

This experimental evolution in the CPP field distribution with the groove depth is compared with the fundamental CPP mode profiles calculated with EI (for the infinitely deep groove) and finite-element (for the truncated groove) methods at  $1425$  and  $1480 \text{ nm}$ . Here, one should keep in mind that EI method (EIM) usage forces the V-groove CPP fields to approach zero at the groove bottom similarly to the case of CPPs propagating in rectangular grooves (tranches) and for the same reason [27], whereas the CPP field is expected to reach its maximum at the V-groove bottom [13–15]. Influence of the EIM approximation is also reflected in the differences between the effective mode indexes calculated with the FEM, e.g.,  $N_{\text{eff}}(\text{FEM}) \cong 1.045$ , and with EIM  $N_{\text{eff}}(\infty) \cong 1.064$  (both found to be smaller than  $N_{\text{eff}}(\text{exp})$  estimated experimentally at  $\lambda = 1425 \text{ nm}$ ). It should be also noted that the  $y$  coordinate appearing in Eq. (1) acts as a parameter that determines the V-groove width:  $w(y) = 2y \tan(\theta/2)$ . To get further theoretical insight into the CPP mode structure, we evaluated the cutoff depth  $d_{\text{cut}}$  of the V-groove. The latter is the depth ( $y$  coordinate) corresponding to the position of the average maximum of the CPP field (i.e., we were looking for  $\max[w(y)I_{\text{CPP}}(y)]$ ); and the groove width at this cutoff depth was considered to be the width of the CPP mode:  $w_m = 2d_{\text{cut}} \tan(\theta/2) \approx \theta d_{\text{cut}}$ . Thus, for the considered V-groove configuration, the cutoff depths and CPP mode widths calculated (at  $\lambda = 1425 \text{ nm}$ ) with EIM (for infinitely deep groove),  $d_{\text{cut}}(\infty) = 650 \text{ nm}$  and  $w_m(\infty) = 288 \text{ nm}$  are found to be quite similar to those obtained with FEM (for finite-depth groove),  $d_{\text{cut}}(\text{FEM}) = 750 \text{ nm}$  and  $w_m(\text{FEM}) = 250 \text{ nm}$ . In general, it is seen that there is a certain discrepancy between CPP mode characteristics calculated with EIM and FEM. We relate this fact to the circumstance that the correspondence between the EIM (approximate) simulations and accurate numerical modeling (e.g., when using the FEM) is generally worse for channel waveguides [24,26]. Finally, the full width at half-maximum (FWHM) was measured for the experimental mode profiles. The FWHM appeared to be much smaller than the widths calculated numerically (by both EIM and FEM). It can be explained by a strong (nearly exponential) dependence of the CPP field magnitude on the depth coordinate. The deeper the SNOM probe penetrates into the groove, the larger the field magnitude is, so the whole optical profile of the mode becomes narrower. Nevertheless, the measured FWHMs for  $1425$  and  $1480 \text{ nm}$  reflect the same trend as for the numerical calculations: the larger the wavelength, the smaller the width.

Summarizing, the CPP mode characteristics determined from high-resolution SNOM images (recorded at  $1425$  and  $1480 \text{ nm}$ ) through the experimental procedures described here are summarized in Table 1 together with the results of corresponding calculations performed (for the wavelengths and groove parameters used in experiments) by using EIM and FEM.

Note that the calculated effective indexes of the fundamental CPP mode are somewhat smaller than the CPP mode indexes determined from the experimental SNOM images. This discrepancy can be attributed to the aforementioned (small) differences in V-groove shape. One should also keep in mind that the SNOM experiments were conducted at ambient conditions; thus water condensation could not be excluded (a very thin water layer can significantly increase the CPP mode index [24]).



#### 4. CONCLUSION

We have studied the dispersion properties of strongly confined CPP modes propagating at telecom wavelengths (1425–1630 nm) along V-grooves cut in a gold film, inferring the main CPP characteristics (mode index, width, and propagation length) from the experimentally obtained SNOM images and comparing them with simulation results obtained by making use of the analytic description of CPP modes supported by infinitely deep V-grooves [28] and FEM implemented in the commercial software COMSOL. The comparison conducted for CPP propagation length, which was straightforwardly evaluated from the experimental SNOM images, indicated that the difference between the two theoretical approaches is smaller than the uncertainty related to the actual groove profile. Note that for strongly confined (and thereby far from the cutoff) CPP modes, these approaches are expected to provide similar results [28]. It also revealed inherent problems with the experimental SNOM characterization of CPP propagation length related to instabilities in maintaining the same (fiber) tip-surface distance. These instabilities seem to be very difficult to circumvent for sufficiently narrow and deep V-grooves, while those are in fact required to strongly confine CPP modes [24,26–28].

The effective indexes of CPP modes were determined from cross sections of the experimentally obtained topographical and near-field optical images by using exponential fits to the optical signal dependences on the distance between the fiber tip and the groove bottom, a procedure that provides direct access to the mode index while being inherently approximate (as noted in Section 3). Taking this into account, the agreement between the mode indexes determined from the SNOM images and those obtained from the simulations can be considered satisfactory. At the same time, it has to be borne in mind that the former tend to be consistently larger than the latter. Finally, we also found that the evaluation of CPP mode confinement directly from SNOM images can be rather misleading, resulting in underestimation of the mode width (especially for strongly confined CPP modes) because of strong correlation between topological and near-field optical profiles.

Overall, we have fabricated gold V-grooves supporting strongly confined ( $\sim\lambda/5$ ) CPP modes and determined their main characteristics at telecom wavelengths by using the SNOM images. The results obtained are of great importance for further developments in CPP-based plasmonic circuitry [2], where the degree of mode lateral confinement plays a crucial role imposing the upper limit on the density of plasmonic components [27]. In comparison with our first experiments [17–20], the presented CPP waveguides demonstrate an improvement by, at least, 3 times in the lateral mode confinement. Another important conclusion is that the main CPP characteristics can be determined *directly* from the SNOM images, albeit with different levels of accuracy. In this context, our consideration of various issues related to the CPP characterization by using the SNOM provides a firm background for future experimental work, alleviating the need for extensive and time-consuming full-field simulations.

We believe that the results obtained in this work constitute an important step toward developing real-life applications of CPP-based plasmonic circuitry in the fields of optical interconnects and sensing. In this context, a significant challenge

yet to be addressed is the realization of efficient in- and out-coupling of radiation, preferably without need for the end-fire coupling with optical fibers that, in fact, can be realized only from one side [17–21]. Strongly confined CPP modes seem especially attractive for sensing applications, in which V-grooves would also be used for microfluidics, since these modes exhibit substantial field enhancements at V-groove bottoms (unlike weakly confined CPP modes [24]). Filling V-grooves with fluids or other materials (e.g., polymers) efficiently represents, however, another formidable challenge that requires further extensive investigations.

#### ACKNOWLEDGMENTS

The authors gratefully acknowledge financial support from the Danish Council for Independent Research (FTP-project no. 09-072949 ANAP) and the European Research Council (ERC) (grant 227577).

#### REFERENCES

1. H. Raether, *Surface Plasmons* (Springer, 1988).
2. T. W. Ebbesen, C. Genet, and S. I. Bozhevolnyi, "Surface plasmon circuitry," *Phys. Today* **61**, 44–50 (2008).
3. D. E. Chang, A. S. Sørensen, E. A. Demler, and M. D. Lukin, "A single-photon transistor using nanoscale surface plasmons," *Nature Phys.* **3**, 807–812 (2007).
4. N. Fang, H. Lee, C. Sun, and X. Zhang, "Sub-diffraction-limited optical imaging with a silver superlens," *Science* **308**, 534–547 (2005).
5. N. A. Janunts, K. S. Baghdasaryan, Kh. V. Nerkararyan, and B. Hech, "Excitation and superfocusing of surface plasmon polaritons on a silver-coated optical fiber tip," *Opt. Commun.* **253**, 118–124 (2005).
6. Y. Wang, W. Srituravanich, C. Sun, and X. Zhang, "Plasmonic near-field scanning probe with high transmission," *Nano Lett.* **8**, 3041–3045 (2008).
7. M. Ringler, A. Schwemer, M. Wunderlich, A. Nichtl, K. Kurzinger, T. A. Klar, and J. Feldmann, "Shaping emission spectra of fluorescent molecules with single plasmonic nanoresonators," *Phys. Rev. Lett.* **100**, 203002 (2008).
8. M. Quinten, A. Leitner, J. R. Krenn, and F. R. Aussenegg, "Electromagnetic energy transport via linear chains of silver nanoparticles," *Opt. Lett.* **23**, 1331–1333 (1998).
9. T. Holmgaard, S. I. Bozhevolnyi, L. Markey, A. Derex, A. V. Krasavin, P. Bolger, and A. V. Zayats, "Efficient excitation of dielectric-loaded surface plasmon-polariton waveguide modes at telecommunication wavelengths," *Phys. Rev. B* **78**, 165431 (2008).
10. H. Choi, D. F. P. Pile, S. Nam, G. Bartal, and X. Zhang, "Compressing surface plasmons for nano-scale optical focusing," *Opt. Express* **17**, 7519–7524 (2009).
11. C. A. Pfeiffer, E. N. Economou, and K. L. Ngai, "Surface polaritons in a circularly cylindrical interface: surface plasmons," *Phys. Rev. B* **10**, 3038–3051 (1974).
12. J. Takahara, S. Yamagishi, H. Taki, A. Morimoto, and T. Kobayashi, "Guiding of a one-dimensional optical beam with nanometer diameter," *Opt. Lett.* **22**, 475–477 (1997).
13. I. V. Novikov and A. A. Maradudin, "Channel polaritons," *Phys. Rev. B* **66**, 035403 (2002).
14. D. F. P. Pile and D. K. Gramotnev, "Channel plasmon-polariton in a triangular groove on a metal surface," *Opt. Lett.* **29**, 1069–1071 (2004).
15. D. K. Gramotnev and D. F. P. Pile, "Single-mode subwavelength waveguide with channel plasmon-polaritons in triangular grooves on a metal surface," *Appl. Phys. Lett.* **85**, 6323–6325 (2004).
16. D. F. P. Pile and D. K. Gramotnev, "Plasmonic subwavelength waveguides: next to zero losses at sharp bends," *Opt. Lett.* **30**, 1186–1188 (2005).

17. S. I. Bozhevolnyi, V. S. Volkov, E. Devaux, and T. W. Ebbesen, "Channel plasmon-polariton guiding by subwavelength metal grooves," *Phys. Rev. Lett.* **95**, 046802 (2005).
18. V. S. Volkov, S. I. Bozhevolnyi, E. Devaux, and T. W. Ebbesen, "Bend loss for channel plasmon polaritons," *Appl. Phys. Lett.* **89**, 143108 (2006).
19. S. I. Bozhevolnyi, V. S. Volkov, E. Devaux, J.-Y. Laluet, and T. W. Ebbesen, "Channel plasmon subwavelength waveguide components including interferometers and ring resonators," *Nature* **440**, 508–511 (2006).
20. V. S. Volkov, S. I. Bozhevolnyi, E. Devaux, J.-Y. Laluet, and T. W. Ebbesen, "Wavelength selective nanophotonic components utilizing channel plasmon polaritons," *Nano Lett.* **7**, 880–884 (2007).
21. V. S. Volkov, S. I. Bozhevolnyi, S. G. Rodrigo, L. Martín-Moreno, F. J. García-Vidal, E. Devaux, and T. W. Ebbesen, "Nanofocusing with channel plasmon polaritons," *Nano Lett.* **9**, 1278–1282 (2009).
22. G. Schider, J. R. Kren, A. Hohenau, H. Ditlbacher, A. Leitner, F. R. Aussenegg, W. L. Schaich, I. Puscasu, B. Monacelli, and G. Boreman, "Plasmon dispersion relation of Au and Ag nanowires," *Phys. Rev. B* **68**, 155427 (2003).
23. J. A. Dionne, L. A. Sweatlock, H. A. Atwater, and A. Polman, "Planar metal plasmon waveguides: frequency-dependent dispersion, propagation, localization and loss beyond the free electron model," *Phys. Rev. B* **72**, 075405 (2005).
24. E. Moreno, F. J. Garcia-Vidal, S. G. Rodrigo, L. Martín-Moreno, and S. I. Bozhevolnyi, "Channel plasmon-polaritons: modal shape, dispersion, and losses," *Opt. Lett.* **31**, 3447–3449 (2006).
25. I. Lee, J. Jung, J. Park, H. Kim, and B. Lee, "Dispersion characteristics of channel plasmon polariton waveguides with step-trench-type grooves," *Opt. Express* **15**, 16596–16603 (2007).
26. S. I. Bozhevolnyi and J. Jung, "Scaling for gap plasmon based waveguides," *Opt. Express* **16**, 2676–2684 (2008).
27. S. I. Bozhevolnyi, "Effective-index modeling of channel plasmon polaritons," *Opt. Express* **14**, 9467–9476 (2006).
28. S. I. Bozhevolnyi and K. V. Nerkararyan, "Analytic description of channel plasmon polaritons," *Opt. Lett.* **34**, 2039–2041 (2009).
29. V. S. Volkov, S. I. Bozhevolnyi, L. H. Frandsen, and M. Kristensen, "Direct observation of surface mode excitation and slow light coupling in photonic crystal waveguides," *Nano Lett.* **7**, 2341–2345 (2007).
30. E. Palik and G. Ghosh, *Handbook of Optical Constants of Solids II* (Academic, 1991).
31. I. P. Radko, I. S. Bozhevolnyi, and N. Gregersen, "Transfer function and near-field detection of evanescent waves," *Appl. Opt.* **45**, 4054–4061 (2006).

# Appendix A.2

CPP directional coupling

---

# Directional coupling in channel plasmon-polariton waveguides

Vladimir A. Zenin,<sup>1,2,\*</sup> Valentyn S. Volkov,<sup>1</sup> Zhanghua Han,<sup>1</sup> Sergey I. Bozhevolnyi,<sup>1</sup>  
Eloïse Devaux,<sup>3</sup> and Thomas W. Ebbesen<sup>3</sup>

<sup>1</sup>*Institute of Technology and Innovation, University of Southern Denmark, Niels Bohrs Allé 1, DK-5230 Odense M, Denmark*

<sup>2</sup>*Laboratory of Nanooptics and Femtosecond Electronics, Moscow Institute of Physics and Technology (State University), Institutsky Lane 9, 141700 Dolgoprudny, Russia*

<sup>3</sup>*Laboratoire des Nanostructures, ISIS, Université de Strasbourg, CNRS (UMR7006), 8 allée Gaspard Monge, 67000 Strasbourg, France*

\*zenin@iti.sdu.dk

**Abstract:** We investigate directional couplers (DCs) formed by channel plasmon-polariton (CPP) waveguides (CPPWs). DCs comprising 5- $\mu\text{m}$ -offset S-bends and 40- $\mu\text{m}$ -long parallel CPPWs with different separations (0.08, 0.25, 0.5 and 2  $\mu\text{m}$ ) between V-groove channels are fabricated by using a focused ion-beam (FIB) technique in a 2- $\mu\text{m}$ -thick gold film and characterized at telecom wavelengths (1425-1630 nm) with near-field optical microscopy. Experimental results reveal strong coupling, resulting in approximately equal power splitting between DC-CPPWs, for small CPPW separations (0.08 and 0.25  $\mu\text{m}$ ). The coupling gradually deteriorates with the increase of separation between V-grooves and practically vanishes for the separation of 2  $\mu\text{m}$ . The DC-CPPW characteristics observed are found in good agreement with finite-element method (implemented in COMSOL) simulations.

©2012 Optical Society of America

OCIS codes: (230.7380) Waveguides, channeled; (240.6680) Surface plasmons.

## References and links

1. V. M. Agranovich and D. L. Mills, eds., *Surface Polaritons* (North-Holland, 1982).
2. H. Raether, *Surface Plasmons* (Springer-Verlag, 1988).
3. N. E. Glass, A. A. Maradudin, and V. Celli, "Theory of surface-polariton resonances and field enhancements in light scattering from gratings," *J. Opt. Soc. Am.* **73**(10), 1240–1248 (1983).
4. J. M. Pitarke, V. M. Silkin, E. V. Chulkov, and P. M. Echenique, "Theory of surface plasmons and surface-plasmon polaritons," *Rep. Prog. Phys.* **70**(1), 1–87 (2007).
5. S. I. Bozhevolnyi and F. Pudonin, "Two-dimensional micro-optics of surface plasmons," *Phys. Rev. Lett.* **78**(14), 2823–2826 (1997).
6. T. W. Ebbesen, H. J. Lezec, H. F. Ghaemi, T. Thio, and P. A. Wolff, "Extraordinary optical transmission through sub-wavelength hole arrays," *Nature* **391**(6668), 667–669 (1998).
7. J. K. Lim, K. Imura, T. Nagahara, S. K. Kim, and H. Okamoto, "Imaging and dispersion relations of surface plasmon modes in silver nanorods by near-field spectroscopy," *Chem. Phys. Lett.* **412**(1-3), 41–45 (2005).
8. T. W. Ebbesen, C. Genet, and S. I. Bozhevolnyi, "Surface-plasmon circuitry," *Phys. Today* **61**(5), 44–50 (2008).
9. D. K. Gramotnev and S. I. Bozhevolnyi, "Plasmonics beyond the diffraction limit," *Nat. Photonics* **4**(2), 83–91 (2010).
10. J. A. Conway, S. Sahni, and T. Szkopek, "Plasmonic interconnects versus conventional interconnects: a comparison of latency, crosstalk and energy costs," *Opt. Express* **15**(8), 4474–4484 (2007).
11. H. Ditlbacher, A. Hohenau, D. Wagner, U. Kreibig, M. Rogers, F. Hofer, F. R. Aussenegg, and J. R. Krenn, "Silver nanowires as surface plasmon resonators," *Phys. Rev. Lett.* **95**(25), 257403 (2005).
12. M. L. Brongersma, J. W. Hartman, and H. A. Atwater, "Electromagnetic energy transfer and switching in nanoparticle chain arrays below the diffraction limit," *Phys. Rev. B* **62**(24), 16356–16359 (2000).
13. S. A. Maier, M. L. Brongersma, P. G. Kik, and H. A. Atwater, "Observation of near-field coupling in metal nanoparticle chains using far-field polarization spectroscopy," *Phys. Rev. B* **65**(19), 193408 (2002).
14. J. R. Krenn and J. C. Weeber, "Surface plasmon polaritons in metal stripes and wires," *Philos. Trans. A Math. Phys. Eng. Sci.* **362**(1817), 739–756 (2004).

15. A. Boltasseva, T. Nikolajsen, K. Leosson, K. Kjaer, M. S. Larsen, and S. I. Bozhevolnyi, "Integrated optical components utilizing long-range surface plasmon polaritons," *J. Lightwave Technol.* **23**(1), 413–422 (2005).
16. J. Gosciniaik, V. S. Volkov, S. I. Bozhevolnyi, L. Markey, S. Massenet, and A. Dereux, "Fiber-coupled dielectric-loaded plasmonic waveguides," *Opt. Express* **18**(5), 5314–5319 (2010).
17. K. Tanaka, M. Tanaka, and T. Sugiyama, "Simulation of practical nanometric optical circuits based on surface plasmon polariton gap waveguides," *Opt. Express* **13**(1), 256–266 (2005).
18. I. V. Novikov and A. A. Maradudin, "Channel polaritons," *Phys. Rev. B* **66**(3), 035403 (2002).
19. S. I. Bozhevolnyi, V. S. Volkov, E. Devaux, and T. W. Ebbesen, "Channel plasmon-polariton guiding by subwavelength metal grooves," *Phys. Rev. Lett.* **95**(4), 046802 (2005).
20. V. S. Volkov, S. I. Bozhevolnyi, E. Devaux, and T. W. Ebbesen, "Bend loss for channel plasmon polaritons," *Appl. Phys. Lett.* **89**(14), 143108 (2006).
21. V. S. Volkov, S. I. Bozhevolnyi, S. G. Rodrigo, L. Martín-Moreno, F. J. García-Vidal, E. Devaux, and T. W. Ebbesen, "Nanofocusing with channel plasmon polaritons," *Nano Lett.* **9**(3), 1278–1282 (2009).
22. S. I. Bozhevolnyi, V. S. Volkov, E. Devaux, J.-Y. Laluet, and T. W. Ebbesen, "Channel plasmon subwavelength waveguide components including interferometers and ring resonators," *Nature* **440**(7083), 508–511 (2006).
23. V. S. Volkov, S. I. Bozhevolnyi, E. Devaux, J.-Y. Laluet, and T. W. Ebbesen, "Wavelength selective nanophotonic components utilizing channel plasmon polaritons," *Nano Lett.* **7**(4), 880–884 (2007).
24. V. A. Zenin, V. S. Volkov, Z. Han, S. I. Bozhevolnyi, E. Devaux, and T. W. Ebbesen, "Dispersion of strongly confined channel plasmon polariton modes," *J. Opt. Soc. Am. B* **28**(7), 1596–1602 (2011).
25. D. Arbel and M. Orenstein, "Plasmonic modes in W-shaped metal-coated silicon grooves," *Opt. Express* **16**(5), 3114–3119 (2008).
26. Y. Li and X. Zhang, "Directional couplers using V-groove plasma waveguides," in *IEEE Symposium on Photonics and Optoelectronics* (Institute of Electrical and Electronics Engineers, New York, 2009), 1–3.
27. R. F. Oulton, G. Bartal, D. F. P. Pile, and X. Zhang, "Confinement and propagation characteristics of subwavelength plasmonic modes," *New J. Phys.* **10**(10), 105018 (2008).
28. V. S. Volkov, S. I. Bozhevolnyi, E. Devaux, and T. W. Ebbesen, "Compact gradual bends for channel plasmon polaritons," *Opt. Express* **14**(10), 4494–4503 (2006).
29. E. Palik and G. Ghosh, *Handbook of Optical Constants of Solids II* (Academic Press, 1991).
30. E. Moreno, F. J. Garcia-Vidal, S. G. Rodrigo, L. Martin-Moreno, and S. I. Bozhevolnyi, "Channel plasmon-polaritons: modal shape, dispersion, and losses," *Opt. Lett.* **31**(23), 3447–3449 (2006).
31. S. I. Bozhevolnyi and J. Jung, "Scaling for gap plasmon based waveguides," *Opt. Express* **16**(4), 2676–2684 (2008).

## 1. Introduction

Surface plasmon polaritons (SPPs) are electromagnetic excitations (i.e., combined oscillations of the electromagnetic field and the surface charges of the metal) existing on a metal dielectric interface [1]. Their field distribution is evanescent in the direction perpendicular to the propagation direction, resulting in intense fields that decay exponentially into both (metal and dielectric) media that bound the interface [2]. Over the last decades, there has been a significant advance in SPPs investigations and a number of theoretical [2–4] and experimental [5–7] studies have been reported. Thus, it is expected that SPPs can be advantageously used for creating a new generation of nanophotonics devices and circuits [8, 9]. The main issue in this context is to strongly confine the SPP field in the cross-section (perpendicular to propagation direction), while keeping low propagation losses [10]. It has been shown that nanometer-sized silver nanowires can support strongly confined SPP modes propagating through only 10  $\mu\text{m}$  [11]. Similar properties were expected [12] and indeed found [13] for the electromagnetic excitations supported by chains of metal nanoparticles. Other configurations, including (among others) SPP propagation along metal stripes [14,15], narrow dielectric ridges deposited on metal films [16] and gap waveguides [17] (based on SPP propagation between two metal surfaces) have been suggested. It should be noted that, in general, the SPP confinement is achieved primarily by decreasing the SPP spatial extent into dielectric, thereby increasing the portion of SPP power being absorbed by metal, so that the choice of optimum guiding configuration is subject to trade-off with many intricate issues yet to be elucidated [10]. One of the most promising approaches for achieving strong lateral confinement of the SPP fields (simultaneously with relatively low propagation loss) is to utilize V-grooves milled in otherwise smooth metal films.

Channel SPP modes, or channel plasmon polaritons (CPPs), where the radiation is concentrated at the bottom of such V-shaped grooves, have been first predicted [18] and then

experimentally shown [19] to exhibit useful subwavelength guiding properties. Their unique features of strong SPP mode confinement make it possible to bend (and split) CPP waveguides (CPPWs) formed in the materials with extremely small curvature [20]. CPPs have already been found suitable for realization of many passive photonic devices [19–23], and may find important applications as basic building blocks in ultrahigh-speed all-optical signal processing circuits [8, 9]. Note that even though the dispersion properties of strongly confined CPP modes (propagating at telecom wavelengths) have been recently reported [24], inferring the main CPP characteristics (mode index, width and propagation length), the directional coupling in CPPWs that determines the integration potential of CPPW-based photonic circuits (with respect to the maximum allowed density of non-interacting CPPWs) has so far been paid little attention to [25, 26].

Here, we present the results of our investigations at telecom wavelengths (1425–1630 nm) of directional couplers (DCs) based on CPP modes guided by V-grooves cut in a gold film and separated by different distances. The main goal of our work was to characterize the crosstalk between adjacent CPPWs so as to accurately determine the minimum CPPW separation that can still be tolerated with respect to the incurred crosstalk. In principle, this separation is directly related to the CPP mode confinement [9, 19–24]. It should be borne in mind though, that the mode confinement can be characterized in different ways (especially for plasmonic waveguides) leading to different conclusions about the absolute and relative confinement strengths [27]. For example, one can introduce the average (lateral) width  $w$  that can be used to determine the largest bend angle  $\theta \sim \lambda/w$  allowed by the acceptable level of bend loss. However, such mode width cannot be applied to determine accurately the minimum separation between neighbor waveguide components since it does not take into account the coupling between modes in adjacent waveguide components. For such purpose the investigation of DCs should provide immediately the value of this minimum separation and, therefore, set the limit on the maximum density of waveguide components.

The remainder of this paper is organized as follows. In Section 2 the investigated sample and the experimental arrangement are described. Section 3 is devoted to the experimental results featuring the scanning near-field optical microscope (SNOM) images of CPP-based DCs and their interpretation. In Section 4 we use finite element method (FEM) implemented in COMSOL for numerical simulations of DCs. Finally, the paper is terminated with our conclusions offered in Section 5.

## 2. Sample description and experimental setup

The sample contained several DCs with channels made as V-shaped grooves, milled by a focused ion-beam (FIB) in a 2- $\mu\text{m}$ -thick gold layer, deposited on a substrate of fused silica covered with an 80-nm-thick indium-tin-oxide layer [Fig. 1(a)]. For each DC one V-groove (called main in our work) was longer and it started from the edge of the sample, while an adjacent second V-groove went parallel to the first one, starting at the distance of approximately 100  $\mu\text{m}$  from the edge of the sample. Two V-grooves were separated by a distance  $d$  (measured at the surface level on SEM images), varied for different DCs from 0.08 to 2  $\mu\text{m}$ , over the length of 40  $\mu\text{m}$ ; then they were pulled apart (by the use of the S-bend design that connects two parallel 5- $\mu\text{m}$ -offset waveguides over a distance of 5  $\mu\text{m}$ ) to increase the separation between the channels to about 10  $\mu\text{m}$  [Fig. 1(b)]. The intention with using S-bends (characterized by the smallest curvature radius  $\sim 2.25$   $\mu\text{m}$  [22]) after the coupling region and laterally displacing the output DC channels was to decrease the influence of radiation scattered in the coupling region on the signal detected in the output channels. Also it allowed measuring the output more accurately (since the coupling region was fixed, so the intensity distribution in two channels at the output could be measured over some distance, not at one point). Each V-groove had an angle  $\theta$  close to  $25^\circ$  and depth  $H$  of  $\sim 1.4$   $\mu\text{m}$  [Fig. 1(c)]. For these parameters only the first (fundamental) CPP mode can be guided in the groove [19].

The experimental setup was quite similar to those used in our previous experiments [19–24]. It consisted of a scanning near-field optical microscope (SNOM) with a sharp optical fiber tip used as a probe, in-coupling arrangement with a tapered-lensed fiber used to couple light to CPP by illuminating the open end of V-groove from the edge of the sample, and a positioning system consisting of several stages [Fig. 1(d)]. The radiation (wavelength 1425–1630 nm) was delivered from a tunable laser by the polarization-maintaining single-mode fiber (note that the CPP mode is excited efficiently for TE mode [19], when the electrical field is almost perpendicular to the groove's walls and parallel to the sample surface). The adjustment of the in-coupling fiber at the focal distance of approximately  $15\ \mu\text{m}$  [Fig. 1(e)] with respect to the illuminated V-groove channel was accomplished while monitoring the SPP propagation along the sample surface with the help of a far-field microscopy arrangement:  $20\times$  objective, mirror and IR-camera. The track of the propagating radiation (distinguishable for all DCs and wavelengths) featured a gradual decay in visibility along the propagation direction. These far-field observations have also confirmed the expected polarization properties of the guided radiation [19] and demonstrated its (relatively) low dissipation.

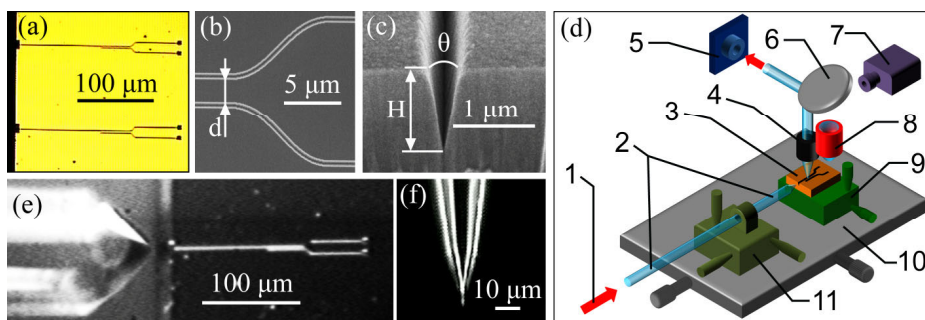


Fig. 1. (a) Microscope image of the sample containing several DCs. (b) SEM image showing the DC with two channels separated by distance  $d$  in the coupling region and by approx.  $10\ \mu\text{m}$  at the output after two S-bends. (c) SEM image of the cross-section of V-groove reveals groove parameters: angle  $\theta \sim 25^\circ$  and depth  $H \sim 1.4\ \mu\text{m}$ . (d) Experimental setup: (1) incoming TE-polarized radiation from tunable laser (free-space wavelength 1425–1630 nm); (2) polarization-maintained fiber with a tapered-lensed end used to couple light to CPP mode; (3) sample; (4) SNOM probe with its positioning system; (5) femtowatt InGaAs photoreceiver; (6) mirror; (7) IR camera; (8)  $20\times$  objective; (9,10) 2-dimensional X, Y stages; (11) 3-dimensional X, Y, Z stage. (e) In-coupling arrangement with the tapered-lensed fiber in front of the DC input. (f) Microscope image of the uncoated sharpened fiber tip used as a near-field optical probe.

Following these experiments (that include also adjusting the in-coupling fiber position to maximize the coupling efficiency) the whole fiber-sample arrangement was placed under the SNOM head to map the intensity distribution near the sample surface. Tapered fiber tip, used as a SNOM probe, was made from a single-mode silica fiber by  $\sim 2$  hours etching of a cleaved fiber in 40% hydrofluoric acid with a protective layer of olive oil. The resulting fiber tip had a cone angle of  $\sim 30^\circ$  and curvature radius of less than  $100\ \text{nm}$  [Fig. 1(f)]. In scanning process the tip was forced to keep the constant distance of a few nanometers from the sample surface by the shear-force feedback. However, inside the V-groove the maximum penetration depth was limited by the shape of the tip. The near-field radiation has been scattered and partially collected by the fiber tip itself, and afterwards guided (in the form of fiber modes) towards the other end of the fiber, where it has been detected by the femtowatt InGaAs photoreceiver (providing both topographical and near-field optical images, simultaneously).

### 3. Experimental results

#### 3.1 CPP coupling at different wavelengths

We conducted a series of experiments investigating CPP coupling for the DC with the separation distance between V-grooves  $d = 0.25\ \mu\text{m}$  at different wavelengths varied from

1425 nm to 1630 nm (Fig. 2). This DC had the smallest separation between V-grooves (excluding the one with the separation of 0.08  $\mu\text{m}$ , the reason for that will be discussed in Section 3.2), so it was expected to provide the best coupling between CPP modes. It was determined that for the 40- $\mu\text{m}$ -long coupling region the CPP intensity in the main groove evenly decreased, while the CPP intensity in the adjusted groove increased uniformly, reaching roughly the same level as of the first groove CPP intensity. It was difficult to obtain an image with a low background all over the whole coupling region due to short CPP propagation length, so in order to obtain the intensity distribution at the output more precisely, we performed the scanning of the DC by SNOM beyond this coupling region, where the grooves are separated by about 10  $\mu\text{m}$  and no coupling is expected for such large separation [Figs. 2(e)–2(h)]. These measurements confirmed the approximately equal power splitting between output CPPWs for all wavelengths, with some small variations that cannot be ascribed to any simple dependence on the wavelength. These variations could be caused by different contributions of the background, whose level was quite high, as can be seen at the cross-section of optical and topographical images for  $\lambda = 1500$  nm, averaged along 10 lines (corresponding to the width of 1  $\mu\text{m}$ ) perpendicular to the propagation direction [Fig. 2(i)].

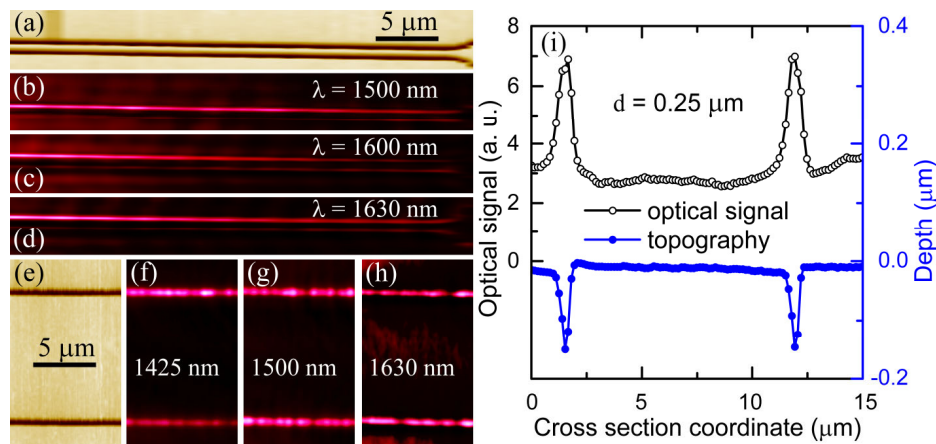


Fig. 2. Experimental results. SNOM (a) topographical and corresponding (b-d) optical images of coupling region for the DC with separation distance  $d = 0.25$   $\mu\text{m}$ , taken at different wavelengths: (b)  $\lambda = 1500$  nm, (c)  $\lambda = 1600$  nm, and (d)  $\lambda = 1630$  nm. SNOM (e) topographical and corresponding (f-h) optical images of output region for the same DC, taken at (f)  $\lambda = 1425$  nm, (g)  $\lambda = 1500$  nm, and (h)  $\lambda = 1630$  nm. (i) Cross-sections of the near-field optical (black hollow circles) and corresponding topographical (blue filled circles) images of (g), averaged along 10 lines perpendicular to the propagation direction.

### 3.2 CPP coupling for DCs with different separation distances

We carried out another series of experiments investigating CPP coupling at the wavelength of  $\lambda \approx 1500$  nm for the DCs with channels separation distance varied from 0.08 to 2.0  $\mu\text{m}$  (Fig. 3). Note that for the DC with separation distance of 0.08  $\mu\text{m}$ , as shown on the topographical image [Fig. 3(a)], the middle part between channels is slightly darker than the outside surface, meaning the level of this part is lower than the surface level. Later, it was confirmed with AFM measurements that, for this DC, two V-grooves are overlapped, with the middle part being lower by approximately 150 nm than the surface level. The coupling behavior for such DC is more difficult to understand and compare to other DCs, so that is why it was not chosen for the series with a varied wavelength described in Section 3.2.



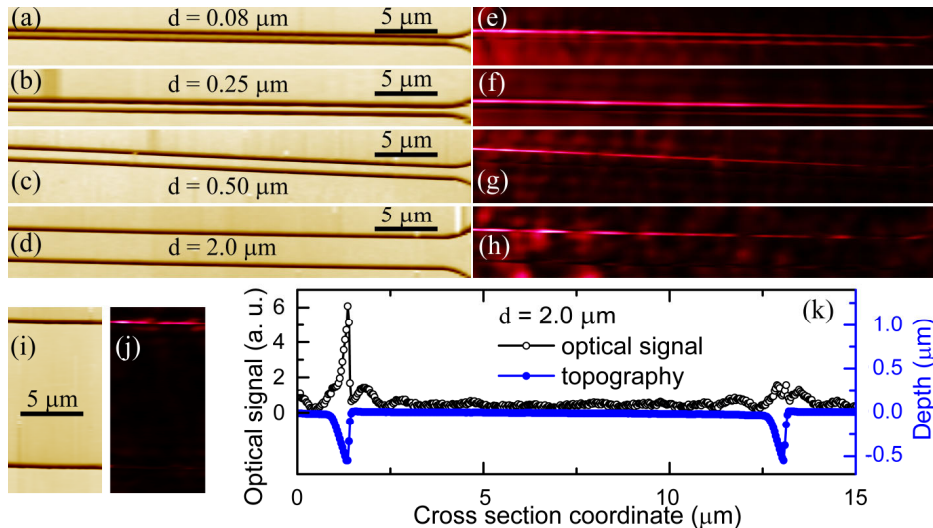


Fig. 3. SNOM (a-d) topographical and corresponding (e-h) optical images of coupling region for the DCs with different separation distances: (a), (e)  $d = 0.08 \mu\text{m}$ , (b), (f)  $d = 0.25 \mu\text{m}$ , (c), (g)  $d = 0.50 \mu\text{m}$ , (d), (h)  $d = 2.0 \mu\text{m}$ ; taken at the wavelength  $\lambda \approx 1500 \text{ nm}$ . SNOM (i) topographical and corresponding (j) optical images of output region for the DC with separation distance  $d = 2.0 \mu\text{m}$  at the same wavelength  $\lambda \approx 1500 \text{ nm}$ . (k) Cross-sections of the near-field optical (black hollow circles) and correspondent topographical (blue filled circles) images of (i), (j), averaged along 5 lines perpendicular to the DC.

Overall, the results showed the following: for the DCs with separation distances of  $0.08 \mu\text{m}$  and  $0.25 \mu\text{m}$ , the power splitting was approximately equal, while for the DC with the separation distance of  $0.50 \mu\text{m}$  the coupling became weaker, and finally for the DC with the separation distance of  $2.0 \mu\text{m}$  no coupling was observed. In order to be sure that no coupling occurred in the last case (relative to the background), we scanned by SNOM (similar to the case of DC with the separation distance of  $0.25 \mu\text{m}$  described in previous section) the output region of the DC, where two grooves are separated by about  $10 \mu\text{m}$  [Figs. 3(i), 3(j)]. The cross-section of these images, averaged along 5 lines (corresponding to the width of  $1 \mu\text{m}$ ) perpendicular to the DC, can be seen in Fig. 3(k). As was expected, the measured optical signal in the adjacent V-groove was at the same level as the background (which is about 6 times smaller than the intensity in the main V-groove); therefore the CPP mode intensity in the adjacent V-groove could not be resolved. Note that the optical signal in the point, corresponding to the deepest part in topography of the adjacent groove, is slightly smaller than the optical signals in nearby points. It could be explained by the enhancement of the background (stray light) at the edges of the groove [28]. This effect is also present for the main groove as a slight variation in the mode profile. However, one can conclude that crosstalk, which could be defined as the ratio of the CPP intensity in the adjacent V-groove to the one in the main groove, is less than  $1/6$ , or approximately  $-8 \text{ dB}$ . It can be compared with the crosstalk of 1 (0 dB), measured for the DC with separation distance of  $0.25 \mu\text{m}$  [see Fig. 2(i)]. It should be noted that the two sets of images (for the DCs with separation distances of  $0.25 \mu\text{m}$  and  $2.0 \mu\text{m}$ ) were made with different SNOM probes (due to its low life-time), which explains the minor differences, such as different background level and different depth of grooves in topography, but it does not influence the crosstalk.

#### 4. Numerical simulation

The directional coupling of CPP modes was investigated numerically by calculating the effective indexes (both real and imaginary parts) of even and odd modes of the double CPPW configuration using the finite-element method (FEM) implemented in the commercial

software COMSOL. The simulations were conducted for the wavelength of  $\lambda = 1425$  nm, 1500 nm, and 1630 nm, with the dielectric permittivity of gold taken from Palik and Ghosh data set [29], and the refractive index of air set to 1. The geometry used in simulations was the following: two V-grooves cut in the gold, each having the width  $w = 630$  nm and depth  $H = 1420$  nm (resulting in the groove angle  $\theta \approx 25^\circ$ ), separated by the distance  $d$  (measured at the surface level), which was varied from 40 nm to 3  $\mu\text{m}$  [Fig. 4(a)]. To avoid singularities and the appearance of wedge plasmon polariton (WPP) modes [28, 30], the edges of the grooves and their bottom angles were rounded with curvature radii 50 nm and 10 nm, respectively (later it was confirmed that this rounding does not influence significantly the mode effective index and coupling efficiency, it just removes the local field maxima created by the field enhancement at the sharp edges). The calculated distribution of the horizontal electric field component  $E_x$  (which dominates in the dielectric) for the even and odd modes at the wavelength  $\lambda = 1500$  nm and separation distance  $d = 0.25$   $\mu\text{m}$  are shown in Figs. 4(b), 4(c). Note the sign change of the  $E_x$  for the even mode, while it is the same in both V-grooves for the odd mode.

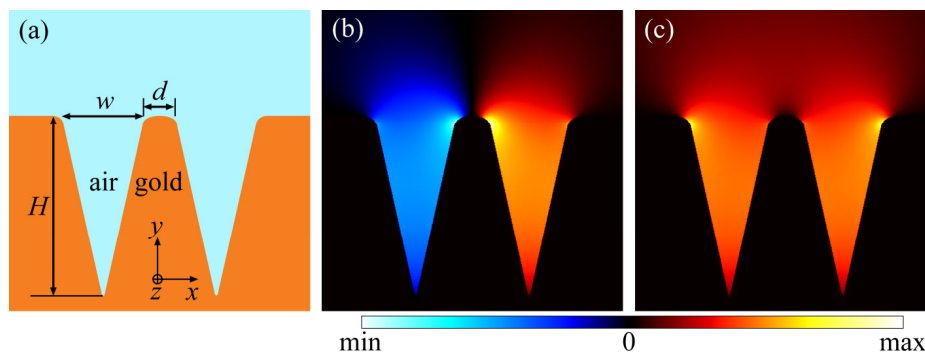


Fig. 4. (a) Coupling configuration used for simulations. Modal structure of (b) even and (c) odd modes represented as the distribution of the dominant electric field component  $E_x$ , calculated by the use of the finite-element method (FEM) implemented in the commercial software COMSOL. All panels have a lateral size of 2.5  $\mu\text{m}$ .

Using the aforementioned technique, the odd and even mode effective indexes were calculated for the range of the separation distance  $d$  from 40 to 3000 nm at the wavelength  $\lambda = 1500$  nm. Their real parts,  $N_{\text{odd}}$  and  $N_{\text{even}}$ , were compared to the one calculated for the CPP mode in the single groove with the same geometrical dimensions,  $N_{\text{CPP}}$ , and to the mode effective index of surface plasmon polaritons  $N_{\text{SPP}}$  [Fig. 5(a)]. Note the large difference between  $N_{\text{odd}}$  and  $N_{\text{even}}$  at small separation distances  $d$ . This could partially explain the (approximately) equal power splitting observed in the experiment for the DC with separation distance  $d = 0.25$   $\mu\text{m}$  [Fig. 2], since scattering by surface roughness increase rapidly when the mode index approaches the light line. Indeed, the maximum size  $r_{\text{max}}$  of a scatterer that efficiently scatters the bound waveguide mode into propagating (out of waveguide) waves can be evaluated by the following expression:  $\Delta N k_0 r_{\text{max}} \sim 2\pi$ , where  $k_0 = 2\pi/\lambda$ , and  $\Delta N = N_{\text{mode}} - 1$ , implying that larger and thereby stronger scatterers start contributing to the mode scattering loss with the decrease of  $N_{\text{mode}}$ . The even mode, having a considerably smaller effective index, is therefore expected to exhibit significantly stronger scattering losses that might result in its complete attenuation, leaving only the odd mode propagating in a DC and thus resulting in the equal power splitting between two individual CPP modes.

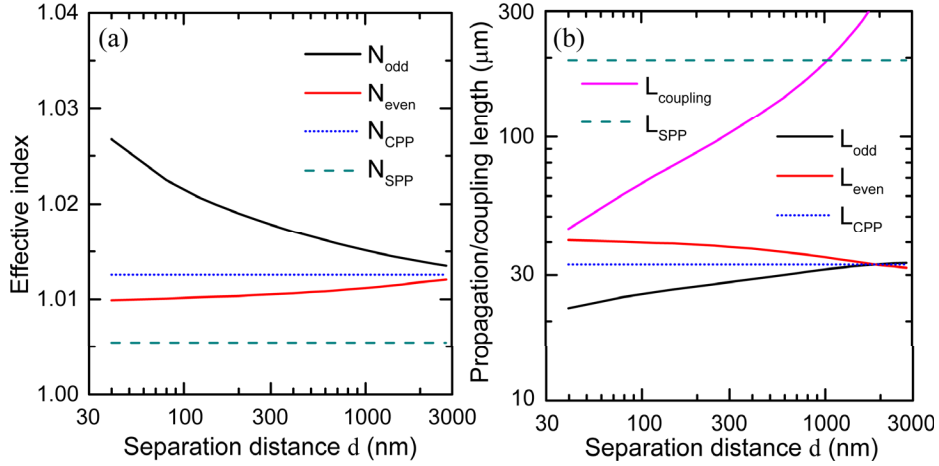


Fig. 5. (a) Effective mode index, calculated for odd (solid black line) and even (solid red line) modes, and compared to the one of CPP (dotted blue line) and SPP (dashed green line) modes, at the wavelength  $\lambda = 1500$  nm. (b) Propagation length of odd (solid black line) and even (solid red line) modes, compared to the one of CPP (dotted blue line) and SPP (dashed green line) modes, along with the coupling length (solid pink line), at  $\lambda = 1500$  nm.

The imaginary part of the mode effective index is natural to represent through the mode propagation length:  $L = 1/(2\text{Im}[n]k_0) = \lambda/(4\pi\text{Im}[n])$ . The propagation lengths of odd and even modes,  $L_{\text{odd}}$  and  $L_{\text{even}}$ , were compared to the one calculated for the CPP ( $L_{\text{CPP}}$ ) and SPP ( $L_{\text{SPP}}$ ) modes, along with the coupling length  $L_{\text{coupling}}$  [Fig. 5(a)]. The coupling length  $L_{\text{coupling}}$  is the distance (along the DC) between the beginning of the coupling region and the point, where the crosstalk (the ratio of the CPP intensity in the adjacent V-groove to the one in the main groove) is at maxima. The electric field in each groove versus the coordinate  $z$  along the propagation direction can be represented as follows:

$$\mathbf{E}_{\text{main}}(x, y, z) = \mathbf{E}_{\text{even}}(x, y) \exp(-in_{\text{even}}k_0z) + \mathbf{E}_{\text{odd}}(x, y) \exp(-in_{\text{odd}}k_0z), \quad (1a)$$

$$\mathbf{E}_{\text{adjacent}}(x, y, z) = \mathbf{E}_{\text{even}}(x, y) \exp(-in_{\text{even}}k_0z) + \mathbf{E}_{\text{odd}}(x, y) \exp(-in_{\text{odd}}k_0z), \quad (1b)$$

where the effective index  $n_{\text{even,odd}}$  contains both the real part  $N_{\text{even,odd}}$  and the imaginary part responsible for the finite propagation length. In the beginning of the coupling region, at  $z = 0$ , there is no intensity in the adjacent groove. Assuming the field distribution being mostly the same in magnitude for odd and even mode,  $|\mathbf{E}_{\text{even}}(x, y)| \approx |\mathbf{E}_{\text{odd}}(x, y)|$ , and taking into account the sign change of dominant field component  $E_x$  for the even mode, one can therefore calculate the crosstalk XT as the function of the distance  $z$  along the propagation direction:

$$\text{XT}(z) = I_{\text{adjacent}}(z)/I_{\text{main}}(z) = |\tan(\Delta nk_0z)|^2, \quad (2)$$

where  $\Delta n = (n_{\text{even}} - n_{\text{odd}})/2$  is the half-difference for the effective indexes of odd and even modes. In order to estimate the coupling length  $L_{\text{coupling}}$ , one can neglect the imaginary part of  $\Delta n$  (it is a valid assumption, since the propagation length is much larger than the wavelength), so the maximum crosstalk will be at  $\Delta nk_0L_{\text{coupling}} = \pi/2$ , or

$$L_{\text{coupling}} = \frac{\lambda}{2(N_{\text{odd}} - N_{\text{even}})}. \quad (3)$$

Using this equation the coupling length was calculated for the range of separation distances  $d$  from 40 to 3000 nm at the wavelength  $\lambda = 1500$  nm, and compared with the CPP propagation length [Fig. 5(b)]. Note that for the separation distance of 0.25  $\mu\text{m}$  the coupling length is around 90  $\mu\text{m}$ , which is almost twice as long as the 40- $\mu\text{m}$ -long coupling region of

the DCs used in our experiment, explaining the observed approximately equal power splitting between two individual CPP modes at the output.

A slight difference between the field magnitude distributions for even and odd modes [Figs. 4(b), 4(c)] caused different propagation lengths for these modes [Fig. 5(b)], especially for small separation distances. As was noted before, when the damping is different for even and odd modes, the maximum crosstalk should be smaller. Indeed, if imaginary part of  $\Delta n$  is non-zero, Eq. (2) can be presented as:

$$XT(z) = \left| \tan(\{\text{Re}[\Delta n] + i \text{Im}[\Delta n]\} k_0 z) \right|^2 = \left| \frac{\tan(\text{Re}[\Delta n] k_0 z) + i \tanh(\text{Im}[\Delta n] k_0 z)}{1 + i \tan(\text{Re}[\Delta n] k_0 z) \tanh(\text{Im}[\Delta n] k_0 z)} \right|^2. \quad (4)$$

At coupling distance  $z = L_{\text{coupling}}$  calculated by Eq. (3),  $\tan(\text{Re}[\Delta n] k_0 z) \rightarrow \infty$ , so the maximum crosstalk will be:

$$XT_{\text{max}} = XT(L_{\text{coupling}}) = \left\{ \tanh(\text{Im}[\Delta n] k_0 L_{\text{coupling}}) \right\}^{-2}. \quad (5)$$

Using the relationship between imaginary part of the mode effective index and its propagation length,  $L = 1/(2\text{Im}[n]k_0)$ , the expression  $\text{Im}[\Delta n]k_0$  can be approximated as

$$\text{Im}[\Delta n]k_0 = \frac{n_{\text{even}} - n_{\text{odd}}}{2} = \frac{1}{2} \left( \frac{1}{2L_{\text{even}}} - \frac{1}{2L_{\text{odd}}} \right) = \frac{L_{\text{odd}} - L_{\text{even}}}{4L_{\text{even}}L_{\text{odd}}} \approx \frac{\Delta L}{4L_{\text{CPP}}^2}, \quad (6)$$

where  $\Delta L = L_{\text{odd}} - L_{\text{even}}$  is the difference in propagation length for even and odd modes. Applying this approximation to Eq. (5), one could finally get the expression for maximum crosstalk:

$$XT_{\text{max}} = XT(L_{\text{coupling}}) = \left\{ \tanh \left( \frac{1}{4} \frac{\Delta L}{L_{\text{CPP}}} \frac{L_{\text{coupling}}}{L_{\text{CPP}}} \right) \right\}^{-2}. \quad (7)$$

So it is clear now that the switching effect (when all energy transfers to the adjacent channel, i.e., when the crosstalk is much higher than 1) is limited, since for separation distances such as  $L_{\text{coupling}} \leq L_{\text{CPP}}$ , as followed from Fig. 5(b),  $\Delta L \approx L_{\text{CPP}}$ , resulting in  $XT_{\text{max}} \approx \{\tanh(1/4)\}^{-2} \approx 16 \approx 12$  dB. Note that for DCs with larger coupling length, when  $L_{\text{coupling}} \gg L_{\text{CPP}}$ , it would be difficult to realize the switching effect practically.

Using the effective mode indexes calculated for the separation distance  $d = 0.25 \mu\text{m}$  and wavelength  $\lambda = 1500 \text{ nm}$ , we compared the expected change of intensities along the propagation direction in the main and adjacent grooves,  $I_{\text{main}}$  and  $I_{\text{adjacent}}$ , with the values taken from the experimental data along the coordinate  $z$  corresponding to the bottom of each groove with the averaged background being subtracted [Figs. 6(a), 6(b)]. Note that it is difficult to properly take into account the influence of the background since its amplitude and phase inside the groove are unknown. It is seen that the overall behavior of optical signals along the propagation direction is in fair agreement with the conducted simulations. Here one should bear in mind that the intensity of CPP mode (measured by the SNOM) has a strong dependence on the SNOM probe penetration depth inside the V-groove [24, 30, 31]. The later, along with the background level, was used to estimate the uncertainty of experimental data, which can be seen as error bars in Fig. 6(b).

Furthermore, the crosstalk  $I_{\text{adjacent}}/I_{\text{main}}$  was calculated for the separation  $d$  varied from 40 to 3000 nm, at three different wavelengths: 1425, 1500, and 1630 nm, and at different coordinates:  $z = 40 \mu\text{m}$  (corresponded to the length of the coupling region for the DCs used in the experiments) and  $z = L_{\text{CPP}}$  (varied with the wavelength:  $L_{\text{CPP}} = 30 \mu\text{m}$  at  $\lambda = 1425 \text{ nm}$ ,  $33 \mu\text{m}$  at  $\lambda = 1500 \text{ nm}$ , and  $38 \mu\text{m}$  at  $\lambda = 1630 \text{ nm}$ ) [Fig. 6(c)]. As was noted before, the CPP propagation length is an important length parameter for the practical realization of waveguide components, so in order to use wavelength-dependent behavior of DCs (i.e., for switching,

modulation, wavelength demultiplexing, and power splitting), one should look for DC configurations that would result in the coupling length being smaller than (or, at least, about) the propagation length  $L_{\text{CPP}}$ . In addition, the results presented in Fig. 6(c) can be used to evaluate the smallest CPPW separation distance that would result in the crosstalk being below a given limit. For example, if the crosstalk should be less than  $-10$  dB at the wavelength of  $1500$  nm, then V-grooves should be separated by more than  $1 \mu\text{m}$ . Thus this figure reflects the limit on integration density of considered CPPWs and corresponding waveguide components. Finally, it should be borne in mind that the above results are related to the V-grooves in gold having particular depth of  $1.4 \mu\text{m}$  and groove angle of  $25^\circ$ , so that the CPPW characteristics have to be scaled accordingly when considering other V-groove parameters [30, 31].

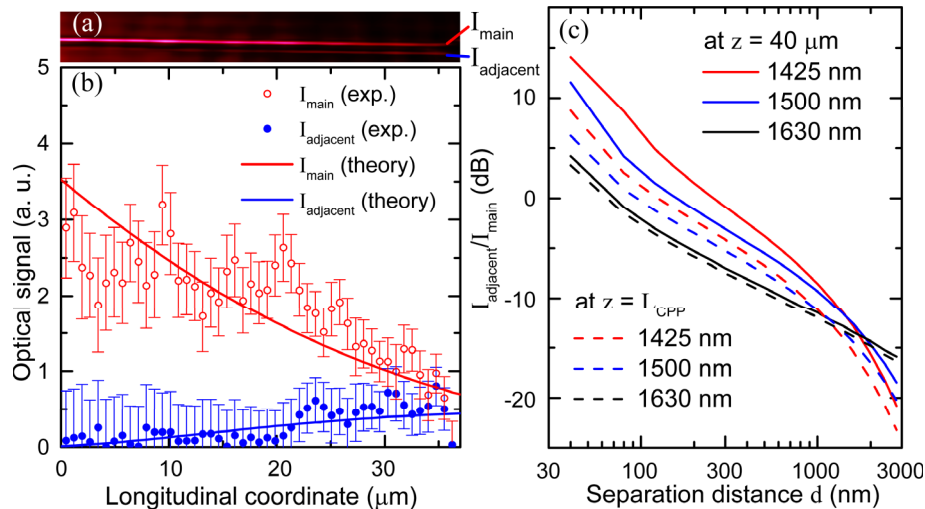


Fig. 6. (a) SNOM optical image of coupling region for the DC with separation distance  $d = 0.25 \mu\text{m}$ , taken at the wavelength  $\lambda = 1500$  nm. (b) Experimental values of the optical signal, varied along the propagation direction, corresponding to optical image (a), calculated inside the main (red hollow circles) and adjacent (blue filled circles) grooves relative to the background, and compared with the results of numerical simulations (red and blue lines for the intensities in the main and adjacent grooves, correspondingly). Error bars are estimated from the maximum variations of the CPP intensity, where we took into account the influence of the background level and the penetration depth of SNOM probe into the groove. (c) Crosstalk  $I_{\text{adjacent}}/I_{\text{main}}$ , calculated numerically for separation  $d$  varied from  $40$  to  $3000$  nm, at different wavelengths:  $1425$  nm (red lines),  $1500$  nm (blue lines), and  $1630$  nm (black lines), and at different longitudinal coordinates:  $z = 40 \mu\text{m}$  (solid lines) and  $z = L_{\text{CPP}}$  (dashed lines).

## 5. Conclusions

Overall, we studied the directional coupling of CPP modes guided by V-grooves cut in gold film, separated by distance  $d \approx 0.08\text{-}2 \mu\text{m}$ . The experimental observations performed by the use of SNOM showed the strong coupling for  $d = 0.25 \mu\text{m}$  (output crosstalk was approximately  $0$  dB after the  $40\text{-}\mu\text{m}$ -long coupling region), independently on the wavelength (over the range  $1425\text{-}1630$  nm). With the increase in separation distance  $d$  the output crosstalk decreased, and for  $d = 2.0 \mu\text{m}$  no coupling was observed.

In addition to experimental study, we performed numerical simulations based on finite-element method implemented in commercial software COMSOL. For  $d = 0.25 \mu\text{m}$  the calculated coupling length was  $90 \mu\text{m}$  (which is almost twice as long as the length of coupling region), explaining approximately equal power splitting obtained in the experiment. Moreover, significantly different propagation losses (related both to different electric field distribution in metal and different effective indexes with corresponding different losses on scattering at surface roughness) for even and odd mode explained the (approximately) equal power splitting for the whole range of wavelengths ( $1425\text{-}1630$  nm). On the other hand, the

coupling length calculated for the DC with the separation  $d = 2.0 \mu\text{m}$  resulted in the output crosstalk of  $-14 \text{ dB}$ , supporting the experimentally obtained data (from which the crosstalk was evaluated to be less than  $-8 \text{ dB}$ ).

The results of numerical simulations also provide the important design guidelines for practical realization of both coupling-dependent waveguide components (utilizing DCs for switching, modulation, wavelength demultiplexing, and power splitting), and, oppositely, configurations in which the crosstalk should be avoided. The latter, with the proper criterion, could be treated as the upper limit on the density of CPP-based waveguide components.

### **Acknowledgments**

The authors gratefully acknowledge financial support from the Danish Council for Independent Research (FTP-project no. 09-072949 ANAP) and the European Research Council (ERC) (grant 227577).

# Appendix A.3

LR-DLSPP directional coupling

---

# Directional coupling in long-range dielectric-loaded plasmonic waveguides

Vladimir A. Zenin,<sup>1,2,\*</sup> Zhanghua Han,<sup>1</sup> Valentyn S. Volkov,<sup>1</sup> Kristjan Leosson,<sup>3</sup>  
Ilya P. Radko,<sup>1</sup> and Sergey I. Bozhevolnyi<sup>1</sup>

<sup>1</sup>Department of Technology and Innovation, University of Southern Denmark, Niels Bohrs Allé 1, Odense, Denmark

<sup>2</sup>Laboratory of Nanooptics and Femtosecond Electronics, Moscow Institute of Physics and Technology (State University), Institutsky Lane 9, Dolgoprudny, Russia

<sup>3</sup>Department of Physics, Science Institute, University of Iceland, Dunhagi 3, IS-107 Reykjavik, Iceland  
\*zenin@iti.sdu.dk

**Abstract:** Directional couplers (DCs) based on long-range dielectric-loaded surface plasmon-polariton waveguides (LR-DLSPPWs) operating at telecom wavelengths are studied both numerically and experimentally. The investigated LR-DLSPPWs are formed by  $\sim 1.2\text{-}\mu\text{m}$ -high and  $1\text{-}\mu\text{m}$ -wide polymer ridges fabricated atop of  $15\text{-nm}$ -thick and  $500\text{-nm}$ -wide gold stripes supported by a  $288\text{-nm}$ -thickOrmoclear polymer deposited on a low-index ( $n_s \approx 1.34$ ) layer of Cytop. DC structures consisting of sine-shaped S-bends (having an offset of  $\sim 10\text{ }\mu\text{m}$  over a distance of  $\sim 20\text{ }\mu\text{m}$ ) and  $\sim 100\text{-}\mu\text{m}$ -long parallel LR-DLSPPWs with a center-to-center separation of  $2\text{ }\mu\text{m}$  are characterized using scanning near-field microscopy. The experimentally obtained values of the propagation length ( $\sim 400\text{ }\mu\text{m}$ ), S-bend loss ( $\sim 4\text{ dB}$ ) and coupling length ( $\sim 100\text{ }\mu\text{m}$ ) are found in good agreement with the numerical simulations, indicating a significant potential of LR-DLSPPWs for the realization of various plasmonic components.

©2013 Optical Society of America

**OCIS codes:** (240.6680) Surface plasmons; (250.5403) Plasmonics; (250.5300) Photonic integrated circuits.

## References and links

1. S. A. Maier, *Plasmonics: Fundamentals and Applications* (Springer, 2007).
2. S. Lal, S. Link, and N. J. Halas, "Nano-optics from sensing to waveguiding," *Nat. Photonics* **1**(11), 641–648 (2007).
3. J. N. Anker, W. P. Hall, O. Lyandres, N. C. Shah, J. Zhao, and R. P. Van Duyne, "Biosensing with plasmonic nanosensors," *Nat. Mater.* **7**(6), 442–453 (2008).
4. D. K. Gramotnev and S. I. Bozhevolnyi, "Plasmonics beyond the diffraction limit," *Nat. Photonics* **4**(2), 83–91 (2010).
5. R. Zia, J. A. Schuller, A. Chandran, and M. L. Brongersma, "Plasmonics: the next chip-scale technology," *Mater. Today* **9**(7-8), 20–27 (2006).
6. J. Takahara, S. Yamagishi, H. Taki, A. Morimoto, and T. Kobayashi, "Guiding of a one-dimensional optical beam with nanometer diameter," *Opt. Lett.* **22**(7), 475–477 (1997).
7. M. Quinten, A. Leitner, J. R. Krenn, and F. R. Aussenegg, "Electromagnetic energy transport via linear chains of silver nanoparticles," *Opt. Lett.* **23**(17), 1331–1333 (1998).
8. I. V. Novikov and A. A. Maradudin, "Channel polaritons," *Phys. Rev. B* **66**(3), 035403 (2002).
9. G. T. Reed and A. P. Knights, *Silicon Photonics: An Introduction* (John Wiley & Sons, Inc., 2004).
10. A. Liu, L. Liao, Y. Chetrit, J. Basak, H. Nguyen, D. Rubin, and M. Paniccia, "Wavelength division multiplexing based photonic integrated circuits on silicon-on-insulator platform," *IEEE J. Sel. Top. Quantum Electron.* **16**(1), 23–32 (2010).
11. F. E. Doany, B. G. Lee, C. L. Schow, C. K. Tsang, C. Baks, Y. Kwark, R. John, J. U. Knickerbocker, and J. A. Kash, "Terabit/s-class 24-channel bidirectional optical transceiver module based on TSV Si carrier for board-level interconnects," in *Proceedings of IEEE Conference on Electronic Components and Technology* (2010), pp. 58–65.
12. A. Biberman, B. G. Lee, N. Sherwood-Droz, M. Lipson, and K. Bergman, "Broadband operation of nanophotonic router for silicon photonic networks-on-chip," *IEEE Photon. Technol. Lett.* **22**(12), 926–928 (2010).
13. Yu. A. Vlasov and S. J. McNab, "Losses in single-mode silicon-on-insulator strip waveguides and bends," *Opt. Express* **12**(8), 1622–1631 (2004).



14. G. Giannoulis, D. Kalavrouziotis, D. Apostolopoulos, S. Papaioannou, A. Kumar, S. I. Bozhevolnyi, L. Markey, K. Hassan, J.-C. Weeber, A. Dereux, M. Baus, M. Karl, T. Tekin, O. Tsilipakos, A. K. Pitolakis, E. E. Kriezis, K. Vyrsokinos, H. Avramopoulos, and N. Pleros, "Data transmission and thermo-optic tuning performance of dielectric-loaded plasmonic structures," *IEEE Photon. Technol. Lett.* **24**(5), 374–376 (2012).
15. J. Gosciniaik, L. Markey, A. Dereux, and S. I. Bozhevolnyi, "Efficient thermo-optically controlled Mach-Zehnder interferometers using dielectric-loaded plasmonic waveguides," *Opt. Express* **20**(15), 16300–16309 (2012).
16. T. Holmgaard and S. I. Bozhevolnyi, "Theoretical analysis of dielectric-loaded surface plasmon-polariton waveguides," *Phys. Rev. B* **75**(24), 245405 (2007).
17. T. Holmgaard, Z. Chen, S. I. Bozhevolnyi, L. Markey, A. Dereux, A. V. Krasavin, and A. V. Zayats, "Wavelength selection by dielectric-loaded plasmonic components," *Appl. Phys. Lett.* **94**(5), 051111 (2009).
18. J. Gosciniaik, S. I. Bozhevolnyi, T. B. Andersen, V. S. Volkov, J. Kjølstrup-Hansen, L. Markey, and A. Dereux, "Thermo-optic control of dielectric-loaded plasmonic waveguide components," *Opt. Express* **18**(2), 1207–1216 (2010).
19. J. Grandidier, G. C. des Francs, S. Massenet, A. Bouhelier, L. Markey, J.-C. Weeber, C. Finot, and A. Dereux, "Gain-assisted propagation in a plasmonic waveguide at telecom wavelength," *Nano Lett.* **9**(8), 2935–2939 (2009).
20. C. Garcia, V. Coello, Z. Han, I. P. Radko, and S. I. Bozhevolnyi, "Partial loss compensation in dielectric-loaded plasmonic waveguides at near infra-red wavelengths," *Opt. Express* **20**(7), 7771–7776 (2012).
21. P. Berini, "Plasmon-polariton waves guided by thin lossy metal films of finite width: Bound modes of symmetric structures," *Phys. Rev. B* **61**(15), 10484–10503 (2000).
22. T. Holmgaard, J. Gosciniaik, and S. I. Bozhevolnyi, "Long-range dielectric-loaded surface plasmon-polariton waveguides," *Opt. Express* **18**(22), 23009–23015 (2010).
23. J. Gosciniaik, T. Holmgaard, and S. I. Bozhevolnyi, "Theoretical analysis of long-range dielectric-loaded surface plasmon polariton waveguides," *J. Lightwave Technol.* **29**(10), 1473–1481 (2011).
24. V. S. Volkov, Z. Han, M. G. Nielsen, K. Leosson, H. Keshmiri, J. Gosciniaik, O. Albrektsen, and S. I. Bozhevolnyi, "Long-range dielectric-loaded surface plasmon polariton waveguides operating at telecommunication wavelengths," *Opt. Lett.* **36**(21), 4278–4280 (2011).
25. H. Micro Resist Technology GmbH, Berlin, Germany, [www.microresist.de](http://www.microresist.de).
26. E. Palik and G. Ghosh, *Handbook of Optical Constants of Solids II* (Academic Press, 1991).
27. S. I. Bozhevolnyi, B. Vohnsen, and E. A. Bozhevolnaya, "Transfer functions in collection scanning near-field optical microscopy," *Opt. Commun.* **172**(1-6), 171–179 (1999).
28. I. P. Radko, S. I. Bozhevolnyi, and N. Gregersen, "Transfer function and near-field detection of evanescent waves," *Appl. Opt.* **45**(17), 4054–4061 (2006).
29. M. Heiblum and J. Harris, "Analysis of curved optical waveguides by conformal transformation," *IEEE J. Quantum Electron.* **11**(2), 75–83 (1975).

## 1. Introduction

Surface plasmon-polaritons (SPPs), which are surface electromagnetic waves propagating along a metal-dielectric interface [1], have been intensively studied during the last decade due to their large number of potential applications, ranging from telecommunications and signal processing to biochemistry and sensing [2–4]. Waveguiding is one of the several particularly interesting applications of plasmonics, since there is an exciting perspective to combine large operational bandwidth of photonics with high-density integration feasible in plasmonics [5]. Among various types of plasmonic waveguides, a number of SPP-based configurations support strongly confined (in the lateral direction) modes, whose confinement can be deeply subwavelength. Those are, for example, metal nanowires [6], chains of nanospheres [7], as well as V-grooves cut in metal surfaces [8]. One of the challenges shared by all subwavelength SPP waveguides is considerable propagation losses, as the mode confinement is always achieved by concentrating large amount of energy in metal, thereby decreasing the spatial extent of the field in dielectric. As a result, one can realize strong field-enhancement phenomena, which can be used for sensing applications, but, on the other hand, this leads to high ohmic losses in metal and a drastic decrease of mode propagation length. In other words, an SPP waveguide configuration is subjected to the propagation length–confinement trade-off.

Considering only these two characteristics, plasmonics has a very strong competitor, viz., silicon photonics, which during the last decade has also gained a tremendous interest and progress [9] in the development of most of the critical components required for optical interconnect applications [10], leading to remarkable achievements both with respect to chip-level transceiver [11] and routing [12] circuitry applications. Having similar to plasmonic waveguides mode confinement and substantially larger propagation length [13], silicon-on-

insulator strip waveguides are often considered to be superior to plasmonic ones. However, metal stripes as an inherent part of plasmonic waveguides provides easy access to the external electrodes offering certain advantages for the implementation of electro- and thermo-optic modulation. The fact that the SPP fields reach their maximum at the metal–dielectric interface makes such modulation substantially more energetically efficient than in the case of silicon photonics, since controlling electrodes can be placed right in the center of the SPP mode. Indeed, a low-energy thermo-optical tuning and fast error-free 10-Gb/s transmission through a dielectric-loaded plasmonic waveguide (DLSPW) has been demonstrated recently [14, 15] as a proof of principle. The DLSPWs confine regular SPPs by use of a dielectric ridge on top of a smooth metal film [16], which introduces an effective refractive index difference. Among all plasmonic configurations, DLSPWs are so far the only waveguides that have been exploited for the realization of complex circuit elements [17], active control [18], and partial loss compensation using optical pumping [19, 20]. Furthermore, the absorption losses in DLSPWs can be significantly reduced by using the long-range SPP configuration [21], in which a thin metal stripe is positioned in a near-symmetric environment so that the longitudinal component of the electric field in metal (and hence the ohmic loss) is minimized. The corresponding long-range DLSPW (LR-DLSPW) configuration has recently been shown both theoretically [22, 23] and experimentally [24] to be able to guide an SPP mode over millimeter-long distances, while retaining relatively strong mode confinement. The usage of LR-DLSPW-based components seems very promising for practical applications, and it is therefore important to assess the potential of LR-DLSPW integration, which is determined by the mode coupling in adjacent waveguides. In this respect, investigations of directional couplers (DCs) should provide directly the minimum separation distance between LR-DLSPWs and thereby set the limit on their maximum integration density.

In this paper, we present the results of our study of LR-DLSPW-based DCs at telecom wavelengths in the range of 1425–1625 nm. The main goal of our work is to investigate the coupling strength between LR-DLSPWs for different separation distances and excitation wavelengths. The fabrication process, as well as imaging of the propagating LR-DLSPW modes by use of a scanning near-field optical microscope (SNOM), is described in the first section. The LR-DLSPW-based S-bends, as an important part of DCs and many other waveguide components, are investigated separately, and the corresponding experimental and theoretical results are presented in the second part. Finally, studies of LR-DLSPW-based DCs are reported in the last section, providing first experimental measurements of the coupling length for a DC-structure with the center-to-center separation of 2  $\mu\text{m}$  between waveguides and then numerical results obtained by use of finite element method (FEM) implemented in commercial software COMSOL.

## 2. Experimental results and numerical simulations

### 2.1 Fabrication process and imaging of LR-DLSPWs using SNOM

The LR-DLSPW structures [Fig. 1(a)] were fabricated by spinning a 288-nm-thick layer of a high-refractive-index UV-curable organic-inorganic hybrid materialOrmoclear ( $n_b \approx 1.53$ ) [25] onto a silicon wafer pre-coated with a 4- $\mu\text{m}$ -thick layer of amorphous fluoropolymer Cytop ( $n_s \approx 1.34$ ). Straight and bent 500-nm-wide and 15-nm-thick gold stripes were patterned with electron-beam lithography, metal evaporation, and lift-off. The waveguide fabrication has been completed using a second lithography step for patterning  $\sim 1.2\text{-}\mu\text{m}$ -high and 1- $\mu\text{m}$ -wide ridges of polymethyl methacrylate (PMMA,  $n_r \approx 1.49$ ) atop of the gold stripes, ensuring the single-mode LR-DLSPW operation. The height and width of the produced PMMA ridges was inspected with atomic force microscopy and found to be close to the designed values. The final step of the fabrication procedure was a cleavage of the sample resulting in  $\sim 150\text{-}\mu\text{m}$ -long waveguide structures.

First, we performed numerical modeling of the fabricated LR-DLSPW configuration by use of FEM implemented in commercial software COMSOL. The calculations revealed the electric field distribution inside the waveguide, with a dominating field component  $E_{\perp} = E_y$

[perpendicular to the surface; see Fig. 1(b)] being almost 5 times stronger than the parallel component  $E_{\parallel} = (E_x^2 + E_z^2)^{1/2}$  [note that a factor of 5 was also used when displaying the distributions of both components; see Fig. 1(c)]. The dielectric permittivity of gold was taken from Palik and Ghosh data set [26], and the refractive index of air was set to 1. The calculations confirmed the single-mode operation of the waveguide, and provided the following important mode characteristics: the mode effective index ( $N_{\text{eff}} = 1.37$ ) and propagation length ( $L_{\text{prop}} = 2.3$  mm) at  $\lambda = 1500$  nm.

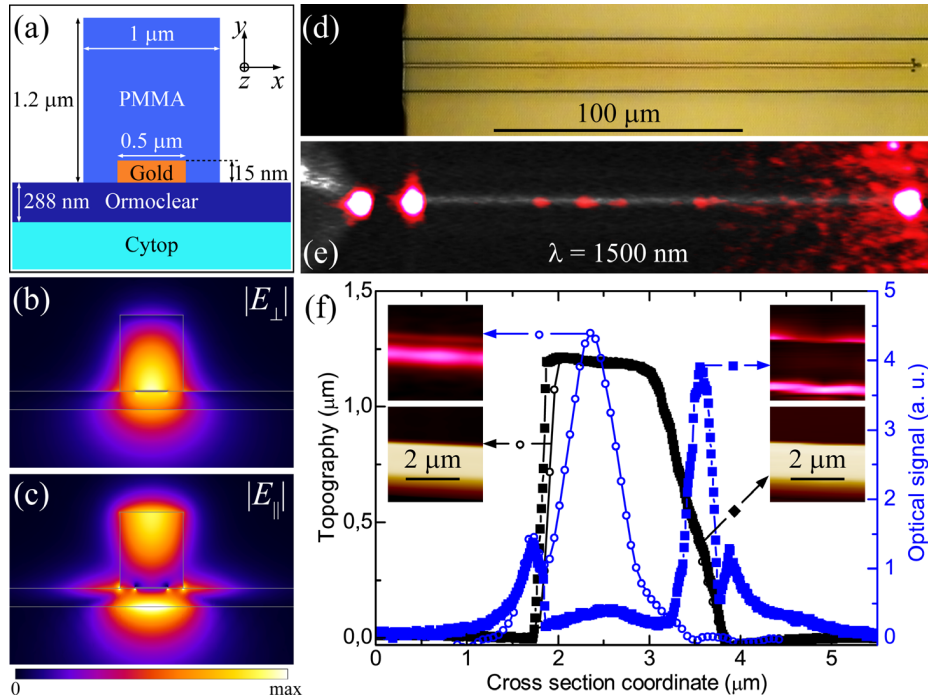


Fig. 1. (a) Schematic layout for the cross section of the fabricated LR-DLSPPW structure. All sizes except the metal stripe thickness are to scale. (b), (c) Fundamental LR-DLSPPW mode electric field distribution (components that are perpendicular and parallel to the surface, respectively), calculated at  $\lambda = 1500$  nm (the size of panels:  $4.5 \times 3 \mu\text{m}^2$ ). (d) Optical microscope top-view image of sample (straight waveguide) and (e) coupling arrangement superimposed with the far-field image taken at the wavelength  $\lambda = 1500$  nm. (f) Cross-sections of topographical and near-field optical images (shown as insets) taken on the same waveguide with different SNOM probes at  $\lambda = 1500$  nm.

In the next step, we experimentally investigated the SPP mode excitation and propagation in straight waveguides [Fig. 1(d)]. We excited the LR-DLSPPW mode by use of polarization-maintaining tapered-lensed fiber placed in front of the cleaved edge of waveguide and observed from above by an IR-camera with a microscope  $20\times$ -objective. The camera was used also for the far-field observation of the LR-DLSPPW mode excitation and propagation, when the TM-polarized light (electric field perpendicular to the sample surface) from a tunable laser (1425-1625 nm) was sent through the tapered fiber directly to the LR-DLSPPW input edge. The fabricated waveguide was terminated with an out-coupling diffraction grating, so that a bright spot was seen at the end of the waveguide, when the in-coupling fiber was adjusted well [Fig. 1(e)]. Also it was possible to see the track of the propagating LR-DLSPPW mode in the far-field, which was most probably produced by mode scattering on the imperfections of the waveguide, and its maximum intensity along with the maximum intensity of the output spot was used as an indicator of a good alignment of the in-coupling fiber [Fig. 1(e)].

After the far-field adjustments, we moved the whole fiber-sample arrangement under the SNOM head and mapped the intensity distributions near the investigated waveguide structure

by the uncoated sharp fiber tip used as a SNOM probe. The tip was scanning along the sample surface at a constant distance of a few nanometers maintained by shear-force feedback, and the radiation collected by the fiber was detected with a femtowatt InGaAs photoreceiver. The recorded near-field images showed the mode propagation with the propagation length estimated to be  $\sim 400 \mu\text{m}$  at excitation wavelength of 1500 nm. It was, however, interesting albeit somewhat unexpected to observe that the *imaged* mode shape strongly depended on the SNOM probe used. For some probes, the detected optical signal reached a maximum in the middle of the topographical image of waveguide [see left insets in Fig. 1(f) and corresponding cross-sections, plotted with hollow circles], whereas, for other probes, two pronounced local maxima were found at the sides of the waveguide [see right insets in Fig. 1(f)]. We relate this behavior to a strong influence of the fiber tip shape on its transfer function [27, 28]. Indeed, an axially symmetrical (and sharp) fiber tip collects only the field components perpendicular to the tip axis ( $E_x$  and  $E_z$ ), but, with even a small probe asymmetry being present, the *dominant* component of the LR-DLSPPW mode field,  $E_y$ , can be collected as well, producing the main signal contribution for a sufficiently large asymmetry. From the above numerical simulations [Figs. 1(b) and 1(c)] it is clearly seen, that, for the field in the air, where it is collected by the SNOM probe, the parallel component  $E_{\parallel}$  is mostly pronounced in the middle above the waveguide [which corresponds to the left inset in Fig. 1(f)], while the perpendicular component  $E_{\perp}$  has two maxima at the sides of the waveguide [which corresponds to the right inset in Fig. 1(f)]. Overall, as observed experimentally and conjectured from the simulations, the SNOM images of the LR-DLSPPW mode depend strongly on the shape and symmetry of the fiber tip, and, in general case, do not represent the actual LR-DLSPPW mode distribution. Importantly, the *average* strength of the SNOM signal can still be used to evaluate the dependence of the LR-DLSPPW mode power *along* the propagation direction.

### 2.2 LR-DLSPPW-based sine-shaped S-bends

Our next step was an investigation of LR-DLSPPW-based S-bends, as an important part of DCs and many other waveguide components. We fabricated our S-bends in a half-period sine shape, providing an offset of  $\sim 10 \mu\text{m}$  over a distance of  $\sim 20 \mu\text{m}$  [Fig. 2(a)]. Far-field images showed, along with a track of propagating mode and a bright output spot, relatively bright track along the S-bend, which can be ascribed to the increased scattering losses on the imperfections of rough bend [Fig. 2(b)]. Near-field measurements revealed mode propagation through the S-bend [Figs. 2(c) and 2(d)], with a total transmission decreasing from  $-3.5$  to  $-4.2$  dB with the increase of wavelength from 1425 nm to 1525 nm.

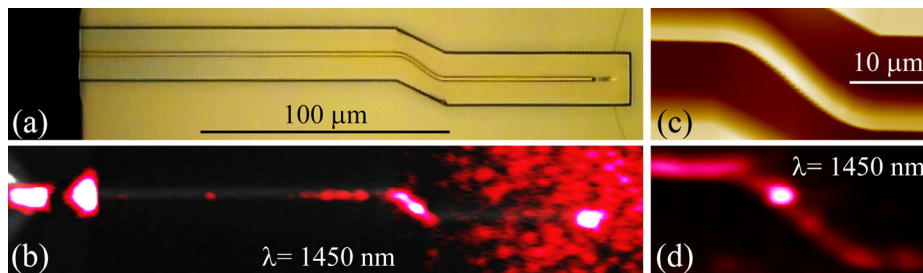


Fig. 2. (a) Optical microscope top-view image of sample (S-bend) and (b) coupling arrangement superimposed with the far-field image taken at the wavelength  $\lambda = 1450$  nm. (c) Pseudocolor topographical and (d) near-field optical images taken at  $\lambda = 1450$  nm.

In order to study theoretically our S-bend structures, we used a method of conformal transformation [29]. The idea is to apply a conformal transformation  $\{x, y, z\} \rightarrow \{u, v, w\}$  such that two new coordinates are defined by the following equation:

$$(u + iv) = r_{\text{bend}} \ln \left[ \frac{(x + iz)}{r_{\text{bend}}} \right], \quad (1)$$

where  $r_{\text{bend}}$  is bending radius,  $i$  is an imaginary unit, and origin is at a center of the bending arc [top-view schematic layout of bend is shown on inset of Fig. 3(a)]. As a result, a bent waveguide (with a constant bending radius  $r_{\text{bend}}$ ) is transformed into a straight waveguide with approximately the same cross-section (the coordinates of the sides of the ridge,  $r_{\text{bend}} \pm w_r/2$ , are transformed into  $r_{\text{bend}} \ln[(r_{\text{bend}} \pm w_r/2)/r_{\text{bend}}]$ , but the total width of the waveguide approaches the original value of  $w_r$  for relatively large bending radii,  $r_{\text{bend}} \gg w_r$ ). Such transformation leads to the following change in Laplacian:  $\nabla_{x,z}^2 \rightarrow \nabla_{u,v}^2 \exp(-2u/r_{\text{bend}})$ , so, for bent 2D-waveguides (waveguides, confined in one dimension – along  $u$ -axis), this conformal transformation is equivalent to the propagation in straight waveguide (with corresponding transformed cross-section) with refractive indexes of media changing as  $n^* = n_0 \exp(u/r_{\text{bend}})$ , where  $n_0$  is the original refractive index of corresponding medium. It should be noted that our LR-DLSPPW is 3-dimensional (2-dimensionally confined), so this theory cannot be applied strictly. However, as in the effective index method (EIM), one can replace LR-DLSPPW with equivalent set of layers along  $x$ -axis, each having its effective refractive index, and then apply conformal transformation for this equivalent 2D-waveguide.

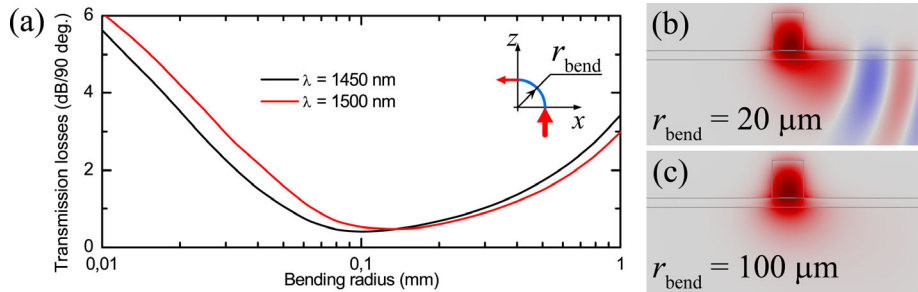


Fig. 3. (a) Transmission through 90-degrees bend as functions of the bending radius at  $\lambda = 1450$  and  $1500$  nm. The inset shows schematic layout of 90-degrees bend. (b), (c) Distribution of the dominating electric field  $E_y$  for bending radius of  $20$  and  $100 \mu\text{m}$ , respectively, showing strong leaky radiation for smaller bending radius. The size of panels:  $9 \times 4.5 \mu\text{m}^2$ .

So we made numerical simulations in such transformed LR-DLSPPW with exponentially changing refractive index of media for different bending radii by using FEM implemented in COMSOL, and calculated total transmission through the 90-degrees-bend [Fig. 3(a)]. The leaking radiation to the substrate due to the bending was clearly seen for small bending radii, and the smaller the radius, the stronger this radiation [see comparison of instant field distributions  $E_y$  in Figs. 3(b) and 3(c)]. In order to evaluate the transmission through our original sine-shaped S-bend, one should calculate the radius of curvature as a function of the length along the waveguide and then properly integrate propagation losses over the whole S-bend. Overall, the total transmission through the investigated S-bend was found to be  $-4.0$  dB at  $\lambda = 1425$  nm and decreases uniformly with the increase of wavelength up to  $-4.8$  dB at  $\lambda = 1525$  nm, which matches the experimental results within the accuracy of measurements.

### 2.3 LR-DLSPPW-based DCs

Finally, we proceeded to the investigation of directional coupling of LR-DLSPPW modes by use of direction couplers. In our sample coupling occurred between two straight LR-DLSPPWs, separated by center-to-center separation distance  $d = 2 \mu\text{m}$  over the distance of  $\sim 100 \mu\text{m}$  [Fig. 4(a)]. Each waveguide had the same cross-section as shown in Fig. 1(a). The mode was excited in one of the waveguides (called here as main and shown with a red arrow), which was completely straight; while the other waveguide (called here as adjacent) had S-bends in order to limit the coupling region. The far-field observations showed, along with the track of propagating modes, the distributed output between main and adjacent waveguides,

with the distribution depending strongly of the wavelength [Figs. 4(b) and 4(c)]. For the used range of wavelengths, 1425 – 1625 nm, we noticed almost complete switch for  $\lambda \approx 1450$  nm. Then we proceeded to the near-field investigation of DC, which revealed the intensity variation of modes in each waveguide along the propagation direction [Figs. 4(d) and 4(e)], where the intensity in the main channel was going down while the intensity in adjacent channel was going up. By the proper fitting of near-field data, we estimated the coupling length, which decreased uniformly from  $\sim 115 \mu\text{m}$  to  $\sim 75 \mu\text{m}$  with the increase of the wavelength from 1425 nm to 1625 nm.

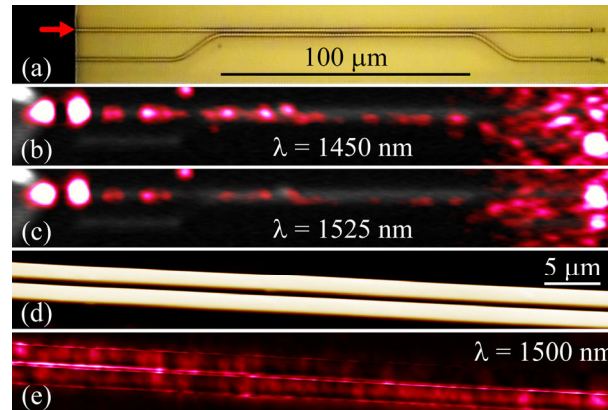


Fig. 4. (a) Optical microscope top-view image of sample (directional coupler) and (b), (c) coupling arrangement superimposed with the far-field image taken at the wavelength of  $\lambda = 1450$  and  $1525$  nm, respectively. Red arrow indicates the main waveguide, where the inputted mode was excited. (d) Pseudocolor topographical and (e) near-field optical images taken at  $\lambda = 1500$  nm. Center-to-center separation between waveguides is  $2 \mu\text{m}$ .

The directional coupling of LR-DLSPPW modes was then investigated numerically by use of the FEM implemented in COMSOL [Figs. 5(a) and 5(b)]. The first set of simulations was made for the varying center-to-center separation distance  $d$  (from  $1.2$  to  $5 \mu\text{m}$ ) at a fixed excitation wavelength  $\lambda = 1500$  nm [Fig. 5(c)]. The other set of simulations was made for the varying free-space excitation wavelength  $\lambda$  (from  $1400$  to  $1650$  nm) for DC with fixed center-to-center waveguides separation distance  $d = 2 \mu\text{m}$  [Fig. 5(d)]. The results were plotted in terms of effective mode index (of even and odd modes and compared with the one of a single LR-DLSPPW mode and the refractive index of the substrate) and coupling length (compared with the propagation length of single LR-DLSPPW mode and experimental results).

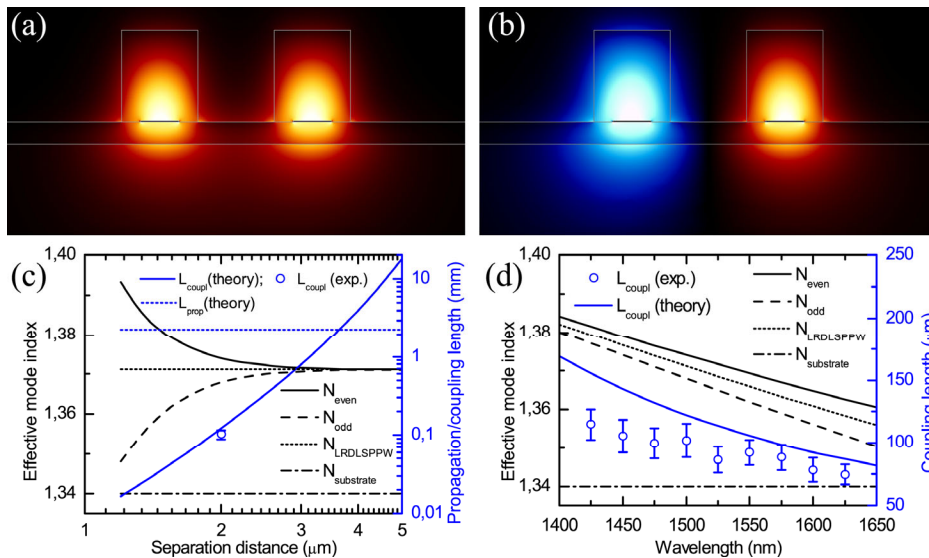


Fig. 5. (a), (b)  $E_y$ -field distribution of even and odd modes, respectively, for center-to-center separation  $d = 2 \mu\text{m}$  at  $\lambda = 1500 \text{ nm}$ . The size of panels:  $6 \times 3 \mu\text{m}^2$ . (c) Effective mode indexes (for even and odd modes, single LR-DLSPPW mode, and refractive index of substrate) and propagation/coupling length as a function of center-to-center separation distance  $d$  at fixed excitation wavelength  $\lambda = 1500 \text{ nm}$  (experimental datum is represented by a hollow circle). (d) Effective mode indexes and coupling length as a function of free-space excitation wavelength  $\lambda$  at fixed center-to-center separation distance  $d = 2 \mu\text{m}$  (experimental data are represented by hollow circles).

One can see that, by varying the separation between waveguides, one can vary coupling strength in the wide range, so one can achieve coupling length as low as  $20 \mu\text{m}$ , which is approximately 100 times smaller than the propagation length. This is an important feature for realizing a number of compact passive waveguide components – such as switches, add-drop multiplexers, etc. However, by decreasing the separation distance, the effective mode index of odd mode goes down closer and closer to the refractive index of substrate. That means the increase of the scattering losses on imperfections for this mode, and eventually, for separation distance smaller than  $1.2 \mu\text{m}$ , odd mode starts to leak to the substrate and therefore it is not supported by the waveguide (so only even mode will survive, resulting in equal output in both waveguides). On the other hand, by increasing the separation between waveguides, one can decrease coupling strength to avoid cross-talk (for example, for the separation of  $5 \mu\text{m}$  the coupling length is almost 10 times larger than the propagation length). Hence, the dependence of the coupling strength on the separation distance can be used to set a limit on maximum integration density of LR-DLSPPW-based components.

A dependence of the coupling strength on the excitation wavelength is an important parameter for the wavelength selective components. Calculations shows that the coupling length is  $\sim 170 \mu\text{m}$  at  $\lambda = 1400 \text{ nm}$ , that is more than twice as long as the coupling length at  $\lambda = 1650 \text{ nm}$  (which is around  $80 \mu\text{m}$ ). However, with the increase of the wavelength the mode effective index of each mode is also going down, so there is a certain cut-off wavelength (approx. at  $1740 \text{ nm}$ ), for which the effective mode index of odd mode reaches the value of the refractive index of the substrate and consequently the mode is no longer coupled to the waveguides. As for the experimental results, a small mismatch with numerical calculations can be explained by a different real geometry of the waveguide (for example, the thickness of metal might be slightly different, and ridge edges might be rounded), as well as by the imperfections of the real waveguide. Overall, a strong dependence on wavelength and separation distance makes LR-DLSPPW very promising for realization of passive and active plasmonic components.

### 3. Conclusion

Overall, we have studied LR-DLSPPW-based DC and its components: single straight waveguides and sine-shaped S-bends, over the wavelength range 1425-1625 nm. It was shown that the near-field optical images depend strongly on the shape and symmetry of the SNOM probe and do not always reflect the actual LR-DLSPPW mode distribution. The experimental observations were explained by the transfer function of the fiber tip [27, 28] and specific LR-DLSPPW mode electric field distribution. However, the average strength of the SNOM signal can still be used to track the propagation of the LR-DLSPPW mode.

Sine-shaped S-bends (having an offset of  $\sim 10 \mu\text{m}$  over a distance of  $\sim 20 \mu\text{m}$ ) have also been investigated experimentally by use of SNOM. Based on experimental data, the total transmission was evaluated to be  $-3.5 \text{ dB}$  at  $\lambda = 1425 \text{ nm}$ , decreasing gradually with the increase of wavelength up to  $-4.2 \text{ dB}$  at  $\lambda = 1525 \text{ nm}$ . Bent waveguides were studied further by applying conformal transformation [29], which allows replacing bent waveguide with an equivalent straight waveguide with exponentially changing refractive index of each medium. By use of FEM we calculated numerically bending losses as a function of bending radius and, eventually, a total transmission through our sine-shaped S-bend, which matched experimental results within the accuracy of measured data.

Finally, we studied LR-DLSPPW-based DCs with a center-to-center waveguides separation of  $2 \mu\text{m}$  over the distance of  $\sim 100 \mu\text{m}$ . The far-field observations showed a strong dependence of DC output on the wavelength and almost complete switch at the wavelength of  $1450 \text{ nm}$ . The near-field experimental measurements showed a strong coupling between waveguides, resulting in coupling length which decreases uniformly from  $\sim 115 \mu\text{m}$  to  $\sim 75 \mu\text{m}$  with the increase of the wavelength from  $1425 \text{ nm}$  to  $1625 \text{ nm}$ .

In addition to experimental study, we performed numerical simulations based on FEM implemented in COMSOL. Calculations showed that, for center-to-center waveguides separation  $d = 2 \mu\text{m}$  and for the excitation wavelength varying from  $1400$  to  $1650 \text{ nm}$ , the coupling length decreases gradually from  $\sim 150 \mu\text{m}$  to  $\sim 80 \mu\text{m}$ . A small mismatch between numerical and experimental results can be explained by a different real geometry of the waveguides (for example, the thickness of metal might be slightly different, and edges might be rounded), as well as by the imperfections of the real waveguides. On the other hand, simulations of DCs at  $\lambda = 1500 \text{ nm}$  for varying separation distance from  $1.2 \mu\text{m}$  to  $5 \mu\text{m}$  showed that the coupling strength can be adjusted vastly: the coupling length increases from  $\sim 20 \mu\text{m}$  (at separation of  $1.2 \mu\text{m}$ ) to  $\sim 20 \text{ mm}$  (at separation of  $5 \mu\text{m}$ ). Combining these features with a relatively large propagation length ( $\sim 2 \text{ mm}$ ) and relatively strong mode confinement, one can conclude that LR-DLSPPWs have a high potential for realization of passive and active plasmonic components.

### Acknowledgments

Very special thanks go out to Xueliang Shi for valuable discussions concerning simulations in COMSOL. The authors also gratefully acknowledge financial support from the Danish Council for Independent Research (FTP-project no. 09-072949 ANAP), support from the University of Iceland Research Fund and the ESF network Plasmon-BioNanoSense.



# Appendix A.4

Nanofocusing in circular sector-like nanoantennas

---

# Nanofocusing in circular sector-like nanoantennas

Vladimir A. Zenin,<sup>1,\*</sup> Anders Pors,<sup>1</sup> Zhanghua Han,<sup>1,2</sup>  
René L. Eriksen,<sup>1</sup> Valentyn S. Volkov,<sup>1</sup> and Sergey I. Bozhevolnyi<sup>1</sup>

<sup>1</sup>*Department of Technology and Innovation, University of Southern Denmark, Niels Bohr Allé 1, DK-5230 Odense, Denmark*

<sup>2</sup>*Center for Terahertz Research, China Jiliang University, Hangzhou 310018, China*

\*[zenin@iti.sdu.dk](mailto:zenin@iti.sdu.dk)

**Abstract:** Gold circular sector-like nanoantennas (with a radius of 500 nm and a taper angle of 60°, 90°, and 120°) on glass are investigated in a near-infrared wavelength range (900 - 2100 nm). Amplitude- and phase-resolved near-field images of circular sector-like antenna modes at telecom wavelength feature a concentric circular line of phase contrast, demonstrating resonant excitation of a standing wave of counter-propagating surface plasmons, travelling between a tip and opposite circular edge of the antenna. Transmission spectra obtained in the range 900 - 2100 nm are in good agreement with numerical simulations, revealing the main feature of this antenna configuration, viz., the resonance wavelength, in contrast to triangular antennas, does not depend on the taper angle and is determined only by the sector radius. This feature together with a robust and easily predictable frequency response makes circular sector-like nanoantennas very promising for implementing bowtie antennas and attractive for many applications.

© 2014 Optical Society of America

**OCIS codes:** (180.4243) Near-field microscopy; (240.6680) Surface plasmons.

## References and links

1. W. Zhang, L. Huang, C. Santschi, and O. J. F. Martin, "Trapping and sensing 10 nm metal nanoparticles using plasmonic dipole antennas," *Nano Lett.* **10**, 1006–1011 (2010).
2. M. L. Juan, M. Righini, and R. Quidant, "Plasmon nano-optical tweezers," *Nature Photonics* **5**, 349–356 (2011).
3. A. Weber-Bargioni, A. Schwartzberg, M. Schmidt, B. Harteneck, D. F. Ogletree, P. J. Schuck, S. Cabrini, "Functional plasmonic antenna scanning probes fabricated by induced-deposition mask lithography," *Nanotechnology* **21**, 065306 (2010).
4. J. N. Farahani, D. W. Pohl, H. J. Eisler, and B. Hecht, "Single quantum dot coupled to a scanning optical antenna: a tunable superemitter," *Phys. Rev. Lett.* **95**, 017402 (2005).
5. H. A. Atwater and A. Polman, "Plasmonics for improved photovoltaic devices," *Nat Mater* **9**, 205–213 (2010).
6. L. Tang, S. E. Kocabas, S. Latif, A. K. Okyay, D. S. Ly-Gagnon, K. C. Saraswat, and D. A. B. Miller, "Nanometre-scale germanium photodetector enhanced by a near-infrared dipole antenna," *Nature Photonics* **2**, 226–229 (2008).
7. J. A. Schuller, E. S. Barnard, W. Cai, Y. C. Jun, J. S. White, and M. L. Brongersma, "Plasmonics for extreme light concentration and manipulation," *Nat Mater* **9**, 193–204 (2010).
8. P. Bharadwaj, B. Deutsch, and L. Novotny, "Optical antennas," *Adv. Opt. Photon.* **1**, 438–483 (2009).
9. L. Novotny and N. F. van Hulst, "Antennas for light," *Nature Photonics* **5**, 83–90 (2011).
10. D. K. Gramotnev and S. I. Bozhevolnyi, "Plasmonics beyond the diffraction limit," *Nature Photonics* **4**, 83–91 (2010).
11. A. Pors, O. Albrektsen, I. P. Radko, and S. I. Bozhevolnyi, "Gap plasmon-based metasurfaces for total control of reflected light," *Sci. Rep.* **3**, 2155 (2013).

12. A. Pors and S. I. Bozhevolnyi, "Plasmonic metasurfaces for efficient phase control in reflection," *Opt. Express* **21**, 27438–27451 (2013).
13. D. P. Fromm, A. Sundaramurthy, P. J. Schuck, G. Kino, and W. E. Moerner, "Gap-dependent optical coupling of single "bowtie" nanoantennas resonant in the visible," *Nano Lett.* **4**, 957–961 (2004).
14. H. Fischer and O. J. F. Martin, "Engineering the optical response of plasmonic nanoantennas," *Opt. Express* **16**, 9144–9154 (2008).
15. D. K. Gramotnev, A. Pors, M. Willatzen, and S. I. Bozhevolnyi, "Gap-plasmon nanoantennas and bowtie resonators," *Phys. Rev. B* **85**, 045434 (2012).
16. L. Novotny, "Effective wavelength scaling for optical antennas," *Phys. Rev. Lett.* **98**, 266802 (2007).
17. T. Søndergaard, J. Beermann, A. Boltasseva, and S. I. Bozhevolnyi, "Slow-plasmon resonant-nanostrip antennas: analysis and demonstration," *Phys. Rev. B* **77**, 115420 (2008).
18. A. Pors, M. Willatzen, O. Albrektsen, and S. I. Bozhevolnyi, "From plasmonic nanoantennas to split-ring resonators: tuning scattering strength," *J. Opt. Soc. Am. B* **27**, 1680–1687 (2010).
19. R. Zia, M. D. Selker, and M. L. Brongersma, "Leaky and bound modes of surface plasmon waveguides," *Phys. Rev. B* **71**, 165431 (2005).
20. M. Schnell, A. Garcia-Etxarri, A. J. Huber, K. B. Crozier, A. Borisov, J. Aizpurua, and R. Hillenbrand, "Amplitude- and phase-resolved near-field mapping of infrared antenna modes by transmission-mode scattering-type near-field microscopy," *J. Phys. Chem. C* **114**, 7341–7345 (2010).
21. N. Ocelic, A. Huber, and R. Hillenbrand, "Pseudoheterodyne detection for background-free near-field spectroscopy," *Appl. Phys. Lett.* **89**, 101124 (2006).
22. A. Garcia-Etxarri, I. Romero, F. J. Garcia de Abajo, R. Hillenbrand, and J. Aizpurua, "Influence of the tip in near-field imaging of nanoparticle plasmonic modes: weak and strong coupling regimes," *Phys. Rev. B* **79**, 125439 (2009).
23. R. Esteban, R. Vogelgesang, J. Dorfmler, A. Dmitriev, C. Rockstuhl, C. Etrich, and K. Kern, "Direct near-field optical imaging of higher order plasmonic resonances," *Nano Lett.* **8**, 3155–3159 (2008).
24. M. Schnell, A. Garcia-Etxarri, A. J. Huber, K. Crozier, J. Aizpurua, and R. Hillenbrand, "Controlling the near-field oscillations of loaded plasmonic nanoantennas," *Nature Photonics* **3**, 287–291 (2009).
25. R. L. Olmon, P. M. Krenz, A. C. Jones, G. D. Boreman, and M. B. Raschke, "Near-field imaging of optical antenna modes in the mid-infrared," *Opt. Express* **16**, 20295–20305 (2008).
26. M. Schnell, P. Alonso-Gonzalez, L. Arzubia, F. Casanova, L. E. Hueso, A. Chuvilin, and R. Hillenbrand, "Nanofocusing of mid-infrared energy with tapered transmission lines," *Nature Photonics* **5**, 283–287 (2011).
27. P. B. Johnson and R. W. Christy, "Optical constants of the noble metals," *Phys. Rev. B* **6**, 4370–4379 (1972).
28. A. V. Zayats, I. I. Smolyaninov, and A. A. Maradudin, "Nano-optics of surface plasmon polaritons," *Phys. Rep.* **408**, 131–314 (2005).
29. T. Søndergaard and S. I. Bozhevolnyi, "Slow-plasmon resonant nanostructures: Scattering and field enhancements," *Phys. Rev. B* **75**, 073402 (2007).
30. K. L. Kelly, E. Coronado, L. L. Zhao, and G. C. Schatz, "The optical properties of metal nanoparticles: the influence of size, shape, and dielectric environment," *J. Phys. Chem. B* **107**, 668–677 (2003).
31. P. Alonso-Gonzalez, P. Albella, F. Neubrech, C. Huck, J. Chen, F. Golmar, F. Casanova, L. E. Hueso, A. Pucci, J. Aizpurua, and R. Hillenbrand, "Experimental verification of the spectral shift between near- and far-field peak intensities of plasmonic infrared nanoantennas," *Phys. Rev. Lett.* **110**, 203902 (2013).

## 1. Introduction

Plasmonic antennas enable a variety of cutting-edge applications such as nanosensors, nanomanipulation and near-field trapping techniques [1, 2], high-resolution probes for nanoimaging and information processing approaches [3, 4], improved photovoltaics [5], nanoscale photodetectors with significantly enhanced signal-to-noise ratio [6, 7], catalysis applications [7], efficient coupling of light energy to nanoscale structures, quantum dots and single molecules [8–10], plasmonic metasurfaces for control of light at the nanoscale [11, 12], etc. Among the vast variety of designs of plasmonic nanoantennas, bowtie antennas are used very often due to the simplicity of fabrication, tunability of the resonance, high localization and electrical field enhancement (FE) [13, 14]. However, the common used triangular shape of bowtie antennas may lead to partial destructive interference of the propagating plasmons, i.e., surface plasmon polaritons (SPPs), due to their different optical paths between bowtie vertex and the points on the opposite edge of the bowtie arm. This in turn leads to a generally reduced FE at the bowtie vertex and comparatively complex frequency response. On the contrary, the circular sector-like shape of nanoantennas is expected to result in the constructive SPP interference and nanofocus-

ing due to the same length of optical paths between the antenna vertex and the opposite circular edge [15]. That allows one to interpret the corresponding plasmonic resonances as being associated with the formation of standing SPPs travelling between the circular edge and vertex of the antenna. These structures should therefore behave similarly to other plasmonic resonators featuring typically a large length-to-width ratio [16-18], with the frequency response being relatively easy to predict and with considerable FE at the antenna vertex.

In this paper we demonstrate proofs of the concept of resonant FE due to standing SPPs in circular sector-like nanoantennas of the insulator-metal-insulator (IMI) configuration. Since SPPs travel synchronously from the antenna edge to its taper, the antenna can be considered as a stripe of variable width. Moreover, if the width of the stripe is much larger than the metal thickness, the mode effective index of SPP propagating on the stripe does not strongly depend on the stripe-width [19]. Therefore, the optical path length of the SPPs should not depend on the taper angle of a relatively thin circular sector-like antenna. Thus, the frequency response should not depend on the taper angle as well. However, this argument does not hold for incident light polarized in the transverse direction of the nanoantenna. Thus, comparing extinction cross-section spectra for antennas with different taper angles illuminated with the incident light of different polarizations, we provide a first proof of the concept. Moreover, the direct comparison of spectra for circular sector-like and triangular antennas with different taper angles indicates advantages of the first design.

Secondly, a standing SPP wave pattern should create a particular distribution of the out-of-plane component of the electric near-field, demonstrating a phase contrast of  $\pi$  rad between the two halves of the antenna, with a line of contrast having a concentric circular shape separating the two sectors. In this work, the near-field amplitude and phase distributions are investigated using a scattering-type scanning near-field optical microscope together with numerical simulations. The simulations for circular sector-like antennas agree well with experimental result, while the simulations for triangular antennas show more complicated phase profile, indicating a complex nature of antenna excitation.

Finally, as mentioned above, a circular shape of the sector-like nanoantenna should provide constructive interference of SPPs converging toward the taper vertex, with FE potentially exceeding those found for triangular-shaped antennas. As SPPs, however, are launched perpendicularly to the nanoantenna edges, circular sector-like antennas may (for linearly polarized light) reduce the SPP excitation efficiency in comparison with triangular antennas, which can limit the overall improvement in FE. In order to compare FE of antennas with both shapes, we study numerically resonant structures at 1500 nm with the emphasis on two different modes of the triangular antenna. Simulations show that one of these modes, which is associated with the SPP propagation along the edges connecting the apex with the other vertices, has FE comparable to the circular sector-like nanoantenna. Nevertheless, similar FE together with easily predicted and controlled frequency response makes circular sector-like antennas preferable to traditional triangular nanoantennas.

## 2. Materials and methods

In this paper we consider gold circular sector-like antennas with radius  $R$ , taper angle  $\alpha$ , and thickness  $t = 50$  nm, placed on a glass substrate [Fig. 1(a)], and compare them with triangular antennas of the same thickness, length  $L$  and taper angle  $\alpha$  [Fig. 1(b)]. We fabricated circular sector-like antennas with  $R = 500$  nm and  $\alpha = 60^\circ$ ,  $90^\circ$ , and  $120^\circ$ , respectively, using electron-beam lithography, metal evaporation and subsequent lift-off. For each taper angle we fabricated an array of  $10 \times 10$  antennas, separated by  $4 \mu\text{m}$ , and investigated them in a near infrared (NIR) range of wavelengths from 900 to 2100 nm. The substrate was made of BK7 glass, which has a refractive index of  $n \simeq 1.5$  for the considered NIR range.

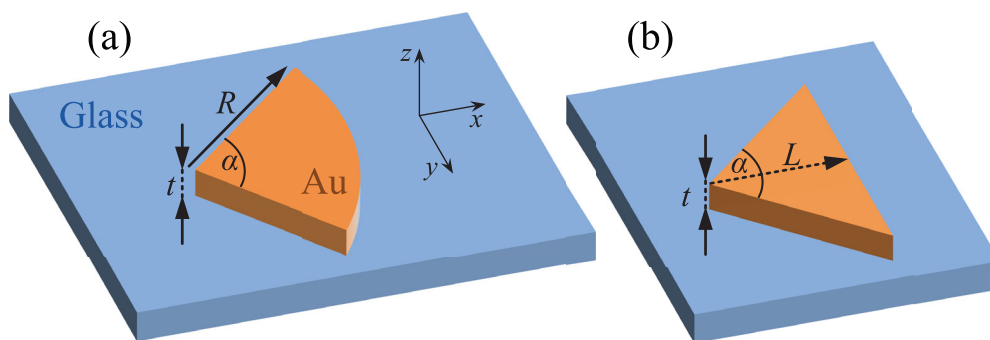


Fig. 1. Design of the (a) circular sector-like plasmonic antenna and (b) triangular antenna.

The transmission spectra of the fabricated nanoantennas were measured in an optical microscope (Olympus BX 51) where the light was sent at near normal incidence from the substrate side upwards through the sample and collected from the top using an objective with a magnification of  $\times 100$  and a numerical aperture (NA) of 0.9 and analyzed in a fiber-coupled spectrometer (NIRQuest512, Ocean Optics). The light was polarized in either  $x$ - or  $y$ -direction, and the diameter of the illumination spot was around  $35 \mu\text{m}$ .

Phase- and amplitude-resolved near-field investigation of nanoantennas was done using a scattering-type scanning near-field optical microscope (s-SNOM), based on an atomic force microscope (AFM), that uses cantilevered tips as near-field probes (NeaSNOM from Neaspec GmbH). In our experiments we used standard commercial Si tips covered with platinum (Arrow NCPt, NanoWorld). The sample was scanned in a tapping mode, with the tip oscillating at the mechanical resonance frequency  $\Omega \approx 250 \text{ kHz}$  with an amplitude  $\sim 50 \text{ nm}$ . The structures were illuminated from the bottom (transmission-mode, [20]) with focused light at  $\lambda = 1500 \text{ nm}$  (the illumination spot diameter was around  $3 \mu\text{m}$ ). The light, scattered by the tip, was collected by a parabolic mirror and directed towards the detector, where it was overlapped with an interfering reference beam, yielding both the amplitude and the phase of the scattered light using pseudoheterodyne detection [21]. Background contributions were suppressed by demodulating the detector signal at a high harmonic frequency  $n\Omega$  (in our case  $n = 2$ ), providing background-free near-field amplitude and phase images. It should be pointed out that in most s-SNOM experiments the illumination is done in reflection-mode, where the light is focused on the tip with the same parabolic mirror that collects scattered light. This configuration creates many problems observing clear antenna modes and treatment of data due to a strong tip-sample coupling [22] and phase-retardation effects [23]. However, in our transmission-mode configuration the sample was illuminated from below, with an in-plane direction of polarization. Therefore we achieved homogeneous illumination and efficient excitation of the antenna and avoided direct excitation of the tip [20, 24]. Due to a dominating dipole moment of a tip along its axis (i.e., along  $z$ -axis), the recorded s-SNOM images represents mostly a distribution of the amplitude and phase of the  $z$ -component of the electric field,  $E_z$  [25, 26]. In order to enhance this selectivity, a polarizer at the detector was set correspondently to  $z$ -polarization of the light, scattered by the tip. Finally, the recorded data were imaged with free scanning probe microscopy software Gwyddion.

The transmission spectra and field distribution were simulated using the finite-element approach in the commercially available software package COMSOL MULTIPHYSICS. The values for the gold permittivity at different incident wavelengths are taken from [27]. The considered three-dimensional structures were illuminated from the bottom using a monochromatic plane wave, linearly polarized along either  $x$ - or  $y$ -axis. For all geometrical configurations, the

simulation domain was truncated using perfectly matched layers on the top and bottom facets in order to suppress artificial scattering from the truncation boundaries. On the other facets, separated by  $4\ \mu\text{m}$ , periodic boundary conditions were applied to simulate the array of structures. All sharp edges of antennas were rounded to  $10\ \text{nm}$  in order to avoid singular fields and to reduce the lightning rod effect [28].

### 3. Results and discussion

#### 3.1. Extinction cross section

The transmission spectra for three arrays of circular sector-like antennas with taper angle of  $\alpha = 60^\circ$ ,  $90^\circ$ , and  $120^\circ$ , respectively, were investigated with the incident light being polarized in either  $x$ - or  $y$ -direction. In order to emphasize wavelength-dependent features, an extinction cross section  $\sigma_{\text{ext}}$  was calculated as follows:

$$\sigma_{\text{ext}} = A(1 - T), \quad (1)$$

where  $A$  is a  $4 \times 4\ \mu\text{m}^2$  unit area and  $T$  is the transmission. The results for  $x$ -polarization show similar frequency response for all three taper angles, with the resonance being at  $\lambda \sim 1500\ \text{nm}$  for all configurations [Fig. 2(a)]. On the contrary, the results for  $y$ -polarization show strong dependence on the taper angle in the frequency response. Therefore, one can conclude, that for  $x$ -polarization the effective resonator length is virtually not changing with the increase of taper angle, but increases considerably for  $y$ -polarization, where the position of the resonance moves substantially (for  $\alpha = 90^\circ$  it is at  $\lambda \sim 1900\ \text{nm}$ , and for  $\alpha = 120^\circ$  it is even beyond the measurement range). For a particular taper angle of  $60^\circ$  the extinction spectra for  $x$ - and  $y$ -polarization look almost the same, which is expected for the structure with a shape close to an equilateral triangle.

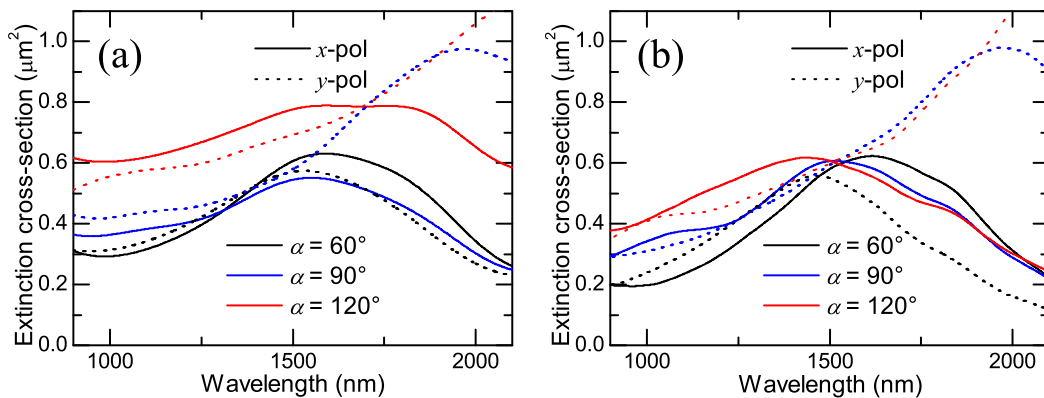


Fig. 2. (a) Experimental and (b) numerically calculated extinction cross section of  $x$ - (solid lines) and  $y$ -polarized light (dotted lines) for circular sector-like antennas with different taper angle:  $\alpha = 60^\circ$  (black),  $90^\circ$  (blue), and  $120^\circ$  (red). The radius is the same,  $R = 500\ \text{nm}$ .

The numerical simulations of transmission spectra and corresponding extinction cross sections [Fig. 2(b)] show a good agreement with the experimental results [Fig. 2(a)], and all features discussed above are still preserved: the position of the resonance is at  $\lambda \sim 1500\ \text{nm}$  and do not move much for  $x$ -polarization (compared with  $y$ -polarization) with the change of taper angle. The small variations of the resonance wavelength with the increase of the taper angle can be explained by the fact that SPPs are not excited uniformly on the circular edge, while

also being generated on the radial edges, hence leading to a frequency response that is not completely angle independent. Another explanation can be that a short part of the antenna near taper, being considered as a stripe, has a relatively small width, therefore the effective mode index of supported SPP is larger than the one for wide stripe, causing a red shift for the resonance wavelength of antennas with smaller taper angles. Also the phase shift acquired upon reflection of the SPP at the taper and the edge of antenna [29] might depend on the taper angle. As for the differences with experimental results, such as the level of average extinction, they can be attributed to the imperfections of fabricated structure. Noticeable red shift and an increased extinction cross-section for the measurements of 120-degree antennas we explain by a slightly larger radius, which will be supported later by topographical images of structures.

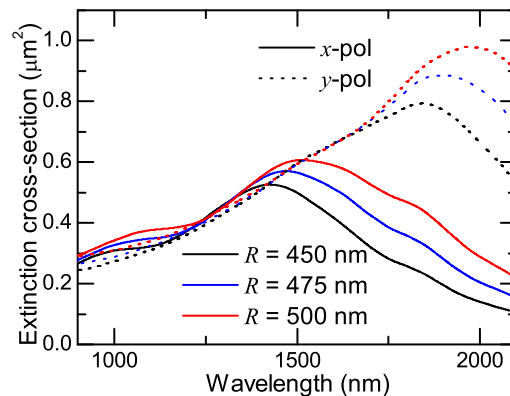


Fig. 3. Numerically calculated extinction cross section of  $x$ - (solid lines) and  $y$ -polarized light (dotted lines) for circular sector-like antennas with different radius:  $R = 450$  nm (black),  $475$  nm (blue), and  $500$  nm (red). The taper angle is the same,  $\alpha = 90^\circ$ .

The numerical simulations were also conducted for different radii of the structures, keeping the taper angle fixed at  $\alpha = 90^\circ$  [Fig. 3]. The results show a well predicted behavior of the frequency response: with the increase of radius  $R$  the resonator length increases, increasing the resonance SPP wavelength (which should fit into the resonator), therefore the resonance wavelength is also increasing. The average extinction cross section increases with the increase of the radius  $R$ , which is expected, since both scattering and absorption cross section increases.

### 3.2. Near-field investigations

Near-field imaging of the SPP modes of circular sector-like antennas was performed with an s-SNOM at  $\lambda = 1500$  nm wavelength with either  $x$ - or  $y$ -polarized light incident from the bottom. Due to the pseudoheterodyne detection we managed to obtain both background free amplitude and phase of the out-of-plane electric near-field component,  $E_z$  [Figs. 4(a) and (c)]. Numerical simulations of the  $E_z$  field distribution at a distance of 5 nm above the structure correspond well with the experimental measurements [Fig. 4(b)]. One can see that for  $x$ -polarized incident light (the polarization is shown with arrows) the amplitude images show two local maxima: a hot spot at the vertex of antenna and much weaker and broader spot at the opposite edge of antenna. Due to imperfections and larger taper rounding in fabricated structure, the measured hot spot in the vertex of antenna is weaker in localization, compared to the simulation results. Also the phase measurements show some distinctions from the simulation outside the structure [the borders of the structure are shown with black lines in Fig. 4(b)], which can be explained by the residual background and tip-sample interaction presented in the experiment. Please note that only simulation results were normalized to the same color bar representing field amplitudes,

since the setup was readjusted each time before the measurement without calibration.

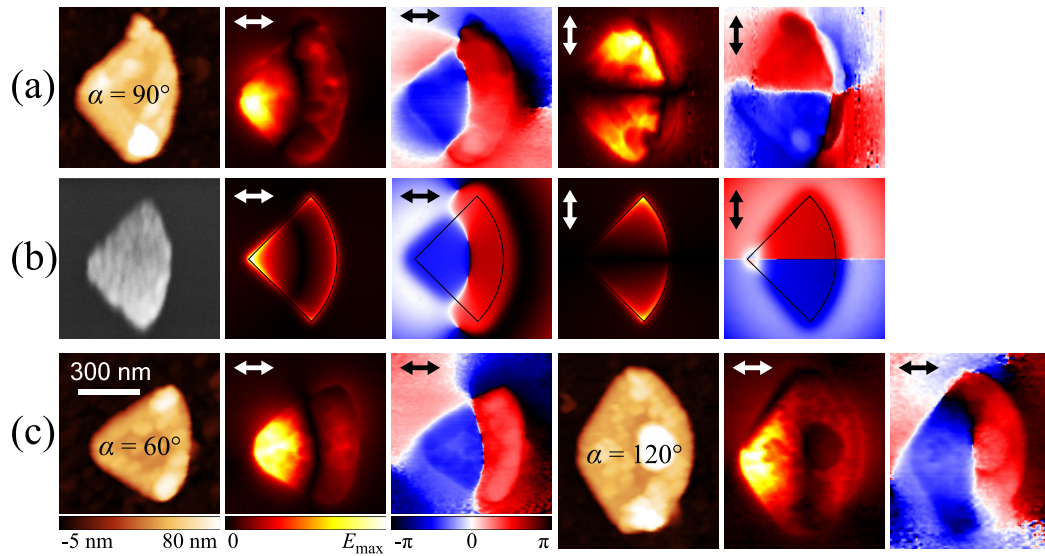


Fig. 4. (a) Pseudocolor s-SNOM images for the circular sector-like antenna with  $R = 500$  nm and  $\alpha = 90^\circ$  at  $\lambda = 1500$  nm, showing (from left to right) topography, optical amplitude and phase for  $x$ - and  $y$ -polarized incident light. (b) Scanning electron microscope (SEM) image of the same structure as in (a), and numerically calculated distributions of  $E_z$  amplitude and phase for  $x$ - and  $y$ -polarized incident light for the same structure. (c) Pseudocolor s-SNOM images of topography, optical amplitude and phase for the antennas with  $R = 500$  nm and  $\alpha = 60^\circ$  and  $120^\circ$  at  $\lambda = 1500$  nm. Linear color bars for topography and optical amplitude, as well as a periodic color bar for the optical phase images are shown. Polarization is shown with arrows.

Phase images for  $x$ -polarization show two distinctive antenna parts, each having almost a constant phase, while the phase difference between the two parts is  $\pi$  rad (note that a color bar for the phase images is periodic and shown at the bottom in Fig. 4), which is a clear indication of a standing wave. Moreover, the line of contrast between these two parts has a concentric circular shape, proving the idea of a standing wave of SPP, travelling between the edge and the vertex of the antenna. Such a split of the field distribution into two opposite parts was observed for all structures (however, the structure with  $\alpha = 120^\circ$  has a weaker contrast). As was assumed before, the 120-degree antenna has slightly larger radius, which can also explain the weak phase contrast (since the antenna is not resonantly excited). The images for  $y$ -polarization show the usual dipole excitation, with the middle horizontal line of phase contrast (due to symmetry of the structure).

### 3.3. Comparison with triangular antennas

The usage of circular sector-like antennas is motivated by rather erratic frequency responses observed for triangular antennas when geometrical parameters are varied [14]. At the same time, as also mentioned in [15], the equal length between the circular-shaped edge and the vertex improves the resonant SPP nanofocusing, potentially leading to higher resonant FE as compared to triangular antennas. In this section, we numerically compare FE at the vertex of our nominal circular sector-like nanoantenna ( $R = 500$  nm,  $\alpha = 90^\circ$ ) with those for two differently-sized triangular antennas, each having a resonance at  $\lambda = 1500$  nm. The two triangular antennas have the lengths  $L = 375$  nm and  $L = 610$  nm, respectively, and their extinction cross-sections for



$x$ -polarized incident light and different taper angles are shown in Fig. 5(a). It is clearly seen that the spectral response strongly depends on the taper angle, with the largest triangular antenna ( $L = 610$  nm,  $\alpha = 120^\circ$ ) demonstrating a multitude of modes in the displayed spectral range. Both triangular antennas show a peak in the extinction at  $\lambda \sim 1500$  nm for the taper angle  $\alpha = 90^\circ$ , and the field distributions of the corresponding modes are presented in Fig. 6 together with the mode of the circular sector-like antenna. It is seen that neither of the two modes of the triangular antennas feature the standing wave pattern extending over the whole antenna area (as is the case with the circular sector-like antenna mode). The mode of the small triangular antenna is related to the standing waves formed along the radial edges, creating thereby an inhomogeneous phase profile [Fig. 6(b)], that albeit somewhat resembles that of the circular sector-like antenna, resulting at the same time in strong FE at all vertices [Fig. 6(a)]. The mode of the large triangular antenna, on the other hand, represents a standing-wave resonance concentrated along the  $x$ -direction, as clearly seen in the phase profile in Fig. 6(b), which is (similar to the mode of the circular sector-like antenna) characterized by increased FE at the taper vertex [Fig. 6(a)].

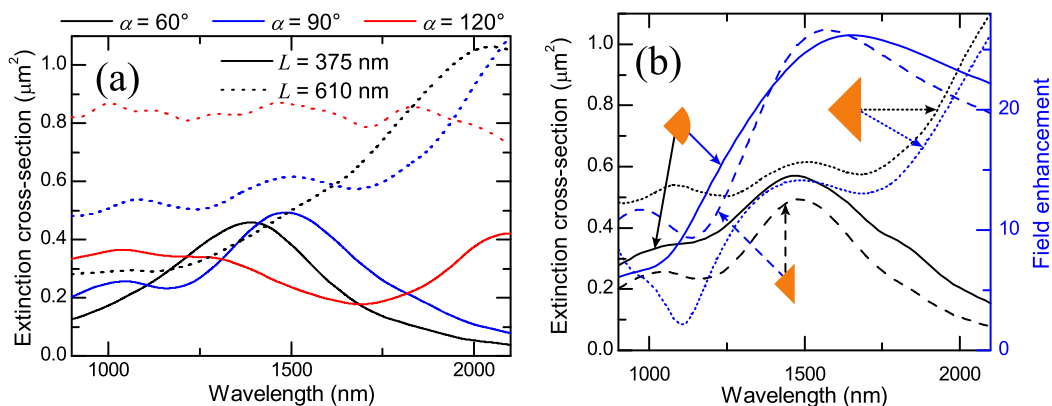


Fig. 5. (a) Numerically calculated extinction cross section of  $x$ -polarized light for small ( $L = 375$  nm, solid lines) and large ( $L = 610$  nm, dotted lines) triangular antennas with different taper angle:  $\alpha = 60^\circ$  (black),  $90^\circ$  (blue), and  $120^\circ$  (red). (b) Comparison of circular sector-like antennas ( $R = 500$  nm, solid lines) with small ( $L = 375$  nm, dashed lines) and large ( $L = 610$  nm, dotted lines) triangular antennas in terms of extinction cross-section (black) and field enhancement (blue).

The FE properties of the three antennas in Fig. 6 are presented in Fig. 5(b) (together with a comparison of their respective extinction cross-sections), with the FE being measured 1 nm away from the taper vertex as indicated by a green arrow in Fig. 6(c). First, it should be noted that the general redshift of the peaks in the FE (i.e., near field) spectra as compared to the extinction spectra is due to depolarization of the plasmonic mode and expected to be found for any nanoantennas with sizes not vanishingly small with respect to the wavelength [30, 31]. Secondly, it is seen that the two competing processes of efficient nanofocusing and reduced excitation efficiency of SPPs for circular sector-like antennas result in similar achievable FE levels for the two types of antennas, with the FE of the triangular antenna being strongly dependent on the choice of the resonant mode. As such, the circular sector-like nanoantenna with an easily predictable and controlled frequency response seems attractive compared to conventional triangular antennas.

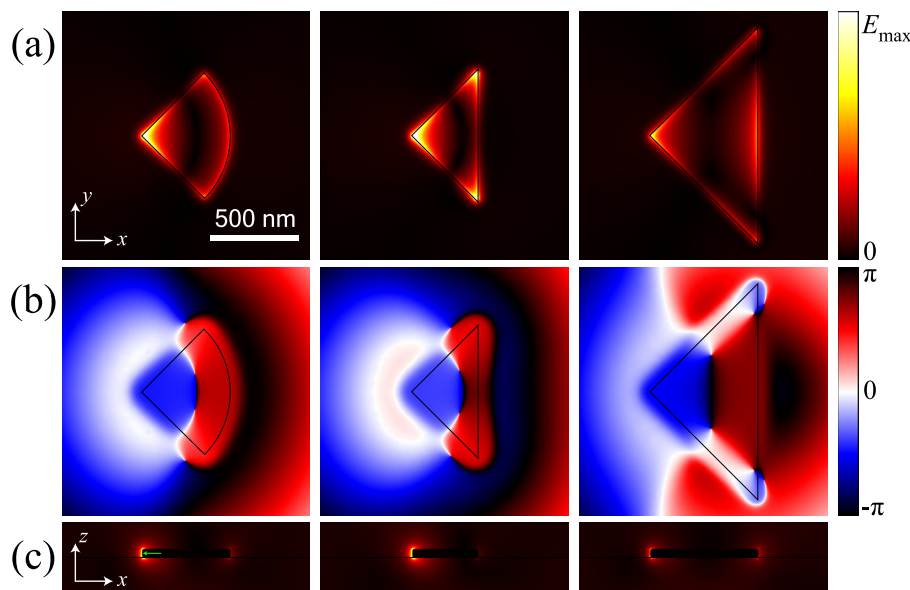


Fig. 6.  $E_z$  amplitude (a) and phase (b) of circular sector-like antennas ( $R = 500$  nm, left), small ( $L = 375$  nm, middle) and large ( $L = 610$  nm, right) triangular antennas, numerically calculated at 5 nm above structures for  $x$ -polarized incident light at  $\lambda = 1500$  nm. (c) Distributions of total field amplitude for the same types of antennas, calculated in  $x$ - $z$  cross-section. The green arrow indicates the point used for evaluation of FE for Fig. 5(b). The top level of amplitude color bar,  $E_{\max}$ , corresponds to FE of 10 for (a) and 30 for (c)

#### 4. Conclusions

Motivated by irregular frequency responses of triangular nanoantennas with respect to changes in geometrical parameters, we have investigated circular sector-like gold nanoantennas on a glass substrate (IMI configuration) in the NIR range. It was expected that this antenna shape would lead to the constructive SPP interference at the taper of the antenna, since the SPPs excited at the antenna circular edge will have the same length of optical path to the antenna vertex, and thereby result in a more robust and predictable frequency response as well as potentially larger FE at the antenna vertex. The circular sector-like nanoantennas, described by a radius  $R$  and taper angle  $\alpha$ , have been studied both experimentally and numerically, revealing that for light polarization along the antenna symmetry axis the extinction spectra only weakly depend on  $\alpha$  from  $60^\circ$  to  $120^\circ$  with well-predictable behavior for changes in the sector radius. On the contrary, the extinction spectra for the opposite polarization, in which the antenna resembles a triangular antenna, varied substantially with respect to the taper angle.

Furthermore, the standing wave pattern of SPPs, travelling between the antenna taper and its circular edge, was expected to create a particular distribution of the out-of-plane electric near-field component, featuring a phase jump between two (almost) constant phase levels, having a phase difference of  $\pi$  rad, and bounded by a line of concentric circular shape. Such field distributions have indeed been found both experimentally and numerically for different taper angles, proving the formation of standing SPP wave.

Finally, we numerically compared the field enhancement properties of circular sector-like nanoantennas and conventional triangular antennas. Despite the nanofocusing ability of the former antenna due to standing SPPs, the circular shape simultaneously reduces the overall SPP excitation efficiency for linearly polarized light, ultimately resulting in similar levels of FE

for the two types of antennas.

We believe that the presented analysis and results obtained demonstrate convincingly that usage of the circular sector-like shape instead of triangular shape for individual antennas and their combinations (like bowtie antennas) is preferential due to more robust and easily predicted frequency responses of these nanoantennas that preserve the same attractive FE properties.

### **Acknowledgments**

The authors thank Alexander S. Roberts and Ashwani Kumar (SDU) for having performed the SEM measurements and acknowledge support for this work from the Danish Council for Independent Research (the FTP project ANAP, Contract No. 09-072949). Z. Han also acknowledges the support from National Natural Science Foundation of China (grant 61107042).



# Appendix A.5

Plasmonic slot waveguides and nanocouplers

---

## Direct Characterization of Plasmonic Slot Waveguides and Nanocouplers

Andrei Andryieuski,<sup>\*,†</sup> Vladimir A. Zenin,<sup>\*,‡</sup> Radu Malureanu,<sup>†</sup> Valentyn S. Volkov,<sup>‡</sup> Sergey I. Bozhevolnyi,<sup>‡</sup> and Andrei V. Lavrinenko<sup>†</sup>

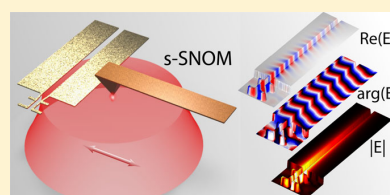
<sup>†</sup>DTU Fotonik, Technical University of Denmark, Oersteds pl. 343, Kongens Lyngby DK-2800, Denmark

<sup>‡</sup>Department of Technology and Innovation, University of Southern Denmark, Niels Bohrs Allé 1, Odense M DK-5230, Denmark

### S Supporting Information

**ABSTRACT:** We demonstrate the use of amplitude- and phase-resolved near-field mapping for direct characterization of plasmonic slot waveguide mode propagation and excitation with nanocouplers in the telecom wavelength range. We measure mode's propagation length, effective index and field distribution and directly evaluate the relative coupling efficiencies for various couplers configurations. We report 26- and 15-fold improvements in the coupling efficiency with two serially connected dipole and modified bow-tie antennas, respectively, as compared to that of the short-circuited waveguide termination.

**KEYWORDS:** Nanocoupler, surface plasmon, slot waveguide, nanoantenna, s-SNOM, near-field microscopy



Great advantages offered by plasmonics to optical waveguiding are extreme subwavelength localization of guided modes close to the metal interface<sup>1</sup> together with electrical tunability of electromagnetic waves via intrinsic metallic contacts.<sup>2</sup> Plasmonic waveguides are therefore considered as a future generation of optical interconnects in integrated circuits for datacom technologies.<sup>3</sup> Inevitably, with the appearance of nanoscale waveguides a new challenge has emerged: how to effectively couple the diffraction-limited optical waves into deep-subwavelength plasmonic waveguides. Various approaches have been utilized ranging from lenses to grating couplers.<sup>4</sup> However, the most compact solution is an antenna-based nanocoupler.

Antenna is a common tool to capture free-space propagating radio-waves with more than a century-long history.<sup>5</sup> Employment of metal-based antennas in photonics started only in the last two decades owing to the progress in high-resolution nanofabrication techniques.<sup>6,7</sup> Usage of plasmonic antennas<sup>8</sup> to couple light to plasmonic waveguides has been suggested theoretically<sup>9–15</sup> and then confirmed experimentally with cross-polarization microscopy measurements in the near-infrared<sup>16</sup> and with near-field microscopy in optical,<sup>17</sup> telecom,<sup>18</sup> and mid-infrared<sup>19</sup> ranges. Nevertheless, the amplitude- and phase-resolved measurements of the antenna-excited slot plasmons in the telecom range (with the free-space wavelength around 1.55  $\mu\text{m}$ ) have not been reported so far. It should be emphasized that the usage of phase-resolved near-field mapping is indispensable for direct characterization of the mode effective index as well as for revealing the symmetry of excited plasmonic modes.<sup>19</sup>

In this Letter, we report for the first time to our knowledge the amplitude- and phase-resolved near-field characterization of plasmonic slot waveguides and antenna-based nanocouplers in the telecom wavelength range. Illumination with a wide laser

beam excites both slot plasmons confined within a dielectric gap in a metal film and surface plasmon polaritons (SPP) propagating along the metal film interface perpendicular to the slot, and the resulting near-field interference pattern is mapped with a scattering-type scanning near-field optical microscope (s-SNOM). The observed interference pattern undergoes then the special filtration procedure in order to extract individual characteristics of the slot mode, including the effective index and propagation length, and its relative excitation efficiency, which is determined as a ratio between the slot mode intensity at the waveguide input and the average SPP intensity. Experimental characterization of two serial dipole and modified bow-tie antennas as well as the short-circuited waveguide termination in the absence of any coupling device is related to modeling of these configurations, including calculations of propagating mode fields and effective areas.

We use a plasmonic slot waveguide<sup>20</sup> (also known as a gap or channel waveguide), representing a rectangular slot of width  $W_{\text{WG}} = 300$  nm carved in a gold film of thickness  $H = 50$  nm. Such a waveguide features both reasonably good mode confinement and propagation length. In a symmetric dielectric environment, the propagation length can reach few tens of micrometers at telecom wavelengths. We, however, select an asymmetric configuration (Figure 1a, inset) that allows one to directly map plasmonic mode-field distributions with a sharp probe tip of the s-SNOM. The drawback of such a configuration is the energy leakage from the slot mode to the slow SPPs on the silica–gold interface (the effective index of the latter is larger than that of the former). The leakage losses

**Received:** April 1, 2014

**Revised:** May 28, 2014

**Published:** June 2, 2014

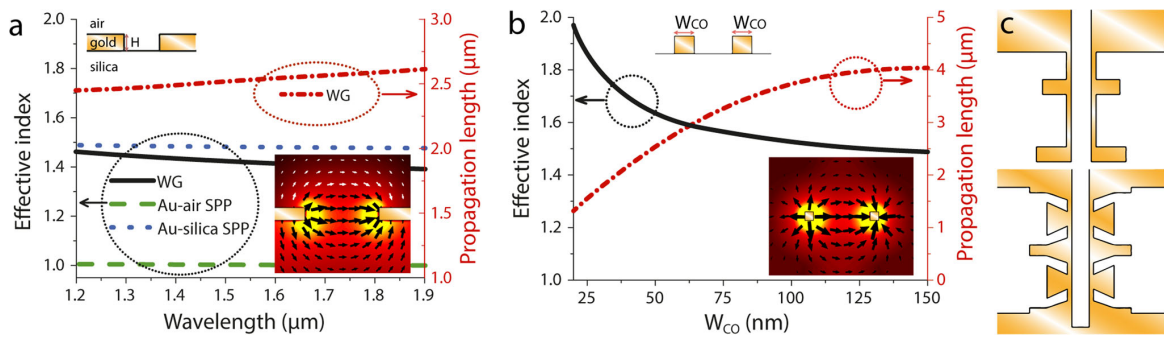


**Figure 1.** (a) Effective indices of the slot waveguide mode (black solid line), gold–air (green dashed) and gold–silica (blue dotted) SPPs together with the propagation length of the slot mode (red dashed-dotted). (b) Effective index (black) and propagation length (red dashed-dotted) of the transmission line waveguide mode depending on the wire width  $W_{CO}$ . Two serially connected (c) dipole and (d) modified bow-tie antennas. Insets in (a) and (b) show cross sections of the correspondent waveguides geometry and total electric field magnitude distributions of the plasmonic modes.

add up to the ohmic losses in the plasmonic waveguide, resulting in the propagation length of  $\sim 2.5 \mu\text{m}$  (Figure 1a). However, simulations indicate that it is sufficient to fill the slot space and add an additional 50 nm thick layer of silica on top in order to eliminate the leakage losses and increase the propagation length up to  $\sim 7 \mu\text{m}$ . For comparison, the propagation lengths of the air–gold and silica–gold SPPs are 230 and 63  $\mu\text{m}$ , respectively, at the wavelength 1.55  $\mu\text{m}$ .

In our previous work,<sup>9</sup> we showed that the serial connection of the antennas provides no benefits for the slot excitation with the tightly focused Gaussian beam, whereas it is an opposite case for the incident plane wave or wide Gaussian beam used in our experimental setup. It is, therefore, important to ensure the optimal connection between the nanoantennas to deliver maximum of the incident energy to the waveguide. The effective index and propagation length of the double-wire transmission line depends on the wire width  $W_{CO}$  (Figure 1b). Smaller losses correspond to wider wires, but wide wires connected to the antenna would prohibit efficient plasmons excitation. It is therefore better to increase the width of the connecting wires in the regions between the antennas, while keeping them narrow otherwise. In order to check the advantage of wider wires we compare thin-wire-connected dipole antennas (Figure 1c) with modified bow-tie antennas that feature widened wire sections between them (Figure 1d). To prevent the wide regions from out-of-phase plasmons excitation, we tune the length of the wide sections out of the resonance.

Numerical simulation and optimization of the nanocouplers for operation at the wavelength of 1.55  $\mu\text{m}$  (see Supporting Information for details) was carried out in CST Microwave Studio.<sup>21</sup> For the plane wave excitation (normal to the substrate in our case), the figure-of-merit of the antenna, which characterizes its coupling efficiency and which is used as an objective function during optimization, is its effective area defined as the ratio of the power delivered to a waveguide mode to the incident power flux  $A_{\text{eff}} = P_{\text{WG}}/S_{\text{inc}}$ . The effective area of one (1DA), two (2DA), and three (3DA) dipole antenna couplers was calculated and found being considerably and progressively larger than that of the open circuit waveguide termination (0DA) (Figure 2, Table 1). At the same time, the operation full width at half-maximum (fwhm) bandwidth of the 3DA coupler is smaller than that of the 2DA one. This fact agrees with the usual trade-off between antenna efficiency and bandwidth. The advantage of larger plasmon propagation

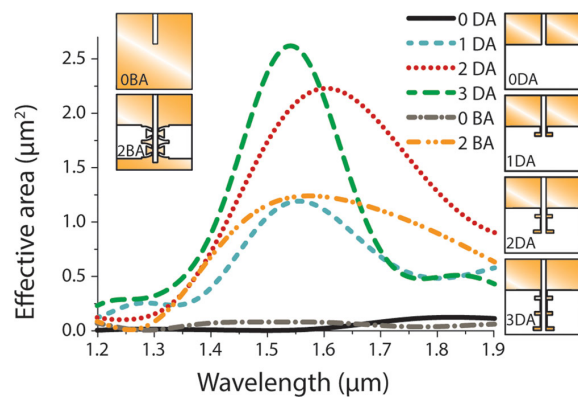


**Figure 2.** Effective area of open circuit waveguide (0DA, black solid), one (1DA, cyan short-dashed), two (2DA, red dotted), and three (3DA, green long-dashed) serial dipoles, short-circuited waveguide (0BA, gray dashed-dotted) and two serial modified bow-tie (2BA, orange dashed-double-dotted) antennas. It is seen that the effective area  $A_{\text{eff}}$  increases with the number of antennas. The values  $A_{\text{eff}}$  at the wavelength of 1.55  $\mu\text{m}$  are collected in Table 1.

**Table 1.** Bandwidth of the Nanocouplers and Their Effective Area at the Optimization Wavelength 1.55  $\mu\text{m}$

design	$A_{\text{eff}} (\mu\text{m}^2)$	bandwidth ( $\mu\text{m}$ )
0 DA	0.0070	
1 DA	1.19	0.30
2 DA	2.09	0.39
3 DA	2.61	0.22
0 BA	0.081	0.38
2 BA	1.23	0.62

length in wider connecting wires does not compensate for worse plasmon excitation due to interaction of metallic bars with the antenna elements and their detuning as well as counter-phase slot plasmons excitation in the modified bow-tie (2BA) antennas, resulting in  $\sim 1.7$  times smaller effective area, but  $\sim 1.5$  times larger bandwidth with respect to that of 2DA. The short-circuited waveguide termination (0BA) was found to be significantly more (by 1 order of magnitude) efficient for slot plasmon excitation than the 0DA configuration. Such a large difference in the coupling efficiencies can be explained by the difference in the corresponding excitation channels; in the OBA

case, the waveguide mode is excited by directional light scattering from a metallic edge extending over the whole waveguide width, whereas in the ODA case it is only excited by scattering off metallic corners with most of scattered light propagating away from the waveguide entrance. Bearing this in mind, we selected the OBA configuration for the experimental fabrication and characterization together with the 2BA and 2DA cases that promise, respectively, 15- and 26-fold improvements in the effective area  $A_{\text{eff}}$  at the wavelength 1.55  $\mu\text{m}$  (Table 1).

The nanocouplers were fabricated using standard electron-beam (e-beam) lithography followed by metal e-beam evaporation and lift-off in acetone (see Supporting Information for details).

Phase- and amplitude-resolved near-field characterization of the plasmonic antenna nanocouplers was carried out using the s-SNOM configuration, based on an atomic force microscope (AFM) with cantilevered tips being employed as near-field probes (NeaSNOM from Neaspec GmbH) (Figure 3). In our

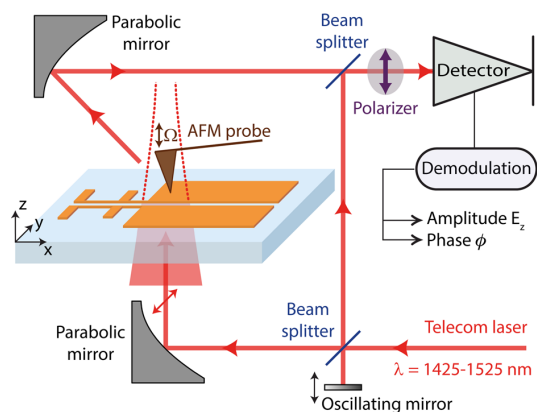


**Figure 3.** Schematic of amplitude and phase near-field mapping with the transmission s-SNOM setup. The sample is illuminated from below with a defocused laser beam (fwhm  $\sim 12 \mu\text{m}$ ) polarized parallel to the dipole antenna. The AFM metal-covered silicon tip scatters the near field (predominantly its vertical component), and the scattered radiation (being collected by the top parabolic mirror) is then mixed with the reference beam and interferometrically detected, yielding amplitude and phase near-field distributions by scanning the sample.

experiments, we used standard commercial Si tips covered with platinum (Arrow NCPt, NanoWorld). The AFM was operated in the tapping mode with the tip oscillating at the mechanical

resonance frequency  $\Omega \approx 250 \text{ kHz}$  with the amplitude of  $\sim 50 \text{ nm}$ . Near-field and topography mapping was performed by moving the sample across the aligned configuration of the oscillating tip and the illumination system. Therefore, in order to continuously excite the antenna we illuminated the structures from below (transmission-mode s-SNOM<sup>22</sup>) with a defocused polarized laser beam (the estimated fwhm illumination spot was  $\sim 12 \mu\text{m}$ ). The light, scattered by the tip, was collected by a top parabolic mirror and directed toward a detector, where it was spatially overlapped with an interfering reference beam, yielding both the amplitude and phase of the scattered light via pseudoheterodyne detection.<sup>23</sup> Background contributions were suppressed by demodulating the detector signal at a high-order harmonic frequency  $n\Omega$  (in our case  $n = 2$ ), providing background-free near-field amplitude and phase images. It should be pointed out that in most s-SNOM experiments the illumination is done in the reflection mode (side-illumination scheme), where the incident light is focused on the tip with the same parabolic mirror that collects scattered light, a configuration that creates many problems for obtaining clear near-field images due to strong tip-sample coupling<sup>24</sup> and phase-retardation effects.<sup>25</sup> However, in our transmission-mode configuration the sample was illuminated from below with an in-plane direction of polarization, allowing us to achieve uniform illumination and efficient excitation of the plasmonic antenna while avoiding the direct tip excitation.<sup>22,25,26</sup> Because of a dominating dipole moment of the tip along its axis (i.e., along the  $z$ -axis), the recorded s-SNOM images represent mostly a distribution of the amplitude and phase of the  $z$ -component of the electric field,  $E_z$ .<sup>25</sup> In order to enhance this selectivity, a polarizer in front of the detector was set to select the out-of-plane  $z$ -polarization of light scattered by the tip. Finally, the recorded data were treated with free (scanning probe microscopy) software Gwyddion.<sup>27</sup>

The recorded optical amplitude and phase images (Figure 4b,c) exhibit a complex interference pattern, produced mainly by the slot waveguide mode and SPPs. The latter are excited with the incident wave being diffracted on the slot, and propagate away from and perpendicular to the slot waveguide. Because of the large (defocused) excitation laser spot, adjusted with the AFM tip during the scan, the SPP amplitude and phase do not significantly change along the waveguide, as opposed to those of the slot mode. One can therefore decompose the recorded near-field data (Figure 4b–d) in the half-space containing the waveguide into the SPP background (Figure 4e–g) and slot mode (Figure 4h–j) fields by fitting the data along the waveguide as a sum of propagating mode and a constant background (see Supporting Information for details).

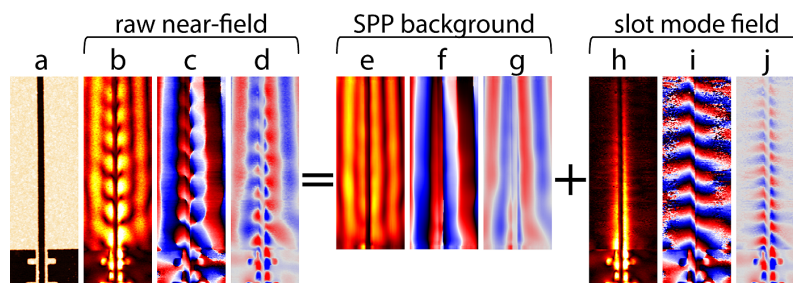


**Figure 4.** Pseudocolor s-SNOM images, representing (a) topography, (b) amplitude, (c) phase, and (d) real part of the raw optical near-field distribution. Amplitude, phase, and real part of the decomposed contributions of (e–g) SPP background and (h–j) slot mode fields.



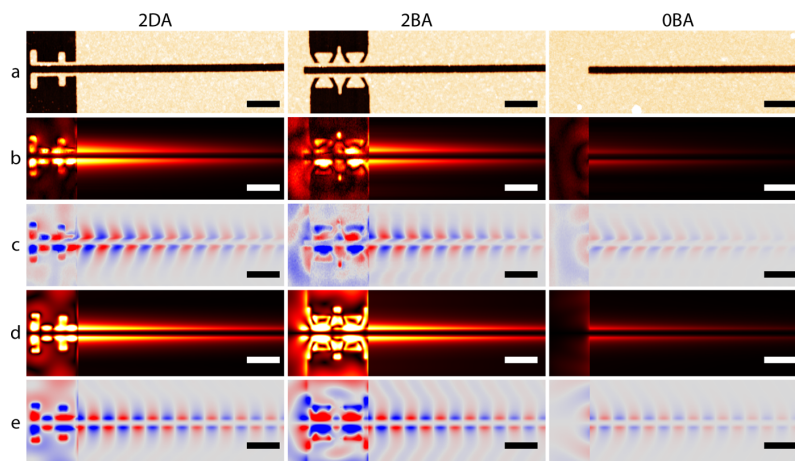


**Figure 5.** Pseudocolor *s*-SNOM images, representing (a) topography, filtered (b) amplitude, and (c) real part of measured near-field data, and filtered (d) amplitude and (e) real part of simulated field for all three types of nanocouplers: 2DA (left), 2BA (middle), and OBA (right). Electric field of the slot mode is normalized to the average amplitude of the background SPP. The scale bar is equal to 1  $\mu\text{m}$ .

Thus, filtered images reveal the propagating slot mode with the decreasing amplitude (Figure 4h) and linearly advancing phase (Figure 4i) of  $E_z$  field. As expected from the mode-field distribution (Figure 1a, inset),  $E_z$  field magnitude is zero in the middle and opposite in sign on both sides of the waveguide (Figure 4j).

The filtering procedure was applied to all measurements (see Supporting Information for more details) made in the telecom range (1425–1525 nm) and to all three types of antenna nanocouplers: 2DA, 2BA, and OBA (Figure 5b,c). Numerically simulated  $E_z$  field distribution at the height of 50 nm above the structure (the average position of the *s*-SNOM tip) was filtered with the same procedure (Figure 5d,e), signifying very reasonable agreement with the experimental results. We should mention that phase images not only allow observing slot plasmon phase evolution but also reveal information on the impedance matching of the antennas to the waveguide.

The filtered images of the slot mode allowed us to estimate the effective mode index, propagation length and intensity of the slot mode at the waveguide entrance (Figure 6) normalized to the average intensity of the SPP background, which does not significantly depend on the wavelength in the range of 1.425–1.525  $\mu\text{m}$ . Thus, normalized slot mode intensity is expected to be proportional to the nanocoupler effective area  $I_{\text{slot at } x=0} \sim P_{\text{WG}} \sim A_{\text{eff}}$ . The validation of such approach is supported by the comparison of simulation results (lines) with experimental results (points), shown in Figure 6a. The effective indices determined from the experimental (filtered) phase images (Figure 5c) were found in good correspondence with the calculated ones (Figure 6b), while the experimentally obtained propagation lengths turned out being slightly smaller than the calculated ones (Figure 6b), most probably due to the fabrication imperfections. One may notice small oscillations in the experimentally measured values, which, we believe represent a systematic error due to degradation or a drift in our setup, because a sequence of measurements for each antenna was 1475–1425–1525–1500–1450 nm, which correlates well with the error in propagation length and effective index (Figure 6b).

In conclusion, we have demonstrated the use of amplitude- and phase-resolved near-field mapping for complete character-

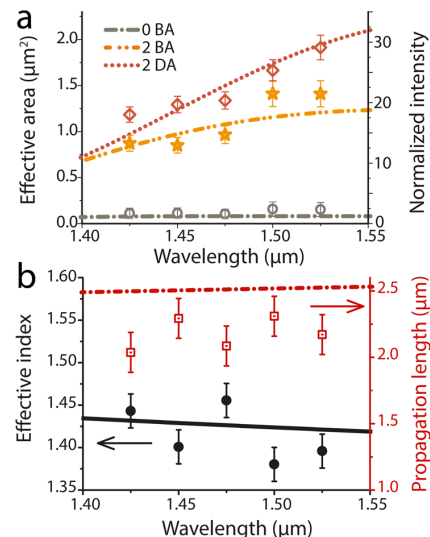


**Figure 6.** (a) Wavelength dependence of the coupling efficiency of different type of antennas: OBA (gray, circles), 2BA (orange, stars), and 2DA (red, rhombs), represented as effective area for numerical calculations (lines) and as normalized intensity for experimental results (points). (b) Wavelength dependence of the experimentally measured effective mode index (black circles) and propagation length (red squares), compared with numerical simulations (lines).

ization of the complex plasmonic waveguide configuration including antenna-based nanocouplers and slot waveguides. The *s*-SNOM characterization allowed us not only to make relative comparison of the efficiencies (in terms of the effective area) of different couplers but also to measure the effective index and propagation length of the slot waveguide mode. All experimental data were found to be in a very good correspondence with the numerical simulations. We have also confirmed that the serially connected dipole antennas represent the most efficient (for the excitation with a wide light beam) and simple design of nanocouplers. We would therefore anticipate that the serial antennas nanocouplers will become

## Nano Letters

## Letter

efficient optical interfaces between macroscopic light sources and nanoscale waveguides. We also believe that the s-SNOM-based characterization procedure described here will become a standard robust technique for the plasmonic waveguide characterization due to its high resolution, reliable measurements, and efficient data filtration procedure.

## ■ ASSOCIATED CONTENT

## S Supporting Information

Details on numerical simulation and optimization, and the fabrication procedure and the filtration procedure for experimental and simulated field distributions. This material is available free of charge via the Internet at <http://pubs.acs.org>.

## ■ AUTHOR INFORMATION

## Corresponding Authors

\*E-mail: [andra@fotonik.dtu.dk](mailto:andra@fotonik.dtu.dk).

\*E-mail: [zenin@iti.sdu.dk](mailto:zenin@iti.sdu.dk).

## Author Contributions

A. A. and V. Z. contributed equally.

## Notes

The authors declare no competing financial interest.

## ■ ACKNOWLEDGMENTS

A.A. acknowledges financial support from the Danish Council for Technical and Production Sciences through the GraTer project (Contract No. 0602-02135B). V.A.Z., V.S.V., and S.I.B. acknowledge financial support from the Danish Council for Independent Research (the FTP project ANAP, Contract No. 0602-01507B) and from the European Research Council, Grant 341054 (PLAQNAP). The authors also acknowledge J. Rosenkrantz de Lasson for a useful discussion on numerical simulations, G. Biagi, T. Holmgaard, J.-S. Bouillard, and A. V. Zayats for discussions on near-field characterization, and an anonymous reviewer for useful comments.

## ■ REFERENCES

- (1) Gramotnev, D. K.; Bozhevolnyi, S. I. *Nat. Photonics* **2010**, *4*, 83–91.
- (2) MacDonald, K. F.; Zheludev, N. I. *Laser Photonics Rev.* **2009**, *4*, 562–567.
- (3) Ozbay, E. *Science* **2006**, *311*, 189–193.
- (4) Andryieuski, A.; Lavrinenko, A. V. *Adv. OptoElectron.* **2012**, *2012*, 1–17.
- (5) Bharadwaj, P.; Deutsch, B.; Novotny, L. *Adv. Opt. Photonics* **2009**, *438–483*.
- (6) Henzie, J.; Lee, J.; Lee, M. H.; Hasan, W.; Odom, T. W. *Annu. Rev. Phys. Chem.* **2009**, *60*, 147–165.
- (7) Boltasseva, A.; Shalae, V. *Metamaterials* **2008**, *2*, 1–17.
- (8) Krasnok, A. E.; Maksymov, I. S.; Denisyuk, A. I.; Belov, P. A.; Miroshnichenko, A. E.; Simovski, C. R.; Kivshar, Y. S. *Phys.-Usp.* **2013**, *56*, 539–564.
- (9) Andryieuski, A.; Malureanu, R.; Biagi, G.; Holmgaard, T.; Lavrinenko, A. *Opt. Lett.* **2012**, *37*, 1124–1126.
- (10) Wen, J.; Romanov, S.; Peschel, U. *Opt. Express* **2009**, *17*, 5925–5932.
- (11) Huang, J.; Feichtner, T.; Biagioni, P.; Hecht, B. *Nano Lett.* **2009**, *9*, 1897–1902.
- (12) Fang, Z.; Lu, Y.; Fan, L.; Lin, C. *Plasmonics* **2010**, *5*, 57–62.
- (13) Klemm, M. *Int. J. Opt.* **2012**, *2012*, 1–7.
- (14) Obelleiro, F.; Taboada, J. M.; Solís, D. M.; Bote, L. *Opt. Lett.* **2013**, *38*, 1630–1632.
- (15) Alu, A.; Engheta, N. *Phys. Rev. Lett.* **2010**, *104*, 213902.
- (16) Wen, J.; Banzer, P.; Kriesch, A.; Ploss, D.; Schmauss, B.; Peschel, U. *Appl. Phys. Lett.* **2011**, *98*, 101109.
- (17) Fang, Z.; Fan, L.; Lin, C.; Zhang, D.; Meixner, A. J. A. J.; Zhu, X. *Nano Lett.* **2011**, *11*, 1676–1680.
- (18) Kriesch, A.; Burgos, S. P.; Ploss, D.; Pfeifer, H.; Atwater, H. A.; Peschel, U. *Nano Lett.* **2013**, *13*, 4539–4545.
- (19) Schnell, M.; Alonso-Gonzalez, P.; Arzubiaga, L.; Casanova, F.; Hueso, L. E.; Chuvilin, A.; Hillenbrand, R. *Nat. Photonics* **2011**, *5*, 283–287.
- (20) Veronis, G.; Fan, S. *J. Light. Technol.* **2007**, *25*, 2511–2521.
- (21) CST. Computer Simulation Technology, AS <http://cst.com> (accessed June 3, 2014).
- (22) Schnell, M.; Garcia-Etxarri, A.; Huber, A. J.; Crozier, K. B.; Borisov, A.; Aizpurua, J.; Hillenbrand, R. *J. Phys. Chem. C* **2010**, *114*, 7341–7345.
- (23) Ocelic, N.; Huber, A.; Hillenbrand, R. *Appl. Phys. Lett.* **2006**, *89*, 101124.
- (24) García-Etxarri, A.; Romero, I.; García de Abajo, F.; Hillenbrand, R.; Aizpurua, J. *Phys. Rev. B* **2009**, *79*, 125439.
- (25) Esteban, R.; Vogelgesang, R.; Dorfmueller, J.; Dmitriev, A.; Rockstuhl, C.; Etrich, C.; Kern, K. *Nano Lett.* **2008**, *8*, 3155–3159.
- (26) Schnell, M.; Garcia-Etxarri, A.; Huber, A.; Crozier, K. B.; Aizpurua, J.; Hillenbrand, R. *Nat. Photonics* **2009**, *3*, 287–291.
- (27) Gwyddion, <http://gwyddion.net/> (accessed June 3, 2014).

# Direct Characterization of Plasmonic Slot Waveguides and Nanocouplers

*Andrei Andryieuski<sup>†\*</sup>, Vladimir A. Zenin<sup>‡\*\*</sup>, Radu Malureanu<sup>†</sup>, Valentyn S. Volkov<sup>‡</sup>, Sergey I. Bozhevolnyi<sup>‡</sup>, and Andrei V. Lavrinenko<sup>†</sup>*

<sup>†</sup>DTU Fotonik, Technical University of Denmark, Ørstedss pl. 343, Kongens Lyngby DK-2800, Denmark

<sup>‡</sup>Department of Technology and Innovation, University of Southern Denmark, Niels Bohrs Alle 1, Odense M DK-5230, Denmark

\* E-mail: [andra@fotonik.dtu.dk](mailto:andra@fotonik.dtu.dk)

\* E-mail: [zenin@iti.sdu.dk](mailto:zenin@iti.sdu.dk)

## Supporting information

**Numerical simulation and optimization.** Simulations are done in CST Microwave Studio<sup>1</sup> with the time-domain finite-integrals method. A hexahedral mesh with the mesh refinement around the slot waveguide is used. The simulation domain consists of a thick silica substrate (3  $\mu\text{m}$ ), waveguide, antenna and thick air superstrate (4  $\mu\text{m}$ ) (Figure S1a). Gold is described with the Drude formula<sup>2</sup> with plasma frequency  $1.36 \times 10^{16} \text{ s}^{-1}$  and collision frequency  $1.57 \times 10^{14} \text{ s}^{-1}$ . The dielectric substrate has a refractive index  $n = 1.47$ . A plane wave is used for the excitation

of the structure. The boundary conditions are perfect electric conductor (PEC) in the x-, and open (perfectly matched layers) in y- and z-directions. To ensure the absence of coupling to the mirror images of antennas at the PEC x- boundaries, the lateral size of the simulation domain is  $11\ \mu\text{m}$ , the longitudinal size is  $9\ \mu\text{m}$  (for calculations of the effective area and optimization) or  $19\ \mu\text{m}$  (for calculations of the electromagnetic fields). Typical simulation with a 12 CPUs (3.5 GHz), 48 GB RAM personal computer takes 1 hour. Numerical optimization with maximization of the effective area as a goal was done with the Nelder-Mead simplex algorithm with the parameters variation range  $\pm 25\%$  from the initial values. The initial values were selected through maximization of the effective area for all parameters one-by-one variation. The optimal parameters are shown in Table S1 with the geometrical parameters marked in Figure S1b,c.

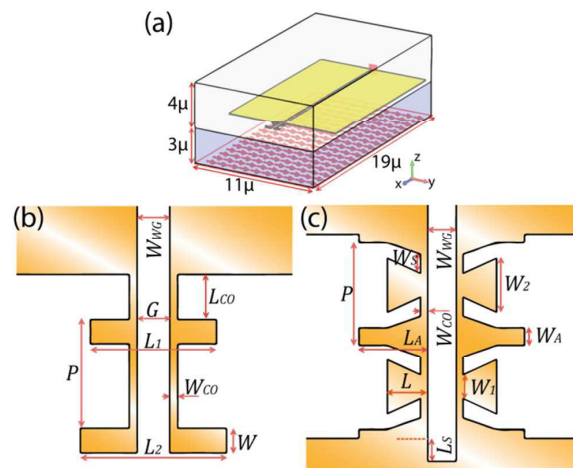


**Figure S1.** (a) Simulation domain used for the fields calculation in CST Microwave Studio. In case of effective area calculation the longitudinal size of the domain was  $9\ \mu\text{m}$  instead of  $19\ \mu\text{m}$ . Optimized serially connected (b) dipole and (c) modified bow-tie antennas. The values of optimal geometrical parameters are presented in the Table S1.

Initially we observed spurious Fabry-Perot resonances in the effective area spectra due to poorly absorbed scattered field by a single-mode plane wave port in CST (the excitation plane wave is shown with arrows in Figure S1a). This issue has been resolved by increasing the number of the port modes to 20 and proper time windowing of the received signal. The electric field recorded with a frequency 3D monitor was collected 50 nm above the top waveguide surface, corresponding to the average position of the s-SNOM tip in experiments. In order to reduce the influence of the fake Fabry-Perot resonances on the simulated electric field, the width of the excitation port was decreased to 4  $\mu\text{m}$ .

**Table S1.** Waveguide and nanocouplers geometrical parameters, designed and fabricated.

Parameter	Designed	Fabricated	St. deviation
All structures			
$H$ (nm)	50	50	1
Waveguide			
$W_{WG}$ (nm)	300	287	7
Dipole antennas coupler (2DA)			
$L_1$ (nm)	1144	1117	8
$L_2$ (nm)	1290	1293	10
$G$ (nm)	290	288	5
$W$ (nm)	210	213	6
$L_{CO}$ (nm)	443	396	10
$W_{CO}$ (nm)	80	82	8
$P$ (nm)	969	969	8
Bow-tie antenna coupler (2BA)			
$L$ (nm)	437	425	10
$W_1$ (nm)	233	246	12
$W_2$ (nm)	560	562	13
$L_A$ (nm)	683	647	7

$W_A$ (nm)	70	74	11
$W_{CO}$ (nm)	76	74	8
$W_S$ (nm)	230	200	17
$L_S$ (nm)	230	234	4
$P$ (nm)	1069	1071	20

Upon the incident wave's diffraction through the slot the surface plasmon polaritons (SPPs) are excited on the metal-dielectric interfaces. We use SPPs on metal-air interface to normalize the intensity of the slot mode. Numerical simulations (see Figure S2) confirm that the amplitude of the excited metal-air SPP does not significantly depend on the wavelength in the range of interest 1425-1525 nm and therefore the normalized slot mode intensity is proportional to the effective area.

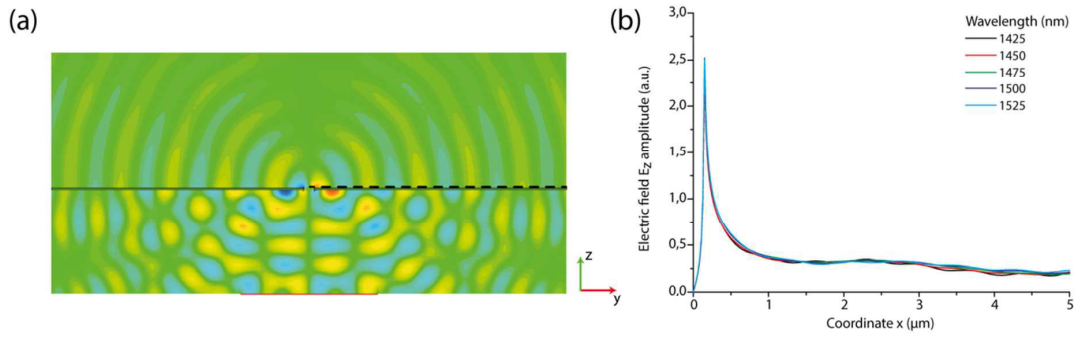


**Figure S2.** (a) Vertical electric field  $E_z$  (real part) distribution in the plane perpendicular to the slot. The y-polarized incident wave excites SPP on the air-metal interface upon diffraction through the slot. (b) Electric field  $E_z$  amplitude along the dashed line in the part (a) demonstrates that the intensity of the excited SPP does not significantly depend on the wavelength.

**Fabrication.** The waveguides and antennas were fabricated on a borofloat glass 500 $\mu\text{m}$  thick substrate (Jinsol). ZEP 520 5.5% (in anisole) resist (thickness 150 nm) was used for electron beam lithography. To prevent charge accumulation a 20 nm thick Al layer was thermally deposited (Wordentec QCL 800). The resist was exposed with 100 kV JEOL JBX-9300FS electron beam lithography system at the charge dose 200  $\mu\text{C}/\text{cm}^2$ . Then Al was removed with commercial MF-322 remover until no visible signs of metal were presented, and the resist was developed in ZED N50 developer for 120 s. Then 1 nm Cr and 49 nm Au were e-beam evaporated (Wordentec QCL 800). During the lift-off the sample was staying in hot acetone (50 C) upside down for 2 hours under constant stirring. Then slight ultrasound was applied for 2 minutes. Finally the sample was rinsed with acetone and isopropanol and carefully dried with nitrogen. After the fabrication we performed lateral size measurements with a scanning electron microscope (FEI Nova 600 NanoSEM and SEM Zeiss Supra 40 VP) and thickness measurements with an atomic force microscope (Dimension 3100 Bruker AXS). The values of the geometrical parameters of the fabricated structures and standard deviations are shown in Table S1. The SEM images of 0BA, 2BA and 2DA structures are shown in Figure S3.

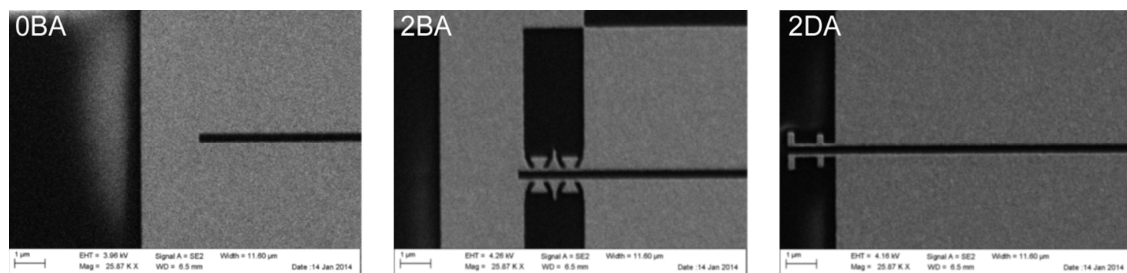


**Figure S3.** SEM microphotos of the fabricated 0BA, 2 BA and 2DA structures.

**Field data processing.** A main idea of filtering near-field data is that the recorded field resulted from the interference of two dominating modes: the slot mode propagating along the

waveguide, and SPP, excited on the edges of the waveguide and therefore travelling across it. However, there is a small difference in treating experimental and simulated near-fields, due to a slightly different excitation and measurement procedures. In our experiment the waveguides were illuminated with a defocused Gaussian beam, which can be described as following:

$$E(x, y) = E_0 \exp\left[-\frac{x^2 + y^2}{w^2(z)}\right] \exp\left[ik_0 \frac{x^2 + y^2}{2R(z)}\right] = E_0 \exp\left[ik_2 (x^2 + y^2)\right],$$

$$\left. \begin{aligned} w^2(z) &= w_0^2 \left[1 + \left(\frac{z}{z_R}\right)^2\right] \\ R(z) &= z \left[1 + \left(\frac{z_R}{z}\right)^2\right] \end{aligned} \right\} k_2 = \frac{k_0}{2R(z)} + \frac{i}{w^2(z)},$$

$$z_R = \frac{\pi w_0^2}{\lambda}, \quad k_0 = \frac{2\pi}{\lambda}$$

where  $E_0$  is an electric field amplitude,  $\lambda$  is a free-space wavelength of illumination,  $w_0 \approx 3 \mu\text{m}$  is a waist of the Gaussian beam, and  $z \approx 65 \mu\text{m}$  is a vertical shift of the excitation parabolic mirror, used to increase the width of the illumination spot. Since only the sample is moving during the scan, the amplitude and phase of the Gaussian beam adjusted with the AFM tip will be changed at the position of the antenna during the scan change. Therefore, the measured amplitude of the slot mode will be in fact a convolution of the Gaussian beam profile and real propagation field. Then one can fit measured data with following:

$$E_{\text{measured}}(x, y) \rightarrow E_{\text{SPP}}(y) + E_{\text{slot}}(y) \exp[ik_{\text{slot}}x] \exp\left[ik_2 (x - x_0)^2\right]$$

where  $E_{\text{measured}}$ ,  $E_{\text{SPP}}$ ,  $E_{\text{slot}}$ ,  $k_{\text{slot}}$ ,  $k_2$  are complex-valued functions and variables (taking into account amplitude and phase for  $E$ -field and propagation with decay for the  $k$ -vector), and  $x_0$  is an effective coordinate of the antenna (in our fitting we assumed it to be  $1 \mu\text{m}$  from the edge of continuous gold for 2BA and 2DA; for 0BA it was assumed to be at the beginning of the waveguide). In our fitting  $k_{\text{slot}}$  was a global fitting parameter (one for the whole image), while



$E_{\text{SPP}}$  and  $E_{\text{slot}}$  were fitting parameters for each line along x-axis. The fitting was done in MATLAB by the least squares method with a use of the built-in MATLAB function *lsqcurvefit*. The results of the fitting for 2DA are shown in Figure S4, where the measured data,  $E_{\text{measured}}(x, y)$  is denoted as RAW, the first term of fitting,  $E_{\text{SPP}}(y)$ , is denoted as SPP, the second term,  $E_{\text{slot}}(y) \exp[ik_{\text{slot}}x] \exp[ik_2(x-x_0)^2]$ , is denoted as Slot mode, and the difference,  $E_{\text{measured}}(x, y) - E_{\text{SPP}}(y) - E_{\text{slot}}(y) \exp[ik_{\text{slot}}x] \exp[ik_2(x-x_0)^2]$ , as Residual field.

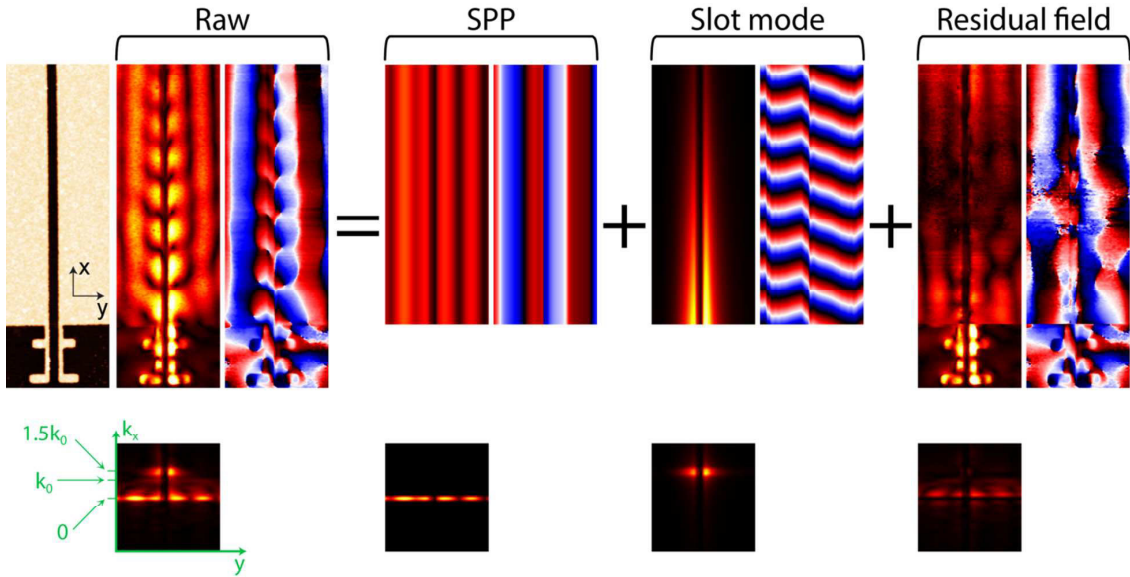


**Figure S4.** Fitting procedure shown on an example of 2DA. Top: Decomposition of the recorded Raw complex-valued data into fitted SPP, Slot mode, and Residual field. Bottom: the same procedure seen in k-space after applying 1D DFT along the waveguide ( $191 \times 31$  pixels, linearly interpolated to  $191 \times 200$  pixels for clarity).

In order to present results concisely, we added the top part of Residual field (containing the waveguide) to SPP and showed it as the SPP background in our work [Figure 4 (e)-(g)], while the original near-field of the antenna (bottom part without waveguide), glued with fitted Slot

mode, is referred to as the slot mode field in our work [Figure 4 (h)-(j)]. The complete procedure of fitting is shown in Figure S4. One can note that there is still relatively large residual field near the beginning of the waveguide, which we ascribe to the excitation and propagation of the SPP, travelling partially along  $x$ -axis, due to the diffraction of the incident beam on the antenna and due to the edge effects for SPP, propagating across the waveguide. However, such distortion does not significantly influence the fitted slot mode and the filtering procedure, which is verified by a one-dimensional discrete Fourier transform (1D DFT) of the top part of complex-valued Raw, SPP, Slot mode, and Residual field along the waveguide (see bottom part of Figure S4). Note that due to a rather limited scanned area Fourier analysis does not allow to accurately determine waveguiding propagation constant  $k_{\text{slot}}$ .

Such fitting allowed determining propagation length and effective mode index of the slot mode for each wavelength [Figure 6(b)]. The normalized intensity of the slot mode was estimated as average value of squared  $E_{\text{slot}}$ , measured at the entrance of waveguide,  $x_1$ , and normalized to the average value of squared  $E_{\text{SPP}}$ , i.e.,

$$I_{\text{slot}} = \frac{\int E_{\text{slot}}(y) \exp[ik_{\text{slot}}x_1] \exp\left[ik_2(x_1 - x_0)^2\right] dy}{\int E_{\text{SPP}}(y) dy}.$$

For 0BA, due to a weak slot mode,  $k_{\text{slot}}$  was fixed and determined by linear fitting of  $k_{\text{slot}}$  for 2DA and 2BA, so only the normalized intensity was determined during the fitting procedure.

As for the numerical simulations with plane wave excitation, the electrical field  $E_z$ , measured at 50 nm above the structure, appeared to contain substantial background of propagating light and SPP, excited on far edges of the sample due to diffraction. Such background negligibly influences the measurements of propagation constant and coupling efficiency, but creates a large obstacle for field filtering. Therefore, for near-field simulations, we used a cylindric Gaussian

beam (homogenous along  $x$ - and Gaussian along  $y$ -axis) to excite slot mode and cross-propagating SPP. The complete results of fitting the experimentally measured and numerically simulated near-field are presented in Figures S5 and S6, correspondingly.

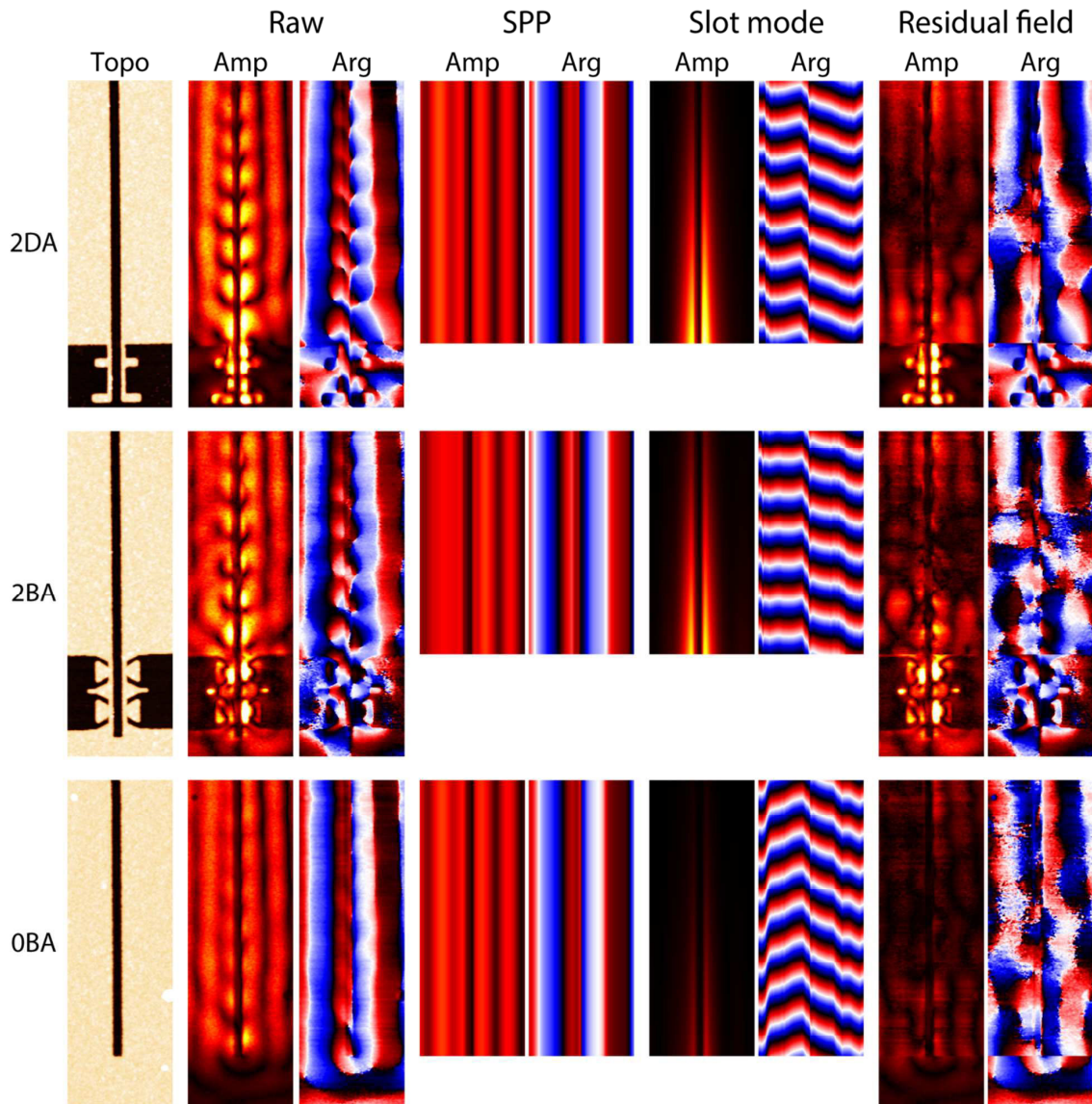


**Figure S5.** Results of fitting measured data for all measured antennas.

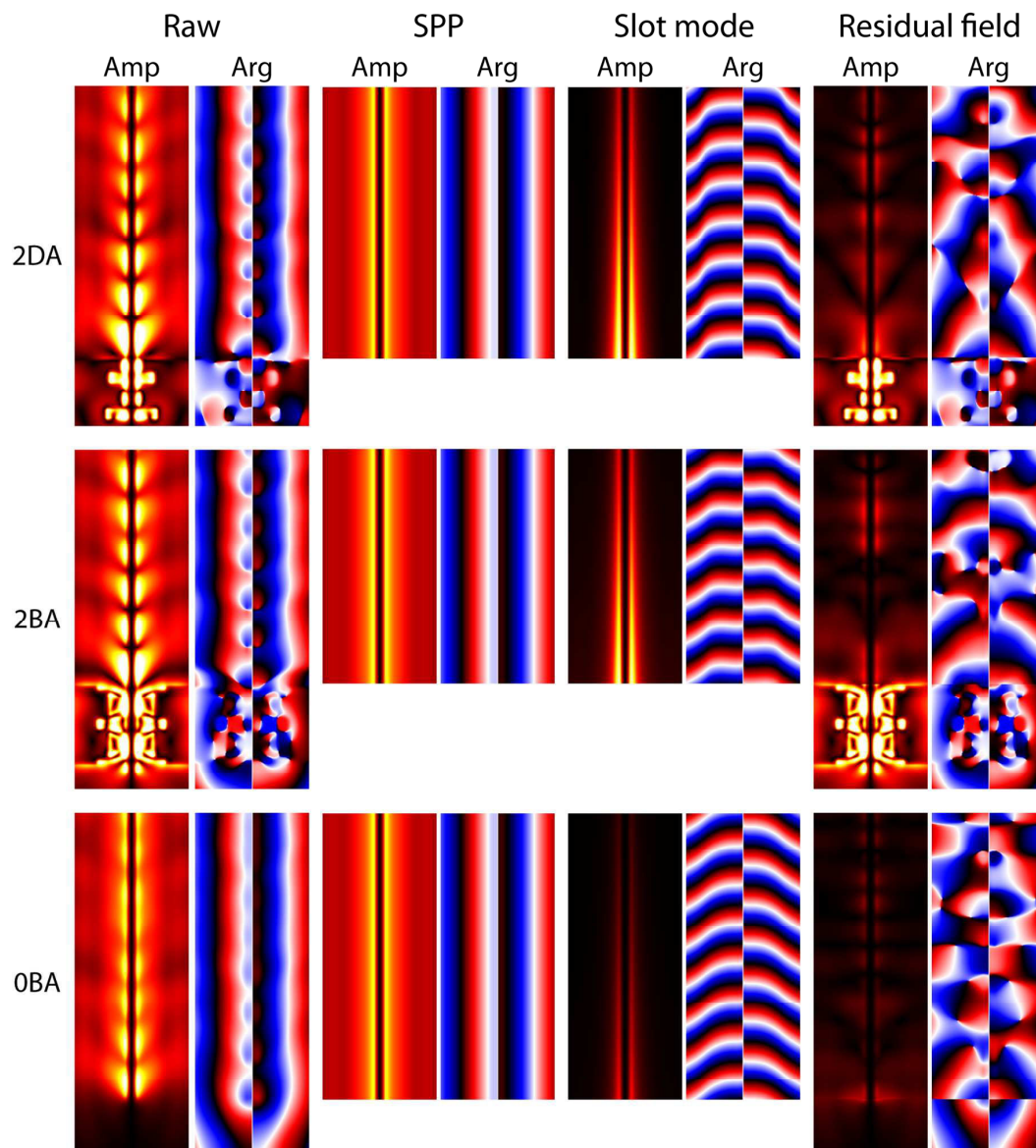


**Figure S6.** Results of fitting numerically simulated near-field.

### References

- (1) CST. Computer Simulation Technology, AS <http://cst.com>.
- (2) Rakic, A D.; Djuricic, A. B.; Elazar, J. M.; Majewski, M. L.; Djuris, A. B. *Appl. Opt.* **1998**, *37*, 5271–5283.

## Authorship agreements

---

**Authorship Agreement**

This authorship agreement concerns the published research work conducted by PhD Student Volodymyr Zenin, Valentyn S. Volkov, Zhanghua Han, Sergey I. Bozhevolnyi, Eloïse Devaux, and Thomas W. Ebbesen.

The research work includes the following article:

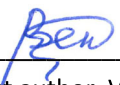
**J. Opt. Soc. Am. B 28(7), 1596–1602 (2011)**

***Dispersion of strongly confined channel plasmon polariton modes***

In accordance with the criteria put forward at the Vancouver Convention for authorship ([www.icmje.org](http://www.icmje.org)), the undersigned Volodymyr Zenin confirms that he as first author is responsible for

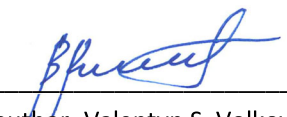
- A substantial contribution of the intellectual content
- Characterization of samples with SNOM
- Treatment of experimental data
- Simulations for infinitely deep groove
- Preparation of all figures
- Critical revisions of the manuscript
- The finalization of the versions to be published

Similarly, the undersigned Valentyn S. Volkov, Zhanghua Han, Sergey I. Bozhevolnyi, Eloïse Devaux, and Thomas W. Ebbesen confirms that they as co-authors have contributed quantitatively and qualitatively to the conception and design, the critical revision for important intellectual content, the interpretation of experimental evidence, and the final approval of the versions to be published. As senior researcher, Sergey I. Bozhevolnyi stands as guarantor and takes public responsibility for the integrity of the research work as a whole, from inception to published articles.




---

First author, Volodymyr Zenin




---

Co-author, Valentyn S. Volkov



---

Co-author, Zhanghua Han



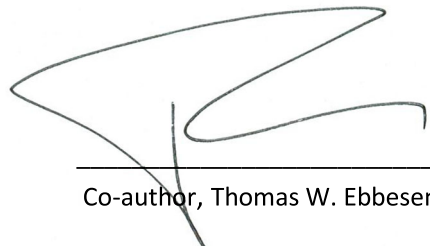
---

Co-author, Sergey I. Bozhevolnyi



---

Co-author, Eloïse Devaux



---

Co-author, Thomas W. Ebbesen

## Authorship Agreement

This authorship agreement concerns the published research work conducted by PhD Student Volodymyr Zenin, Valentyn S. Volkov, Zhanghua Han, Sergey I. Bozhevolnyi, Eloïse Devaux, and Thomas W. Ebbesen.

The research work includes the following article:

**Opt. Express 20(6), 6124–6134 (2012)**

***Directional coupling in channel plasmon-polariton waveguides***

In accordance with the criteria put forward at the Vancouver Convention for authorship ([www.icmje.org](http://www.icmje.org)), the undersigned Volodymyr Zenin confirms that he as first author is responsible for

- A substantial contribution of the intellectual content
- Characterization of samples with SNOM
- Treatment of experimental data
- FEM simulations
- Preparation of all figures
- The initial drafting of the manuscript and the finalization of the versions to be published

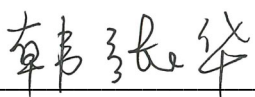
Similarly, the undersigned Valentyn S. Volkov, Zhanghua Han, Sergey I. Bozhevolnyi, Eloïse Devaux, and Thomas W. Ebbesen confirms that they as co-authors have contributed quantitatively and qualitatively to the conception and design, the critical revision for important intellectual content, the interpretation of experimental evidence, and the final approval of the versions to be published. As senior researcher, Sergey I. Bozhevolnyi stands as guarantor and takes public responsibility for the integrity of the research work as a whole, from inception to published articles.



First author, Volodymyr Zenin



Co-author, Valentyn S. Volkov



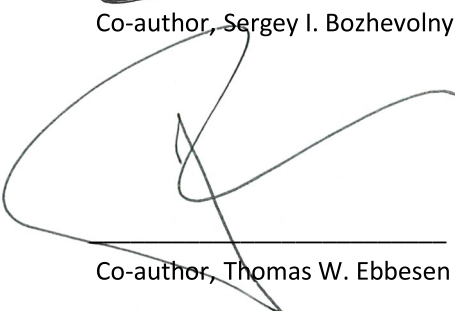
Co-author, Zhanghua Han



Co-author, Sergey I. Bozhevolnyi



Co-author, Eloïse Devaux



Co-author, Thomas W. Ebbesen

**Authorship Agreement**

This authorship agreement concerns the published research work conducted by PhD Student Volodymyr Zenin, Zhanghua Han, Valentyn S. Volkov, Kristjan Leosson, Ilya P. Radko, and Sergey I. Bozhevolnyi.

The research work includes the following article:


**Opt. Express 21(7), 8799–8807 (2013)**

***Directional coupling in long-range dielectric-loaded plasmonic waveguides***

In accordance with the criteria put forward at the Vancouver Convention for authorship ([www.icmje.org](http://www.icmje.org)), the undersigned Volodymyr Zenin confirms that he as first author is responsible for

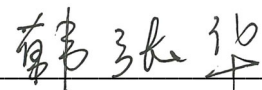
- A substantial contribution of the intellectual content
- Characterization of samples with SNOM
- Treatment of experimental data
- FEM simulations
- Preparation of all figures
- The initial drafting of the manuscript and the finalization of the versions to be published

Similarly, the undersigned Zhanghua Han, Valentyn S. Volkov, Kristjan Leosson, Ilya P. Radko, and Sergey I. Bozhevolnyi confirms that they as co-authors have contributed quantitatively and qualitatively to the conception and design, the critical revision for important intellectual content, the interpretation of experimental evidence, and the final approval of the versions to be published. As senior researcher, Sergey I. Bozhevolnyi stands as guarantor and takes public responsibility for the integrity of the research work as a whole, from inception to published articles.



---

First author, Volodymyr Zenin



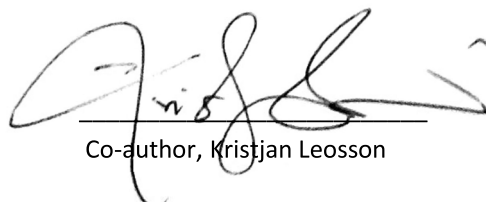
---

Co-author, Zhanghua Han



---

Co-author, Valentyn S. Volkov



---

Co-author, Kristjan Leosson



---

Co-author, Ilya P. Radko



---

Co-author, Sergey I. Bozhevolnyi



### Authorship Agreement

This authorship agreement concerns the published research work conducted by PhD Student Volodymyr Zenin, Anders Pors, Zhanghua Han, René L. Eriksen, Valentyn S. Volkov, and Sergey I. Bozhevolnyi.

The research work includes the following article:

**Opt. Express 22(9), 10341–10350 (2014)**

***Nanofocusing in circular sector-like nanoantennas***

In accordance with the criteria put forward at the Vancouver Convention for authorship ([www.icmje.org](http://www.icmje.org)), the undersigned Volodymyr Zenin confirms that he as first author is responsible for

- A substantial contribution of the intellectual content
- Characterization of samples with s-SNOM
- Treatment of experimental data
- Interpretation of numerically simulated data
- Preparation of all figures
- The initial drafting of the manuscript and the finalization of the versions to be published

Similarly, the undersigned Anders Pors, Zhanghua Han, René L. Eriksen, Valentyn S. Volkov, and Sergey I. Bozhevolnyi confirms that they as co-authors have contributed quantitatively and qualitatively to the conception and design, the critical revision for important intellectual content, the interpretation of experimental evidence, and the final approval of the versions to be published. As senior researcher, Sergey I. Bozhevolnyi stands as guarantor and takes public responsibility for the integrity of the research work as a whole, from inception to published articles.



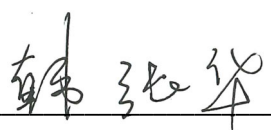
---

First author, Volodymyr Zenin



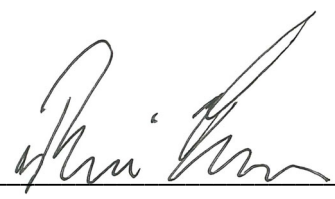
---

Co-author, Anders Pors



---

Co-author, Zhanghua Han



---

Co-author, René L. Eriksen



---

Co-author, Valentyn S. Volkov



---

Co-author, Sergey I. Bozhevolnyi

**Authorship Agreement**

This authorship agreement concerns the published research work conducted by Andrei Andryieuski, PhD Student Volodymyr Zenin, Radu Malureanu, Valentyn S. Volkov, Sergey I. Bozhevolnyi, and Andrei V. Lavrinenko.

The research work includes the following article:

**Nano Lett. 14, 3925–3929 (2014).**

***Direct characterization of plasmonic slot waveguides and nanocouplers***

**Author contributions: A. A. and V. Z. contributed equally.**

In accordance with the criteria put forward at the Vancouver Convention for authorship ([www.icmje.org](http://www.icmje.org)), the undersigned Volodymyr Zenin confirms that he as co-author is responsible for


- A substantial contribution of the intellectual content
- Characterization of samples with s-SNOM
- Treatment of experimental data
- Interpretation of numerically simulated data
- Preparation of figures
- Critical revisions of the manuscript

Similarly, the undersigned Andrei Andryieuski, Radu Malureanu, Valentyn S. Volkov, Sergey I. Bozhevolnyi, and Andrei V. Lavrinenko confirm that they have contributed quantitatively and qualitatively to the conception and design, the critical revision for important intellectual content, the interpretation of experimental evidence, and the final approval of the versions to be published. As senior researcher, Sergey I. Bozhevolnyi stands as guarantor and takes public responsibility for the integrity of the research work as a whole, from inception to published articles.



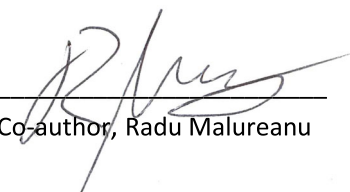
---

First author, Andrei Andryieuski




---

Co-author, Volodymyr Zenin




---

Co-author, Radu Malureanu




---

Co-author, Valentyn S. Volkov



---

Co-author, Sergey I. Bozhevolnyi



---

Co-author, Andrei V. Lavrinenko

# Bibliography

---



## References

---

- [1] H. Raether, *Surface Plasmons* (Springer-Verlag, 1988).
- [2] S. I. Bozhevolnyi, ed., *Plasmonic Nanoguides and Circuits* (Pan Stanford Publ., 2008).
- [3] R. Zia, J. A. Schuller, A. Chandran, and M. L. Brongersma. “Plasmonics: the next chip-scale technology,” *Materials Today* **9**, 20–27 (2006).
- [4] D. K. Gramotnev and S. I. Bozhevolnyi, “Plasmonics beyond the diffraction limit,” *Nat. Photonics* **4**, 83 (2010).
- [5] S. A. Maier, *Plasmonics: fundamentals and applications* (Springer, 2007).
- [6] P. Drude, “Zur Elektronentheorie der Metalle,” *Ann. Phys.* **306**, 566–613 (1900).
- [7] E. Palik and G. Ghosh, *Handbook of Optical Constants of Solids II* (Academic Press, 1991).
- [8] Z. Han and S. I. Bozhevolnyi, “Radiation guiding with surface plasmon polaritons,” *Rep. Prog. Phys.* **76**, 016402 (2013).
- [9] R. F. Oulton, G. Bartal, D. F. P. Pile, and X. Zhang, “Confinement and propagation characteristics of subwavelength plasmonic modes,” *New J. Phys.* **10**, 105018 (2008).
- [10] R. D. Kekatpure, A. C. Hryciw, E. S. Barnard, and M. L. Brongersma, “Solving dielectric and plasmonic waveguide dispersion relations on a pocket calculator,” *Opt. Express* **17**, 24112–24129 (2010).

- 
- [11] A. Drezet, A. Hohenau, D. Koller, A. Stepanov, H. Ditlbacher, B. Steinberger, F.R. Aussenegg, A. Leitner, and J.R. Krenn, “Leakage radiation microscopy of surface plasmon polaritons,” *Materials Science and Engineering B* **149**, 220–229 (2008).
- [12] S. I. Bozhevolnyi and J. Jung, “Scaling for gap plasmon based waveguides,” *Opt. Express* **16**, 2676–2684 (2008).
- [13] J. Q. Lu and A. A. Maradudin, “Channel plasmons,” *Phys. Rev. B* **42**, 11159–11165 (1990).
- [14] I. V. Novikov and A. A. Maradudin, “Channel polaritons,” *Phys. Rev. B* **66**, 035403 (2002).
- [15] S. I. Bozhevolnyi, V. S. Volkov, E. Devaux, and T. W. Ebbesen, “Channel plasmon-polariton guiding by subwavelength metal grooves,” *Phys. Rev. Lett.* **95**, 046802 (2005).
- [16] V. S. Volkov, S. I. Bozhevolnyi, E. Devaux, and T. W. Ebbesen, “Bend loss for channel plasmon polaritons,” *Appl. Phys. Lett.* **89**, 143108 (2006).
- [17] S. I. Bozhevolnyi, V. S. Volkov, E. Devaux, J.-Y. Laluet, and T. W. Ebbesen, “Channel plasmon subwavelength waveguide components including interferometers and ring resonators,” *Nature* **440**, 508–511 (2006).
- [18] S. I. Bozhevolnyi and K. V. Nerkararyan, “Channel plasmon polaritons guided by graded gaps: closed-form solutions,” *Opt. Express* **17**, 10327–10334 (2009)
- [19] S. I. Bozhevolnyi and K. V. Nerkararyan, “Analytic description of channel plasmon polaritons,” *Opt. Lett.* **34**, 2039–2041 (2009).
- [20] S. I. Bozhevolnyi, “Effective-index modeling of channel plasmon polaritons,” *Opt. Express* **14**, 9467–9476 (2006).
- [21] C. L. C. Smith, A. H. Thilsted, C. E. Garcia-Ortiz, I. P. Radko, R. Marie, C. Jeppesen, C. Vannahme, S. I. Bozhevolnyi, and A. Kristensen, “Efficient excitation of channel plasmons in tailored, UV-lithography-defined V-grooves,” *Nano Lett.* **14**, 1659–1664 (2014).
- [22] V. S. Volkov, Z. Han, M. G. Nielsen, K. Leosson, H. Keshmiri, J. Gosciniak, O. Albrektsen, and S. I. Bozhevolnyi, “Long-range dielectric-loaded surface plasmon polariton waveguides operating at telecommunication wavelengths,” *Opt. Lett.* **36**, 4278–4280 (2011).
- [23] G. Veronis, S. Fan, “Modes of subwavelength plasmonic slot waveguides,” *J. Light. Technol.* **25**, 2511–2521 (2007).

- 
- [24] R. B. Pettit, J. Silcox, and R. Vincent, “Measurement of surface-plasmon dispersion in oxidized aluminum films,” *Phys. Rev. B* **11**, 3116–3123 (1975).
- [25] F. J. Garcia de Abajo, “Optical excitations in electron microscopy,” *Rev. Mod. Phys.* **82**, 209–275 (2010).
- [26] H. Ditlbacher, J. R. Krenn, G. Schider, A. Leitner, and F. R. Aussenegg, “Two-dimensional optics with surface plasmon polaritons,” *Appl. Phys. Lett.* **81**, 1762–1764 (2002).
- [27] C. Lemke, T. Leißner, S. Jauernik, A. Klick, J. Fiutowski, J. Kjelstrup-Hansen, H.-G. Rubahn, and M. Bauer, “Mapping surface plasmon polariton propagation via counter-propagating light pulses,” *Opt. Express* **20**, 12877–12884 (2012).
- [28] I. P. Radko, S. I. Bozhevolnyi, A. B. Evlyukhin, and A. Boltasseva, “Surface plasmon polariton beam focusing with parabolic nanoparticle chains,” *Opt. Express* **15**, 6576–6582 (2007).
- [29] D. Courjon, *Near-field microscopy and near-field optics* (Imperial College Press, 2003).
- [30] E. Kretschmann and H. Raether, “Radiative decay of non-radiative surface plasmons excited by light,” *Z. Naturforschung A* **23**, 2135–2136 (1968).
- [31] A. Otto, “Excitation of nonradiative surface plasma waves in silver by the method of frustrated total reflection,” *Z. Physik* **216**, 398–410 (1968).
- [32] R. Stöckle, C. Fokas, V. Deckert, R. Zenobia, B. Sick, B. Hecht, and U. P. Wild, “High-quality near-field optical probes by tube etching,” *Appl. Phys. Lett.* **75**, 160–162 (1999).
- [33] S. I. Bozhevolnyi, B. Vohnsen, and E. A. Bozhevolnaya, “Transfer functions in collection scanning near-field optical microscopy,” *Opt. Commun.* **172**, 171–179 (1999).
- [34] I. P. Radko, S. I. Bozhevolnyi, and N. Gregersen, “Transfer function and near-field detection of evanescent waves,” *Appl. Opt.* **45**, 4054–4061 (2006).
- [35] M. Schnell, A. Garcia-Etxarri, A. J. Huber, K. B. Crozier, A. Borisov, J. Aizpurua, and R. Hillenbrand, “Amplitude- and phase-resolved near-field mapping of infrared antenna modes by transmission-mode scattering-type near-field microscopy,” *J. Phys. Chem. C* **114**, 7341–7345 (2010).
- [36] N. Ocelic, A. Huber, and R. Hillenbrand, “Pseudoheterodyne detection for background-free near-field spectroscopy,” *Appl. Phys. Lett.* **89**, 101124 (2006).

- 
- [37] F. Keilmann and R. Hillenbrand, “Near-Field Microscopy by Elastic Light Scattering from a Tip,” *Philos. Trans. R. Soc. A* **362**, 787–805 (2004).
- [38] R. Hillenbrand and F. Keilmann, “Complex Optical Constants on a Sub-wavelength Scale”, *Phys. Rev. Lett.* **85**, 3029–3032 (2000).
- [39] J. M. Stiegler, Y. Abate, A. Cvitkovic, Y. E. Romanyuk, A. J. Huber, S. R. Leone, and Rainer Hillenbrand, “Nanoscale Infrared Absorption Spectroscopy of Individual Nanoparticles Enabled by Scattering-Type Near-Field Microscopy,” *ACS Nano* **5**, 6494–6499 (2011).
- [40] A. Garcia-Etxarri, I. Romero, F. J. Garcia de Abajo, R. Hillenbrand, and J. Aizpurua, “Influence of the tip in near-field imaging of nanoparticle plasmonic modes: weak and strong coupling regimes,” *Phys. Rev. B* **79**, 125439 (2009).
- [41] R. Esteban, R. Vogelgesang, J. Dorfüller, A. Dmitriev, C. Rockstuhl, C. Etrich, and K. Kern, “Direct near-field optical imaging of higher order plasmonic resonances,” *Nano Lett.* **8**, 3155–3159 (2008)
- [42] M. Schnell, A. Garcia-Etxarri, A. J. Huber, K. Crozier, J. Aizpurua, and R. Hillenbrand, “Controlling the near-field oscillations of loaded plasmonic nanoantennas,” *Nature Photonics* **3**, 287–291 (2009).
- [43] R. L. Olmon, P. M. Krenz, A. C. Jones, G. D. Boreman, and M. B. Raschke, “Near-field imaging of optical antenna modes in the mid-infrared,” *Opt. Express* **16**, 20295–20305 (2008).
- [44] M. Schnell, P. Alonso-Gonzalez, L. Arzubiaga, F. Casanova, L. E. Hueso, A. Chuvilin, and R. Hillenbrand, “Nanofocusing of mid-infrared energy with tapered transmission lines,” *Nature Photonics* **5**, 283–287 (2011).
- [45] B. Deutsch, R. Hillenbrand, and L. Novotny, “Near-field amplitude and phase recovery using phase-shifting interferometry,” *Opt. Express* **16**, 494–501 (2008).
- [46] M. Schnell, P.S. Carney, and R. Hillenbrand, “Synthetic optical holography for rapid nanoimaging,” *Nat. Commun.* **5**, 3499 (2014).



## List of publications

---

### Articles in peer-reviewed journals

- 1:** V. A. Zenin, V. S. Volkov, Z. Han, S. I. Bozhevolnyi, E. Devaux, and T. W. Ebbesen, “Dispersion of strongly confined channel plasmon polariton modes,” *J. Opt. Soc. Am. B* **28**, 1596–1602 (2011).
- 2:** V. A. Zenin, V. S. Volkov, Z. Han, S. I. Bozhevolnyi, E. Devaux, and T. W. Ebbesen, “Directional coupling in channel plasmon-polariton waveguides,” *Opt. Express* **20**, 6124–6134 (2012).
- 3:** V. A. Zenin, Z. Han, V. S. Volkov, K. Leosson, I. P. Radko, and S. I. Bozhevolnyi, “Directional coupling in long-range dielectric-loaded plasmonic waveguides,” *Opt. Express* **21**, 8799–8807 (2013).
- 4:** V. A. Zenin, A. Pors, Z. Han, R. L. Eriksen, V. S. Volkov, and S. I. Bozhevolnyi, “Nanofocusing in circular sector-like nanoantennas,” *Opt. Express* **22**, 10341–10350 (2014).
- 5:** A. Andryieuski, V. A. Zenin, R. Malureanu, V. S. Volkov, S. I. Bozhevolnyi, and A. V. Lavrinenko, “Direct characterization of plasmonic slot waveguides and nanocouplers,” *Nano Lett.* **14**, 3925–3929 (2014). Author contributions: A. A. and V. A. Z. contributed equally.

### Presentations

- 1:** Poster presentation with the title “Dispersion of strongly confined channel plasmon polariton modes,” Danish Optical Society annual meeting, November 2011, Århus (Denmark).

- 2:** Poster presentation with the title “Directional coupling in channel plasmon-polariton waveguides,” E-MRS 2012 Spring Meeting, May 2012, Strasbourg (France).
- 3:** Poster presentation with the title “Near-field characterization of strongly confined channel plasmon polariton modes,” NFO-12 conference, September 2011, Donostia – San Sebastian (Spain).
- 4:** Poster presentation with the title “Nanofocusing in circular sector-like nanoantennas,” Nanolight Conference, March 2014, Bidasoa (Spain).